NASA/TP—2018–219996

Gradient Field Imploding Liner Fusion Propulsion System

NASA Innovative Advanced Concepts Phase I Final Report

M.R. Lapointe and R.B. Adams
Marshall Space Flight Center, Huntsville, Alabama

J. Cassibry and M. Zweiner
The University of Alabama—Huntsville, Huntsville, Alabama

J.H. Gilland
Ohio Aerospace Institute, Cleveland, Ohio

September 2018

The NASA STI Program…in Profile

Since its founding, NASA has been dedicated to the advancement of aeronautics and space science. The NASA Scientific and Technical Information (STI) Program Office plays a key part in helping NASA maintain this important role.

The NASA STI Program Office is operated by Langley Research Center, the lead center for NASA's scientific and technical information. The NASA STI Program Office provides access to the NASA STI Database, the largest collection of aeronautical and space science STI in the world. The Program Office is also NASA's institutional mechanism for disseminating the results of its research and development activities. These results are published by NASA in the NASA STI Report Series, which includes the following report types:

- TECHNICAL PUBLICATION. Reports of completed research or a major significant phase of research that present the results of NASA programs and include extensive data or theoretical analysis. Includes compilations of significant scientific and technical data and information deemed to be of continuing reference value. NASA's counterpart of peer-reviewed formal professional papers but has less stringent limitations on manuscript length and extent of graphic presentations.

- TECHNICAL MEMORANDUM. Scientific and technical findings that are preliminary or of specialized interest, e.g., quick release reports, working papers, and bibliographies that contain minimal annotation. Does not contain extensive analysis.

- CONTRACTOR REPORT. Scientific and technical findings by NASA-sponsored contractors and grantees.

- CONFERENCE PUBLICATION. Collected papers from scientific and technical conferences, symposia, seminars, or other meetings sponsored or cosponsored by NASA.

- SPECIAL PUBLICATION. Scientific, technical, or historical information from NASA programs, projects, and mission, often concerned with subjects having substantial public interest.

- TECHNICAL TRANSLATION. English-language translations of foreign scientific and technical material pertinent to NASA's mission.

Specialized services that complement the STI Program Office's diverse offerings include creating custom thesauri, building customized databases, organizing and publishing research results…even providing videos.

For more information about the NASA STI Program Office, see the following:

- Access the NASA STI program home page at <http://www.sti.nasa.gov>

- E-mail your question via the Internet to <help@sti.nasa.gov>

- Phone the NASA STI Help Desk at 757–864–9658

- Write to:
  NASA STI Information Desk
  Mail Stop 148
  NASA Langley Research Center
  Hampton, VA 23681–2199, USA

NASA/TP—2018–219996

Gradient Field Imploding Liner Fusion Propulsion System

NASA Innovative Advanced Concepts Phase I Final Report

M.R. Lapointe and R.B. Adams
Marshall Space Flight Center, Huntsville, Alabama

J. Cassibry and M. Zweiner
The University of Alabama—Huntsville, Huntsville, Alabama

J.H. Gilland
Ohio Aerospace Institute, Cleveland, Ohio

National Aeronautics and
Space Administration

Marshall Space Flight Center • Huntsville, Alabama 35812

September 2018

Acknowledgments

The authors gratefully acknowledge the support of the NASA Innovative Advanced Concepts Program during this Phase I study.

Available from:

NASA STI Information Desk
Mail Stop 148
NASA Langley Research Center
Hampton, VA 23681–2199, USA
757–864–9658

This report is also available in electronic form at
<http://www.sti.nasa.gov>

TABLE OF CONTENTS

1. BACKGROUND 1

   1.1 Concept Description 1
   1.2 Benefits and Challenges 4

2. PHASE I RESEARCH OVERVIEW 6

   2.1 Target Design 6
   2.2 Target Accelerator Concepts 8
   2.3 Magnetic Field Coil Design 11
   2.4 Estimating System Performance 12

3. SEMI-ANALYTIC COMPRESSION MODEL 14

   3.1 Liner Radial Acceleration 15
   3.2 Pressure Terms 16
   3.3 Energy Terms 17
   3.4 Net Energy Change and Fuel Temperature 20
   3.5 Fusion Reaction Rates 21

4. ANALYTIC MODEL: PRELIMINARY RESULTS 24

   4.1 Model Check: Adiabatic Compression 24
   4.2 Initial Target Density 25
   4.3 Initial Target Radius 26
   4.4 Initial Target Velocity 27
   4.5 Target Preheating 28
   4.6 External Magnetic Field 29
   4.7 Internal Target Magnetic Field 30
   4.8 Magnetic Field Gradient 31
   4.9 Liner Material 32
   4.10 Pulse Considerations 34
   4.11 Optimized Case 36
   4.12 Summary 42

TABLE OF CONTENTS (Continued)

5. SPFMAX THREE-DIMENSIONAL NUMERICAL MODEL 43

5.1 SPFMaX Preliminary Results 49
5.2 Verification Test Case Plan 51

6. MISSION ANALYSIS 55

6.1 Detailed Mission Examples 57

7. VEHICLE DESIGN 60

7.1 Vehicle Assumptions 61

8. OPTIONS FOR A GROUND-BASED, PROOF-OF-CONCEPT DEMONSTRATION 63

8.1 Two-Stage Light Gas Gun 63
8.2 Test Facility Description 64
8.3 Target Projectiles 67
8.4 Potential Test Setup 68

9. CONCLUDING REMARKS 70

APPENDIX A—ANALYTIC MODEL BLOCK DIAGRAM 71

APPENDIX B—ANALYTIC MODEL DATA VALUES 73

REFERENCES 76

LIST OF FIGURES

1. Pulsed θ-pinch operation (adapted from ref. 15) 3

2. Gradient field imploding liner concept 4

3. Standard fusion reactions, energy release, and cross sections (adapted from ref. 13) 6

4. Lindl-Widner diagram for D-T cylinder at stagnation (adapted from ref. 20) 7

5. Example of magnetic field topology (stream lines) generated by coaxial windings of magnetic field coils (yellow). Outline of representative nozzle walls and chamber geometry are for illustrative purposes (adapted from ref. 28) 12

6. Example of: (a) Half-plane contours for axial magnetic field strength half-plane contours (coil geometry in black box) and (b) corresponding axial magnetic field strength along the magnetic centerline as a function of axial position 14

7. Specific impulse as a function of initial fuel density 26

8. Specific impulse as a function of initial target radius 27

9. Specific impulse as a function of initial target velocity 28

10. Specific impulse as a function of uniformly preheated fuel temperature 29

11. Specific impulse as a function of axial magnetic field external to the target 30

12. Specific impulse as a function of initial target internal magnetic field 30

13. Specific impulse as a function of axial magnetic field gradient 31

14. Specific impulse as a function of target liner material 32

15. Yield as a function of target liner material 33

16. Impulse as a function of target liner material 33

17. Target radius compression, expansion, and subsequent compression cycle 35

LIST OF FIGURES (Continued)

18. External and internal magnetic field values for Be- and Li-lined targets 37

19. Evolution of liner and fuel radius with time 37

20. Evolution of D-T fuel mass density with time 38

21. Evolution of number of D-T ions with time 38

22. Evolution of D-T fuel temperature with time 39

23. Evolution of fuel areal density (ρR) with time 40

24. Cumulative target yield as a function of time 40

25. Evolution of neutron production with time 41

26. Cumulative neutron production with time 41

27. Example of external circuit and connections to anode and cathode of a z-pinch with SPH particles (red, gray, and black) immersed in electric particles (cyan) and magnetic particles (yellow) 47

28. Magnetic field coil: (a) With converging/diverging windings and (b) with magnetic field streamlines 49

29. Sequence of target propagation through the entrance of a magnetic field coil: (a) 0 ns, (b) 500 ns, (c) 1,000 ns, and (d) 1,500 ns 50

30. Preliminary simulation of the gradient field propulsion system 51

31. Flux compression generator illustration: (a) A conductive plate with a seed current and seed field traps flux between itself and a bottom conductive plate. Explosives or other force push the plate down with a negative vertical velocity and (b) the top plate and compressed area between the plates. The flux is conserved, and the current rises under conditions discussed in the text 51

32. Circuit in an FCG 53

33. Screen capture of the MATLAB-based GUI flux compression generator model developed for this project 54

34. Mission performance contours for one-way trip to Mars 56

LIST OF FIGURES (Continued)

35. Mission performance contours for one-way trip to Saturn 56

36. Mars (a) propellant mass and (b) total initial mass scaling for the Li liner gradient field fusion case 57

37. Mars (a) propellant mass and (b) total initial mass scaling for the Be liner gradient field fusion case 58

38. Saturn (a) propellant mass and (b) total initial mass scaling for the Li liner gradient field fusion case 58

39. Saturn (a) propellant mass and (b) total initial mass scaling for the Be liner gradient field fusion case 59

40. Illustrative vehicle concept 60

41. Major components of a two-stage LGG 64

42. Steps in LGG firing sequence 64

43. General facility launch mass/velocity capability 65

44. Intermediate-sized, two-stage LGG range 66

45. Multiple data acquisition and image access ports for flexible test setup 66

46. Hollow steel sphere with filler material 67

47. Hollow steel sphere and sabot used for support during launch 67

48. Magnetic flux and target compression test setup 68

LIST OF TABLES

1. Coefficients for reaction rate calculations (adapted from ref. 30) 22

2. Predicted and analytic adiabatic compression fuel temperatures for various initial conditions 25

3. Target and magnetic field values used in liner material evaluation 32

4. Engine performance estimates for optimized target and magnetic field values 42

5. Calculated performance space for gradient field fusion system 57

6. Preliminary vehicle design parameters 61

7. UAH ARC two-stage LGG parameters with single-stage example 65

LIST OF SYMBOLS AND ACRONYMS

Al	aluminum
AR	aspect ratio
ARC	Aerophysics Research Center
Be	beryllium
CO_2	carbon dioxide
D	deuterium
FCG	flux compression generator
GUI	graphical user interface
HDPE	high density polyethylene (plastic)
He	helium
ICF	inertial confinement fusion
IMLEO	initial mass in low Earth orbit
LEO	low Earth orbit
LGG	light gas gun
Li	lithium
MagLIF	magnetized liner inertial fusion
MGL	mass growth allowance
MIF	magneto-inertial fusion
MTF	magnetized target fusion
NIAC	NASA Innovative Advanced Concepts

LIST OF SYMBOLS AND ACRONYMS (Continued)

SAMM	semi-analytic MagLIF Model
SLS	Space Launch System
SPFMaX	Smooth Particle Fluid with Maxwell Equation Solver (code developed by UAH)
SPH	smooth particle hydrodynamic
T	tritium
TP	Technical Publication
UAH	The University of Alabama—Huntsville

NOMENCLATURE

$\mathbf{A}$	magnetic vector potential
AR	aspect ratio
a	(subscript) point in space
B	magnetic field
B_i	internal magnetic field strength
B_{i0}	initial trapped magnetic field
B_{v0}	initial vacuum magnetic field
B_z	axial component of magnetic field
b	neighboring particles
C'	capacitive gradient per particle
C_0–C_7	fitting parameters
C_c	sound speed at critical target density
c	speed of light in a vacuum
c_f	speed of sound in fuel region
dB_z/dt	rapidly changing axial magnetic field
E	yield energy
$\dot{E}_{ad}$	adiabatic heating rate
$\dot{E}_{end}$	energy loss rate due to end particle losses
$\dot{E}_f$	time rate of change in fuel energy
E_f	cumulative energy in the fuel

NOMENCLATURE (Continued)

$\dot{E}_{pre}$	fuel preheating rate
$\dot{E}_{tc}$	thermal conduction cooling rate
$\dot{E}_{\alpha}$	α particle heating rate
e	elementary unit of charge
F	thrust
F_{ave}	average thrust
f	frequency; exhaust shape factor
f_{α}	fraction of alpha particle energy deposited in the fuel
G	gain
g_0	acceleration of gravity
I	laser intensity; current
I_{bit}	impulse
I_n	net current into the particle
I_{sp}	specific impulse
$\mathbf{j}$	current density vector
k	Boltzmann's constant; thermal conductivity
L	length of cylindrical fuel element; target length; liner length
L_0	target diameter
l_{α}	mean free path of an α particle; fraction of energy deposited in the fuel
$\ln(\Lambda)$	Coulomb logarithm
M_0	initial mass

NOMENCLATURE (Continued)

M_f	fuel mass
$\dot{m}$	propellant mass flow rate
m	expelled propellant mass
m_0	initial pellet mass; initial target mass
m_D	deuteron mass
m_e	electron mass
m_f	final pellet mass following ablation; fraction of target mass
m_i	ion mass
$\bar{m}_i$	average ion mass
m_l	liner mass
m_T	triton mass
m_α	α particle rest mass
N_{D}	total number of deuterons
$\dot{N}_{\mathrm{D\text{-}T}}$	D-T reaction rate
N_e	total number of electrons
N_{T}	total number of tritons
$\mathbf{n}$	unit normal for each face of particle
n_0	initial density of ablated material
n_c	critical density
n_{D}	fuel deuteron number density
n_e	electron number density

NOMENCLATURE (Continued)

n_i	ion number density
n_s	species number density
n_{T}	fuel triton number density
P	power
P_{Bi}	magnetic field pressure internal to the target
P_{Bv}	magnetic field pressure external to the target
P_f	isobaric fuel pressure
P_{fusion}	fusion power released by the imploding target
P_{gen}	generated fusion power
P_{in}	input power
P_{jet}	jet power
P_{li}	liner pressure facing the fuel
P_{lv}	liner pressure facing the vacuum
P_M	magnetic field pressure
P_{rs}	surface radiation
P_{rv}	volume radiation
P_{target}	laser power on target
p	static pressure
Q_α	α particle energy
R	outer radious of the target; universal gas constant
r	radius

NOMENCLATURE (Continued)

r_0	initial fuel radius
r_0/r	compression ratio
r_c	coil radius
r_f	fuel radius
$\ddot{r}_{fl}$	radial acceleration of fuel-liner interface
r_l	external target radius including liner
$\ddot{r}_{lv}$	radial acceleration of liner-vacum interface
$r_{\alpha L}$	α particle Larmor radius
T	(subscript) transmission line section
T_0	initial fuel temperature
T_B	brightness temperature
T_f	fuel temperature
t	time
t_b	time to fully burn through ablative target material
u	velocity vector
V	particle volume
V_b	volume of the neighboring particles b
V_f	fuel volume
v_e	exhaust velocity
v_z	axial velocity
v_{z_target}	axial velocity of the target imparted by the accelerator

NOMENCLATURE (Continued)

$v_{\alpha 0}$	initial velocity of the α particle
W	interpolating kernel function
x_0	initial plate spacing
x_e	electron Hall parameter
x_i	ion Hall parameter
$\bar{Z}_f$	average ionization state of the fuel
Z_α	α charge
α	specific power of propulsion system
α_s	albedo of the liner's inner surface
γ_f	ratio of specific heats for an ideal gas
Δ	liner thickness
Δt	time step
Δv	velocity imparted to the pellet
ε	infrared emissivity
ε_0	permittivity of free space
η	efficiency
κ_e	electron thermal conduction coefficient
λ	plate width
μ	permeability of the liner
μ_0	permeability of free space
ρ	mass density

NOMENCLATURE (Continued)

ρR	areal density of the target
σ	conductivity of the liner; Stefan-Boltzmann constant
σ_v	reactivity parameter for D-T reactions
τ	diffusion time; deviatoric viscous stress tensor
τ_{ei}	average electron-ion collison time
τ_{ii}	average ion-ion collision time
φ_i	magnetic flux
φ_{loss}	radiated power loss to space
ϕ	electric scalar potential
ϕ_{therm}	thermal loss
χ_{Planck}	single group Planck emission opacity
ω	frequency of incident laser light
ω_{ce}	electron cyclotron frequency
ω_{ci}	ion cyclotron frequency

TECHNICAL PUBLICATION

GRADIENT FIELD IMPLODING LINER FUSION PROPULSION SYSTEM
NASA INNOVATIVE ADVANCED CONCEPTS PHASE I FINAL REPORT

1. BACKGROUND

The advancement of human deep space exploration requires the continued development of energetic in-space propulsion systems, from current chemical engines to nuclear thermal rockets to future high energy concepts such as nuclear fusion. As NASA embarks on a program to develop near-term nuclear thermal propulsion, this NASA Innovative Advanced Concepts (NIAC) Phase I activity was funded to investigate the feasibility of an innovative approach toward highly energetic pulsed fusion propulsion. Previous concept studies have proposed the conversion of fusion energy for in-space propulsion, ranging from laser-ignited fusion systems such as Gevaltig[1] and VISTA,[2] to the British Interplanetary Society's Daedalus concept[3] and its more recent incarnation under Project Icarus,[4] to steady-state spherical torus fusion systems.[5] Recent NIAC studies have also evaluated several innovative fusion concepts, including the acceleration and compression of field reversed configuration plasmas in time-changing magnetic fields,[6] magnetically driven liners imploding onto plasma targets,[7] and high current *z*-pinch compression of material liners onto fission-fusion fuel targets.[8] While each of these studies firmly established the potential benefits of fusion systems for interplanetary travel, they also identified significant challenges in successfully engineering such systems for spacecraft propulsion. The concept outlined in this Technical Publication (TP) builds on the lessons learned from these prior activities, approaching the quest for fusion-powered propulsion through an innovative variation of magneto-inertial fusion concepts developed for terrestrial power applications.

1.1 Concept Description

The rapid magnetic compression of targets containing fusion fuel at high pressure offers potentially higher implosion efficiencies than other inertial confinement fusion approaches, and remains an area of active development.[9–11] To successfully implode the target and trigger fusion reactions, a pulsed high current discharge in a surrounding magnetic field coil generates a rapidly changing axial magnetic field, dB_z/dt, which induces a counterpropagating current in the conducting outer liner of a centrally aligned cylindrical target. The inductively driven liner current rapidly implodes the liner radially inward, compressing the fuel to the densities and temperatures required for fusion. A significant energy loss mechanism observed during liner compression and ignition of the resulting plasma is electron thermal conduction, which is mitigated by the use of strong magnetic fields to suppress cross field thermal conduction losses, generating higher plasma temperatures at lower implosion velocities.[12]

While promising, there are several challenges associated with imploding liner fusion concepts that must be addressed in the context of a propulsion system. The requirement of short duration, high current pulses to produce a rapidly changing magnetic field for target compression precludes the use of superconducting magnets, resulting in significant resistive losses and coil heating. Related issues include the need for capacitive or inductive power supplies, pulse-forming networks, and robust, long-life switches capable of repetitively channeling several MA of pulsed current into the magnetic field coil. Repetitive and accurate target replacement within the coil after each pulse, together with mitigating liner or other target material debris impacts to the chamber walls, presents additional engineering challenges. Targets must be designed to suppress potential instabilities that may occur at the liner-fuel interface during compression, either by judicious choice of liner materials and thickness in solid target liners or the rotation of liquid liners prior to compression. Preheating the target fuel has been shown to improve ignition, and a method to efficiently deliver an energy pulse to the target prior to main compression must be incorporated. Finally, coupling the significant energy gain released in a successful target fusion event to the spacecraft without incurring structural or material damage requires directing the rapidly expanding plasma out of the chamber, using either a magnetic nozzle or causing the event to occur downstream where it can impact against a pusher plate to provide thrust.

The proposed concept takes advantage of the significant advances in terrestrial magneto-inertial fusion (MIF) designs while attempting to mitigate the potential engineering impediments to in-space propulsion applications. Methods to induce a rapid radial compression in a stationary central target typically focus on z-pinch or θ-pinch geometries. In the z-pinch geometry, a very high current pulse is sent through a conducting liner coating a cylindrical fusion target. The axial current induces an azimuthal magnetic field, and the combination creates a radial Lorentz force that rapidly compresses the target to high density and temperature. In a θ-pinch geometry, current is pulsed through a drive coil surrounding the central target. The pulsed current creates a time-changing axial magnetic field, which in turn induces an azimuthal current in the conducting target liner. The combination of strong axial magnetic field and induced azimuthal current combine to again provide a rapid radial Lorentz force compression of the target. Equivalently, the compression mechanism in each case can be considered the result of a rapid buildup of external magnetic field pressure external to the conducting liner, which inhibits field penetration into the target. The external pressure significantly exceeds the target fuel internal pressure, forcing a rapid radial compression until the pressures equilibrate at high internal densities and temperatures.

A prior NIAC Phase I study evaluated the application of z-pinch geometries for in-space propulsion,[8] and several ground-based fusion experiments are based on the z-pinch approach.[13,14] Although options to incorporate z-pinch physics into an in-space propulsion system continue to be explored by the previous NAIC authors, the current concept instead utilizes a geometry more closely aligned with the θ-pinch. An overview of the θ-pinch operation is provided in figure 1.[15] As noted, current sent through the drive coil induces an opposing azimuthal current in the stationary central target liner, and the combination of increasing axial magnetic field and induced azimuthal current provide rapid radial compression.

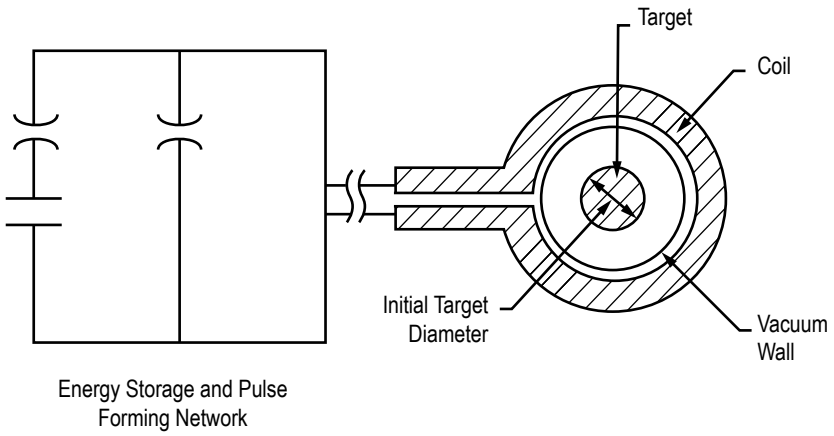

Figure 1. Pulsed θ-pinch operation (adapted from ref. 15).

The approach being investigated in the current Phase I activity replaces the pulsed, high current magnetic field coil and stationary central target with a fast-moving target fired axially into a static, high gradient magnetic field. This essentially decomposes the time-changing derivative of the axial magnetic field into partial derivatives associated with an axial magnetic field gradient and an axial velocity:

$$\frac{dB_z}{dt} = \frac{\partial B_z}{\partial z}\frac{\partial z}{\partial t} = v_z \frac{\partial B_z}{\partial z} \quad . \tag{1}$$

As such, a target fired at high axial velocity into a steep magnetic field gradient will effectively experience a rapidly changing axial magnetic field and undergo the same inductive compression as a stationary target at the center of a rapidly pulsed magnetic field. A conceptual overview of this gradient field imploding liner system is provided in figure 2, forming the basis for the study outlined in this TP.

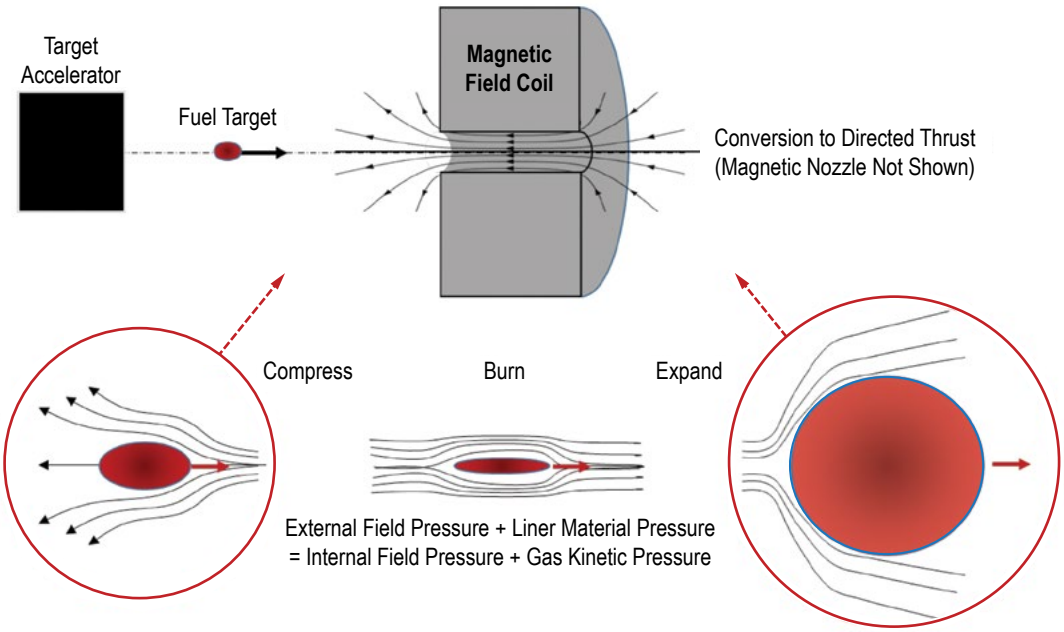

Figure 2. Gradient field imploding liner concept.

1.2 Benefits and Challenges

Shifting the onus of rapid target compression from a pulsed, high current coil to a target accelerator and a static high gradient magnetic field offers several potential advantages for in-space propulsion. Eliminating the need to rapidly pulse the magnetic field coil allows the use of energy efficient superconducting field coils, which in turn reduces energy storage requirements, coil thermal losses, and associated radiator requirements. The field coils can be shaped to provide strong upstream field gradients, a high field midsection to enhance target fuel burning, and a magnetic nozzle at the downstream exit plane to convert the rapidly expanding plasma into directed thrust. Target acceleration may be accomplished using one of several possible approaches, including inductive acceleration or laser ablation, the latter also offering a possible method for preheating the target fuel. Electron and ion radial thermal losses can be suppressed by strong internal magnetic fields trapped within the target during compression, reducing energy losses and improving target gain. The linear geometry of the system, together with the axial motion of the target as it enters, compresses, burns, and expands into the magnetic nozzle region, lends itself more naturally to repetitively pulsed in-space propulsion, easing design issues associated with target placement and energy transfer to the vehicle.

To realize these potential benefits, a number of significant challenges are being addressed during this Phase I activity to determine the feasibility of the concept. These include modeling the magnetic field geometries and axial gradients required for fuel target compression, evaluating accelerator concepts to achieve high target velocities, evaluating initial target fuels and design options, and evaluating methods to convert the expanding high temperature plasma into directed thrust. Analytic and numerical models have been developed to simulate and understand target pellet compression and burn physics, which in turn feed back into target accelerator concepts, magnetic field designs,

and mission performance parameters. Preliminary mission trajectory analysis and vehicle designs are being developed to guide system performance requirements and quantify potential benefits for crewed or robotic solar system and deep space exploration. Each of these areas are discussed in the following sections, which describes the methods, research status, and initial results that will underpin the determination of concept viability.

2. PHASE I RESEARCH OVERVIEW

The purpose of this Phase I activity is to design and evaluate a system that can rapidly inject, compress, and burn a fusion fuel target, and efficiently exhaust the resulting high temperature plasma, in a configuration suitable for in-space propulsion applications. Taking advantage of the experience gained by international MIF research programs, the concept under evaluation seeks to replicate well known static target compression physics in a novel, dynamic system. As terrestrial systems advance toward break even, the target designs and field requirements used to reach these higher yields can be readily incorporated into this innovative in-space system design.

2.1 Target Design

For this initial Phase I evaluation, a cylindrical pellet with deuterium-tritium (D-T) fuel and a conductive liner has been chosen both for simplicity of modeling and for consistency with current terrestrial MIF fusion experiments. D-T fuels have a higher fusion cross section at lower ignition temperatures, making them a standard fuel of choice for most terrestrial experiments. Figure 3 lists several fusion reactions with their corresponding energy release, and a plot of reaction cross section versus center of mass energy.[16]

Reaction	Energy Release
$D + T \rightarrow \alpha + n$	17.59 MeV
$D + D \rightarrow T + p$	4.04 MeV
$D + D \rightarrow {}^3He + n$	3.27 MeV
$D + {}^3He \rightarrow \alpha + p$	18.35 MeV
$D + {}^6Li \rightarrow 2\alpha$	22.374 MeV
$D + {}^6Li \rightarrow p + {}^7Li$	5.026 MeV
$D + {}^6Li \rightarrow n + {}^7Be$	3.38 MeV
$p + {}^{11}B \rightarrow 3\alpha$	8.68 MeV
$n + {}^6Li \rightarrow T + \alpha$	4.86 MeV
$n + {}^7Li \rightarrow T + \alpha + n$	–2.87 MeV

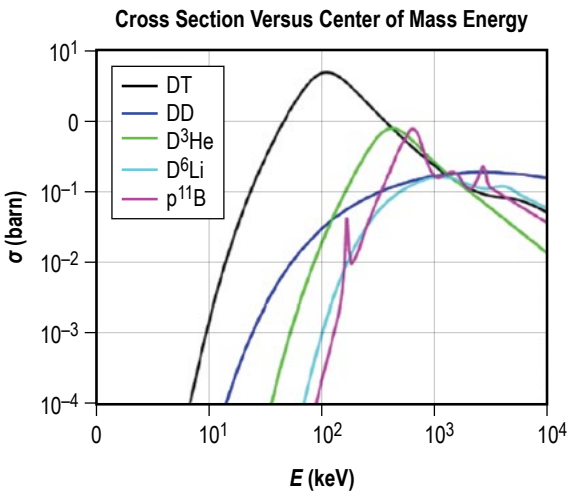

Figure 3. Standard fusion reactions, energy release, and cross sections (adapted from ref. 16).

Several low atomic number coating materials have been investigated as conductive target liners, including beryllium (Be), aluminum (Al), and lithium (Li).[17] For the inductively driven target compression under consideration, the liner material serves to carry the induced azimuthal current,

interacting with the applied axial magnetic field to generate a radial Lorentz force and rapidly compress the target. The heavier liner shell also provides momentum to the imploding target, stagnating on axis to provide longer confinement and burn times for more efficient fuel conversion.

Several ground-based experiments and numerical studies have shown that the ratio of target radius to liner thickness (the aspect ratio (AR)) plays a role in the evolution of disruptive Rayleigh-Taylor instabilities:

$$AR = \frac{R}{\Delta R} \ , \tag{2}$$

where R is the outer radius of the target (including liner), and ΔR is the liner thickness. Aspect ratio values ≤6 have been shown to delay the onset of Rayleigh-Taylor instabilities,[18,19] which if left unchecked, will significantly limit target convergence and enhance material mixing between the liner and target layers. Enhanced mixing leads to a substantial reduction in fusion burnup due to high z poisoning of the mixing layer and faster thermal conduction losses. As such, most targets employ liner coatings that satisfy this AR to improve target compression and heating. Additional methods to reduce the Rayleigh-Taylor instability have also been investigated, including the use of thin dielectric coatings over metallic liners,[19] which appears to significantly improve converging target uniformity. While not evaluated in this Phase I effort, dielectric coating of metallic liners can be incorporated into the Smooth Particle Fluid with Maxwell Equation Solver (SPFMaX) model currently under development by The University of Alabama—Huntsville (UAH) and remains an area for later investigation.

A key parameter for achieving fusion conditions is the areal density of the target, expressed as ρR, where ρ is the fuel density and R is the radius at maximum compression. Values of ρR as a function of temperature required to achieve net energy gain are plotted in Lindl-Widner diagrams, an example of which is shown in figure 4 for cylindrical D-T fuel at stagnation.[20]

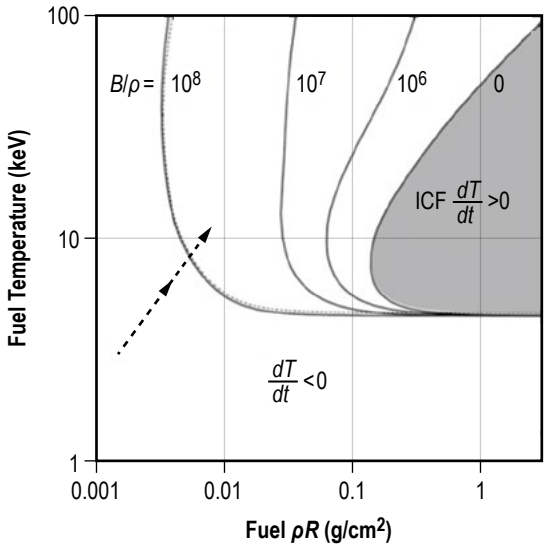

Figure 4. Lindl-Widner diagram for D-T cylinder at stagnation (adapted from ref. 20).

The shaded region shows the area of net gain in pure inertial confinement fusion (ICF) without internal magnetic fields. The solid lines demarking areas to the left of this region show ρR, T parameters required for net energy gain in cases where the targets have internal magnetic fields (displayed in the figure as values of B/ρ). Such plots show that incorporating strong magnetic fields within the fuel can significantly reduce the value of ρR required for net energy gain at a given temperature. This in turn implies a less stringent requirement on the final fuel density and radius at compression, reducing the energy required to compress the target. In current MIF experiments, applied magnetic fields of a few to several tesla are often used as the seed fields to produce compressed fields of 10^2–10^3 T during the brief period of target implosion. Assuming an axial magnetic field is present and remains trapped within the cylindrical fuel target during compression, the field strength will be significantly increased during compression via the conservation of magnetic flux. These strong axial magnetic fields can trap charged α particles produced during the fusion process to enhance fuel heating, and in addition, serve to reduce the loss of energy through radial electron and ion thermal conduction. This is the major advantage of MIF concepts over pure ICF, and why these systems are being actively investigated to provide terrestrial fusion power. The concept discussed in this TP likewise incorporates the use of seed magnetic fields to enhance the performance of the system.

In addition to pure fusion targets, prior studies have also investigated fission-fusion hybrid targets for magnetically imploding systems,[21] including the recent NIAC effort to develop a pulsed fission-fusion z-pinch system.[8] In that concept, the target contained a central cylinder of D-T material, surrounded by a ^{238}U cylindrical sheath, which in turn is surrounded by a cylindrical Li sheath. Upon implosion, the D-T mixture is compressed and a limited number of fusion reactions begin to take place. The resulting fast thermonuclear neutrons bombard the surrounding ^{238}U and induce fission, which in turn increases the fusion yield of the D-T core. Neutrons from both fission and fusion reactions are reflected and moderated by the surrounding Li liner, reducing neutron escape and damage to surrounding structures. In this hybrid design, fusion neutrons result in a more complete burn of the fissile fuel, sustaining energy release. This sustained release extends the compression of the fusion reactants, yielding more fusion reactions, which in turn release more neutrons for more fissile material consumption. This synergy has been observed in the development of other fission-fusion devices, leading to more complete fuel burnup and allowing fusion ignition to be achieved with lower initial energy input than pure D-T targets. For the proposed concept, this would also translate into less severe requirements on the initial pellet velocities generated by the accelerator or on the strength of the gradient magnetic field. Pending a determination of the initial feasibility of the concept, a hybrid target remains a viable option to be investigated.

2.2 Target Accelerator Concepts

Maintaining a static magnetic field with constant currents in superconducting coils simplifies the problem of repetitively pulsed high current coil discharges and associated coil heating but introduces a new challenge in the design of the pellet accelerator. To induce rapid radial compression as the pellet enters the gradient magnetic field requires a high initial pellet velocity of several kilometers per second. Several options were considered for the pellet accelerator, including gas guns, rail guns, electrothermal and electromagnetic accelerator concepts, and laser ablation acceleration. The dual requirements of efficient pellet acceleration to velocities of several kilometers per second and repetitive, long life operation in a vacuum environment reduced the initial set of options to the conceptual

electromagnetic macron accelerator proposed by Kirtley,[22] electrothermal accelerators proposed to accelerate fuel pellets for tokomak systems,[23] and laser ablation concepts also proposed for use in refueling tokomak and other magnetic confinement fusion systems.[24–26] Of these, the macron system appears capable of accelerating gram-size pellets to the required velocities but has not yet been demonstrated. Electrothermal accelerators working via ablative arcs have been demonstrated to achieve a few kilometers per second with gram-size pellets, and remain a potential option. Laser ablation employs a high-power laser pulse to ablate material at high velocity from one end of the pellet, causing the remaining mass to accelerate in the opposite direction. Models and initial experiments indicate accelerations of up to 200 km/s for millimeter-size D-T pellets using modest laser intensities of 10^{14} W/cm^2, readily achieved by commercially available carbon dioxide (CO_2) lasers. Of additional interest, it may be possible to provide preheating of the accelerated pellet via the same laser pulse, which can significantly increase the final temperature achieved during pellet compression. For these reasons, the laser ablation concept was chosen for a more detailed initial evaluation.

Following the model of Jarboe[25] and Jarboe et al.,[26] the laser ablation concept is treated using the rocket equation, where the ablated material plays the role of reaction mass expelled from the system:

$$\Delta v = v_e \ln\left(\frac{m_0}{m_f}\right), \tag{3}$$

where Δv is the velocity imparted to the pellet, v_e is the velocity of the ablated material leaving the pellet, m_0 is the initial pellet mass, and m_f is the final pellet mass following ablation. For the gradient field concept, the required pellet velocity is on the order of 10 km/s, hence the equation can be inverted to determine the fraction of material that must be ablated to provide this velocity:

$$1-\frac{m_f}{m_0} = 1-\exp\left(\frac{-\Delta v}{f \cdot v_e}\right). \tag{4}$$

Here, an 'exhaust' shape factor (f) has been included in the expression to account for ablated material leaving the surface at angles to the axial direction of motion. Laser ablation experiments performed on conically shaped pellets provide a shape factor of approximately 0.6.[25]

Assuming that the energy imparted to the ablated material is converted to kinetic energy of the ions, the velocity v_e is given by:[26]

$$v_e = \left(\frac{4\,I}{n_c\, m_i}\right), \tag{5}$$

where I is the laser intensity illuminating the pellet, n_c is the critical density at which the incident laser light frequency equals the plasma frequency, and m_i is the mass of the ion species being accelerated. The critical density is given by:

$$n_c = \left(\frac{m_e \varepsilon_0 \omega^2}{e^2} \right), \tag{6}$$

where m_e is the electron mass, ε_0 is permittivity of free space, ω is the frequency of the incident laser light, and e is the elementary unit of charge. Assuming a CO_2 laser with a wavelength of 10.6 μm, the laser light frequency is 2.83×10^{13}/s. Substituting into the equation above yields a critical density of $2.52 \times 10^{23}/m^3$.

Assuming the laser illuminates and ablates liner material, a choice must be made for the liner. As noted in the preceding section, various liner materials have been proposed for MIF pellets, including Al, Li, and Be. For this sample calculation, Al is chosen as a representative liner material. The ion mass is then given by $m_i = 27 \cdot (1.6726 \times 10^{-27})$ kg = 4.52×10^{-26} kg.

The laser illumination can be estimated using available laser powers and appropriately sized beam widths that approximate the pellet cross section. Available high-power CO_2 lasers can readily provide 10 kW of power. Assuming an initial pellet radius of 1 cm provides a cross-sectional area of around 3.14×10^{-4} m^2, for a pulsed laser intensity of 3.18×10^7 W/m^2.

Combining these results into a calculation of ablated ion velocity yields:

$$v_e = \left(\frac{(4)\left(3.18 \times 10^7\right)}{\left(2.52 \times 10^{23}\right)\left(4.52 \times 10^{-26}\right)} \right)^{1/2} = 1.06 \times 10^5 \text{ m/s}. \tag{7}$$

The fraction of ablated liner mass required to provide this velocity is then given by:

$$1 - \frac{m_f}{m_0} = 1 - \exp\left(\frac{-10^4}{(0.6)\left(1.06 \times 10^5\right)} \right) = 0.15 . \tag{8}$$

Thus, for the given parameters, ablating 15% of the liner mass would provide a pellet injection velocity of 10 km/s. Increasing the incident laser energy on the target would increase the ablated ion velocity and reduce the amount of ablated material required to reach the desired injection velocity. For example, increasing the laser power from 10 to 100 kW in equation (7) would increase the ion velocity to 3.33×10^5 m/s. Substituting into equation (8) indicates that approximately 5% of the initial target (liner) material would need to be ablated at this higher power level to provide the required 10 km/s injection velocity. A 1 MW pulse reduces the mass requirement even further to around 1.5%. This mass could be accounted for by adding additional mass to the upstream face of the pellet, designed to be ablated away by the pulsed laser illumination. Alternatively, it may be possible to design the pellet with different ablative material at the back of the pellet, or if D-T ice is used as the fuel, illuminate the ice directly to provide a lower ablative ion mass and higher exhaust velocity. In addition, once the required velocity is imparted to the pellet and the ablative mass is worn away, the

laser pulse may be tailored to continue for a brief period to heat the internal fuel as the target enters the magnetic field and begins to compress. Achieving an internal fuel temperature of several tens to hundreds of eV prior to compression would reduce the amount of compression required to achieve fusion temperatures, which in turn can reduce the demands on pellet acceleration and compressive field strengths. Laser heating of D-T fuel pellets is an active area of investigation in magnetized liner inertial fusion. Sandia National Laboratories incorporates a 2.5 kJ, 1 TW Nd:YAG laser in their z-pinch experiments to preheat a stationary target prior to compression.[18]

2.3 Magnetic Field Coil Design

A simple solenoid magnetic field coil is assumed for this preliminary analysis. Steady-state, super-conducting solenoid coils with field strengths up to 30 T are now available,[27] and it is reasonable to expect coils at or above this field strength can be designed and manufactured for the proposed concept. As concept definition progresses, more complex coil geometries can be incorporated, including magnetic nozzle coils and transition coils between the primary gradient field coil and the magnetic nozzle. However, to investigate whether the concept can compress and heat a rapidly injected target within a reasonable distance and with realistic field strengths, a simple solenoid coil model will be used. Because typical target diameters are small (centimeter scale or less), a small-bore magnet can be used which should help reduce system mass and volume. Using a simple solenoid model also allows a ready calculation of axial and radial magnetic field strengths and gradients for use in the analytic and more advanced numerical models discussed below.

Some initial constraints on the axial length of the field coil can be estimated by assuming the injected target must be compressed and burned before the external (driving) magnetic field diffuses into the target, and exhausted into a magnetic nozzle before it dissociates to prevent damage to the coil. The diffusion time (τ) for a magnetic field to penetrate through a conducting layer into a cylindrical target can be estimated as:

$$\tau \approx \frac{\mu \sigma \Delta r}{2}\,, \tag{9}$$

where μ, σ, and Δ are the permeability, conductivity, and thickness of the liner, and r is the radius. For typical liner materials, the diffusion time is roughly on the order of 10^{-3} s. For an assumed initial target velocity of around 10 km/s, the target will travel a distance of approximately 10 m before the external magnetic field will diffuse into the interior of the target. A more stringent constraint is associated with the compression and burn time of the target. For the same initial target velocity and a compression time on the order of 10 μs, the distance traveled by the target (assuming no slowing down within the coil) is around 10 cm, indicating that the coil needs to be sufficiently short to allow the target to compress and burn within this distance before expanding into the nozzle region. While more detailed estimates of coil length can be derived from the compression models, the initial analysis indicates the magnetic field coil will likely be less than a meter in length.

Once fusion is achieved and the plasma begins to expand, it must be directed into axial thrust. The initial assumption is that a magnetic nozzle will be used for this purpose, and a numerical model has been developed by UAH to simulate this effect.[28] In this model the coil windings are grouped in

stages, with the number of windings and current in each stage treated as variables. The field is highest at the throat and expands downstream. The axial field gradient can be increased by increasing the number of windings, the current, or both, at the throat section while decreasing the field on either side of the throat stage. An example of a simulated magnetic nozzle is presented in figure 5. Once the numerical modeling work underpinning the compression and burn physics is completed, the model will be integrated with the magnetic nozzle simulation to provide a complete system description. More immediately, a magnetic nozzle efficiency factor can be employed to estimate system performance as discussed in section 2.4.

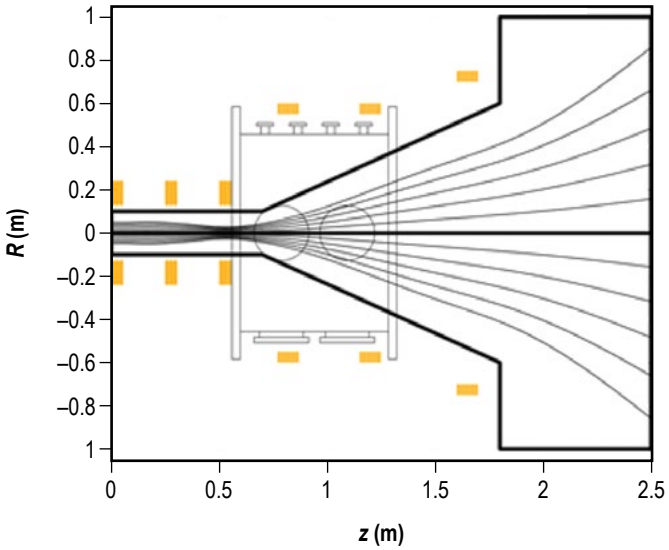

Figure 5. Example of magnetic field topology (stream lines) generated by coaxial windings of magnetic field coils (yellow). Outline of representative nozzle walls and chamber geometry are for illustrative purposes (adapted from ref. 28).

2.4 Estimating System Performance

The analytic and numerical models developed under this Phase I activity provide an estimate of the fusion yield energy, which in turn can be used to roughly estimate the exhaust velocity of the plasma propellant. Equating the yield energy, E, to the directed kinetic energy of a propellant provides the following equation for the exhaust velocity, v_e:

$$v_e = v_{z\_\text{target}} + \left(\frac{2\eta E}{m}\right)^{1/2}, \tag{10}$$

where v_{z_target} is the axial velocity of the target imparted by the accelerator (taking into account any reduction* due to traversing the radial portion of the magnetic field gradient), m is the expelled

* The analytic model was used to determine the change in initial target velocity caused by radial magnetic field pressure within the magnetic field gradient. In general, the axial target velocity was reduced by less than 10%.

propellant mass, and η is the efficiency at which the magnetic nozzle converts the uniformly expanding plasma into directed axial thrust. Values for η can vary widely, and the performance of the system will be more accurately represented through an integrated numerical simulation of the compression, burn, and expansion of the fusion plasma in the magnetic nozzle. However, for these preliminary Phase I estimates, a value of $\eta \approx 0.7$ is assumed, consistent with recommended practice.[29]

The specific impulse (I_{sp}) of the system can then be estimated using

$$I_{sp} = \frac{v_e}{g_0}\,, \tag{11}$$

where g_0 is the acceleration due to gravity (9.8 m/s^2). The impulse (I_{bit}) provided by the pulsed exhaust is calculated by:

$$I_{bit} = m v_e = \frac{m I_{sp}}{g_0}(\text{N-s})\,. \tag{12}$$

For a pulse repetition frequency f(Hz), the average thrust, F_{ave}, provided by the system is given by:

$$F_{ave} = f(\text{Hz}) \cdot I_{bit}\ . \tag{13}$$

Once the yield energy is defined, these equations can be used to estimate the performance of the system.

The overall gain of the fusion system can be estimated using the ratio of the yield energy to the energy required to accelerate and preheat the target (driver energy). As with other systems, using a laser will incur inefficiencies in converting the input power to laser power, and in converting the laser energy illuminating the target to directed kinetic energy. For an input power (P_{in}) to laser power conversion efficiency η_{in} and a laser power to power on target (P_{target}) conversion efficiency η_{target}, the gain (G) may be defined as:

$$G = \frac{P_{fusion}}{\left(\frac{P_{in}}{\eta_{in}}\right) + \left(\frac{P_{target}}{\eta_{target}}\right)}\,, \tag{14}$$

where P_{fusion} is the fusion power released by the imploding target. Gains exceeding unity are clearly desired for efficient system operation, but high gains can also place severe stress on vehicle structures. Defining the optimum gain to produce desired vehicle performance is integrally connected to the mission performance modeling described in a later section, and ties to requirements on specific impulse, power, and mass. This iterative process between mission modeling and fusion system modeling is currently ongoing as part of the Phase I activity.

3. SEMI-ANALYTIC COMPRESSION MODEL

A semi-analytic model is being developed to help evaluate initial concept feasibility and to provide initial approximations for magnetic field geometries, target fuel densities and initial velocities, target compression and heating, and fusion yields that could be used to guide more detailed numerical simulations and initial vehicle performance estimates. The model is based on the Semi-Analytic MagLIF Model (SAMM) developed by McBride and Slutz[30] for a terrestrial *z*-pinch geometry, modified and adapted to the current concept with additional simplifications to be discussed below. Given the unique nature of the concept under investigation, the quantitative values predicted by the modified semi-analytic model cannot be readily validated and provide crude approximations at best. However, the qualitative results likely predict correct trends and thus can be used to guide a smaller set of more accurate numerical simulations.

In its present form, the analytic model used in the Phase I effort consists of several interlinked analytic expressions, encompassing fuel and magnetic field pressure terms, liner radial acceleration, optional fuel preheating, α particle energy deposition, radiative losses, ion and electron thermal conduction losses, fusion reaction rate calculations, energy balance, and gain calculations. Developed to simulate a *z*-pinch system, the original SAMM included circuit equations for axial current generation and corresponding induced azimuthal magnetic fields acting on a stationary D-T fuel target. In the current model, a stationary magnetic field is assumed and a D-T target is injected into the field with a user-defined velocity. For simplicity, the initial model assumes a linear magnetic field gradient up to a maximum value of magnetic field within the coil, after which the field is assumed to remain constant within the coil. This is fairly consistent with numerical simulations of solenoid coil magnetic fields and associated axial gradients, an example of which is shown in figure 6.

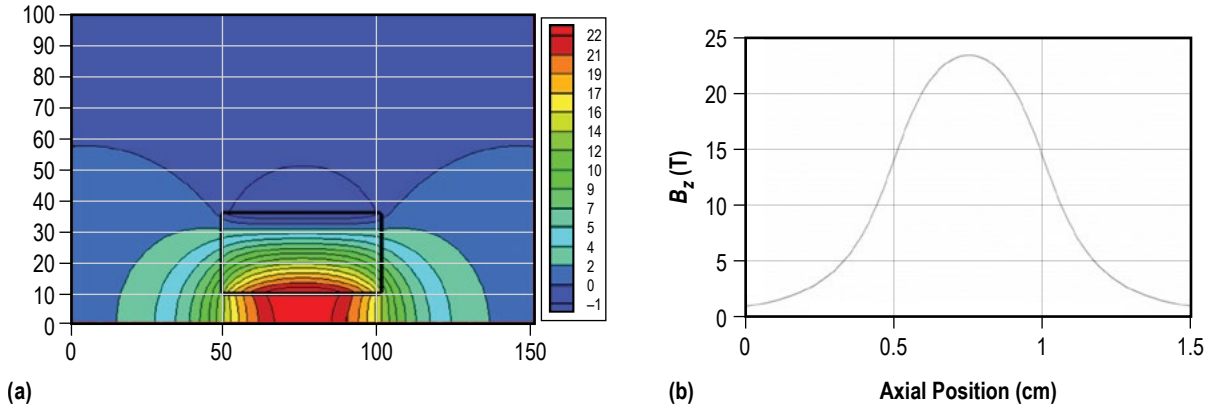

Figure 6. Example of: (a) Half-plane contours for axial magnetic field strength half-plane contours (coil geometry in black box) and (b) corresponding axial magnetic field strength along the magnetic centerline as a function of axial position.

User-defined inputs to the analytic model include the magnetic field coil radius, maximum axial magnetic field within the coil, axial magnetic field gradient, target outer radius and liner thickness, target length, liner material (currently Al, Be, or Li), the initial target D-T fuel mass density, initial target fuel temperature, initial target axial velocity, initial axial magnetic field internal to the target, and options to include target preheating, α-heating, radiation losses, ion and electron radial thermal conduction losses, and magnetic nozzle efficiency. Time steps and total run times are also defined. With these inputs, the model runs through a series of calculations at each time step, following the block diagram outlined in appendix A. The equations corresponding to each block function are described below.

3.1 Liner Radial Acceleration

For this initial simplified model, it is assumed that the target liner is incompressible and remains at a constant thickness during compression. This is a gross simplification compared to the SAMM model, which treats the liner as multiple shells with corresponding material equations of state and dynamics to estimate liner compression during implosion. With a rigid liner the current model will likely overestimate the amount of target compression and the corresponding energy release compared to the more realistic SAMM liner model. While a compressible shell model is being considered for a later version of the current model, the initial simplification of a rigid liner provides a useful starting point for analyzing performance trends.

Ignoring internal liner shell pressures, the radial acceleration of the fuel-liner interface $\left(\ddot{r}_{fl}\right)$ is given by

$$\ddot{r}_{fl} = \frac{P_f + P_{B_i} - P_{l_i}}{m_l / 2} \cdot 2\pi r_f L \tag{15}$$

and that of the liner-vacuum interface $\left(\ddot{r}_{lv}\right)$ is given by

$$\ddot{r}_{lv} = \frac{P_{l_v} - P_{B_v}}{m_l / 2} \cdot 2\pi r_l L \,, \tag{16}$$

where P_f is the isobaric (ideal gas) fuel pressure, P_{B_i} is the magnetic field pressure internal to the target, P_{l_i} is the liner pressure facing the fuel, P_{l_v} is the liner pressure facing the vacuum, P_{B_v} is the magnetic field pressure external to the target, m_l is the liner mass, r_f is the fuel radius, r_l is the external target radius (including liner), and L is the liner length. In this approximation, half the liner mass is attributed to the liner-fuel interface and half to the liner-vacuum interface. For an incompressible liner, $P_{l_i} = P_{l_v}$ and the radial acceleration of the fuel-liner interface is equal to the radial acceleration of the liner-vacuum interface. As such, equations (15) and (16) can be combined to provide an expression for the radial acceleration of the target liner:

$$\ddot{r}_l = \frac{2\pi L}{m_l}\left(P_f + P_{B_i} - P_{B_v}\right) r_l - \left(P_f + P_{B_i}\right)\Delta \,, \tag{17}$$

where Δ is the thickness of the (incompressible) liner. Pressure values are calculated for each time step, and the radial acceleration is updated. From this updated acceleration, the liner radial velocity and radial position can then be determined at each step.

3.2 Pressure Terms

The following are pressure terms:

- The isobaric fuel pressure is given by $P_f = \rho R T_f$, where ρ is the fuel mass density, R is the universal gas constant, and T_f is the fuel temperature.

- Magnetic field pressure internal to target:

$$P_{B_i} = \frac{B_i^2}{2\mu_0} \quad . \tag{18}$$

Here, B_i is the internal magnetic field strength and μ_0 is the permeability of free space. During target compression, the internal magnetic field increases as the initially trapped magnetic flux is compressed into an ever-shrinking radius. For an initial trapped magnetic field B_{i0} and target radius r_0, the magnetic flux φ_i confined within the uncompressed target is:

$$\varphi_i = B_{i0}\left(\pi r_0^2\right) \quad . \tag{19}$$

Assuming the magnetic flux remains constant during compression (no flux leakage), the magnetic field B_i at target radius r is then:

$$B_i = \frac{B_{i0}\left(\pi r_0^2\right)}{\pi r^2} = B_{i0}\left(\frac{r_0}{r}\right)^2 \quad . \tag{20}$$

For even modest compression ratios (r_0/r), an initially trapped magnetic field of a few to several Tesla within the target can significantly increase to axial field values sufficient for trapping fusion α particles and suppressing the radial thermal conduction of ions and electrons.

- Magnetic field pressure external to target:

$$P_{B_v} = \frac{B_v^2}{2\mu_0} \quad . \tag{21}$$

For the simple version of the code developed under Phase I, the vacuum magnetic field is assumed to consist of a gradient region followed by a maximum constant axial field within the coil. As noted in a prior section, the axial gradient is assumed to be linear to simplify the analytic model.

It is assumed that any magnetic flux external to the target does not penetrate the liner during compression (compression time << field diffusion time). The flux within the solenoid coil prior to target entry is given by:

$$\varphi_v = B_{v0}\left(\pi r_c^2\right), \tag{22}$$

where B_{v0} is the initial vacuum magnetic field within the coil and r_c is the solenoid coil radius. As the target enters the coil the flux will be compressed between the target liner and the internal coil wall:

$$\varphi_v = B_v \pi\left(r_c^2 - r_l^2\right). \tag{23}$$

For conserved flux, the displaced magnetic field external to the liner as the target traverses the coil is then given by:

$$B_v = \frac{B_{v0}\left(r_c^2\right)}{\left(r_c^2 - r_l^2\right)}. \tag{24}$$

For an initial target radius close to the inner coil radius, the compressed flux can significantly increase the magnetic field strength between the coil and target, in turn providing enhanced magnetic field pressure to compress the target.

3.3 Energy Terms

The total fuel energy changes during each time step due to multiple heating and cooling terms, which are described in detail in McBride and Slutz[30] and summarized below:

- Adiabatic heating $\left(\dot{E}_{ad}\right)$: The adiabatic heating rate is given by $\dot{E}_{ad} = P_f \dot{V}_f$, where P_f is the internal isobaric fuel pressure (defined above) and $\dot{V}_f$ is the change in fuel volume calculated at each time step.

- Fuel preheating $\left(\dot{E}_{pre}\right)$: As noted, several ground-based experiments and simulations have demonstrated significant improvements in final compressed fuel temperatures if the fuel is preheated prior to compression. In most cases, this is accomplished via pulsed, high-intensity laser illumination of the target to raise the fuel temperature several tens to hundreds of eV just prior to implosion. The SAMM code[30] includes laser preheating through a target window, simulating recent Sandia experiments. For this more simple initial model, the analysis includes an option to ramp the fuel temperature from an initial temperature to a user-defined temperature over a given time period. The time period can be adjusted to provide a temperature change before the target enters the gradient region, or during traversal of the region prior to the start of radial compression. While crude, it offers at least an initial ability to investigate the effects of preheated fuel temperatures on the performance of the concept.

• α particle heating $\left(\dot{E}_\alpha\right)$: If the axial magnetic field internal to the target is sufficiently strong at compression, the α particles released during D-T fusion will be trapped and deposit some fraction of their energy into the fuel. For a given α particle energy Q_α, the fraction f_α of energy deposited in the fuel is given by:[30]

$$f_\alpha = \frac{x_\alpha + x_\alpha^2}{1 + \frac{13x_\alpha}{9} + x_\alpha^2} \tag{25}$$

with

$$x_\alpha = \frac{8}{3}\left(\frac{r_f}{l_\alpha} + \frac{b^2}{\sqrt{9b^2 + 1{,}000}}\right) \tag{26}$$

and

$$l_\alpha = \left(4\pi\in_0\right)^2 \cdot \frac{3}{4\sqrt{2\pi}} \cdot \frac{m_\alpha v_{\alpha 0}\left(kT_f\right)^{3/2}}{\overline{n_e} Z_\alpha^2 q_e^4 m_e^{1/2} \ln\Lambda}\ , \tag{27}$$

$$b = \frac{r_f}{r_{\alpha L}}\ , \tag{28}$$

and

$$r_{\alpha L} = \frac{m_\alpha v_{\alpha 0}}{Z_\alpha q_e B_i}\ . \tag{29}$$

In the above, l_α is the mean free path of an α particle, m_α is the α particle rest mass, $v_{\alpha 0}$ is the initial velocity of the α particle $\left(=\sqrt{2Q_\alpha/m_\alpha}\right.$, where Q_α is the α particle energy), Z_α is the α charge (=2), $r_{\alpha L}$ is the α particle Larmor radius, and ln(Λ) is the Coulomb logarithm. Using these equations, the heating rate due to α particle energy deposition is then given by:

$$\dot{E}_\alpha = \dot{N}_{\text{D-T}} Q_\alpha f_\alpha\ , \tag{30}$$

where $\dot{N}_{\text{D-T}}$ is the D-T reaction rate, discussed in a later section.

• Radiative cooling: The initial radiative cooling term included in the simplified analytic model was limited to bremsstrahlung radiation, given by:

$$\dot{E}_r = 1.57\times 10^{-40}\, \overline{Z}_f \overline{n}_i \overline{n}_e \sqrt{\overline{T}_f}\ \cdot\left(\pi r_f^2 L\right), \tag{31}$$

which assumes a constant density and temperature over the entire fuel volume, and an optically thin volume emitter. This radiative model significantly overestimated the fuel cooling rates, and in many cases, overwhelmed the heating terms to prevent any temperature rise in the plasma. While circumstances can exist where radiative cooling can exceed adiabatic and other heating sources, the rapid radiative energy loss observed in several cases for the initial analytic model was somewhat suspect, leading to the need for a more accurate approach. As such, the gray radiation model discussed in McBride and Slutz[30] seemed a more suitable representation. The gray model incorporates two-temperature effects as well as liner radiation absorption and reemission. Due to the limited time remaining on the Phase I activity, a simplified version of the gray model was adapted for the current analysis. In this adaptation, the volume radiation (P_{rv}) is set equal to the gray body surface radiation (P_{rs}), with the terms defined as:

$$P_{rv} = A_{br} \cdot 2\pi L \cdot \bar{Z}_f \int_0^{r_f} n_i n_e \sqrt{T_f} \left[1 - \left(\frac{T_B}{T_f} \right)^4 \right] r\, dr \tag{32}$$

$$P_{rs} = \left(1 - \alpha_s\right) \sigma T_B^4 \cdot 2\pi r_f L \ , \tag{33}$$

where $A_{br} = 1.5 \times 10^{-40}$ m^3 K$^{-½}$ J/s, L is the length of the cylindrical fuel element, $\bar{Z}_f$ is the average ionization state of the fuel, $\sigma$is the Stefan-Boltzmann constant, T_f is the fuel temperature, T_B represents the brightness temperature, and α_s is the albedo of the liner's inner surface (typically ≥0.9). In the simple analytic model used here, the albedo is set to 0.9, and number densities and temperatures are assumed uniform over the fuel volume. With these approximations, the equations are set equal and the brightness temperature, T_B, is solved and used to determine the total radiated power at each time step.

- Thermal conduction cooling $\left(\dot{E}_{tc}\right)$: The SAMM code[30] differentiates fuel regions into a high temperature central hot spot and cooler shelf region, which provides a well-defined radial thermal gradient for thermal conduction to occur. The simplified model used here assumes a uniform volumetric fuel density and temperature, and instead uses an assumed linear radial thermal profile to approximate potential thermal conduction losses. In this instance, the energy loss rate due to electron thermal conduction is given by:[30]

$$\dot{E}_{tc,e} = 2\pi r L \cdot \kappa_e \cdot k \frac{\partial T_f}{\partial r} \approx 2\pi r L \cdot \kappa_e \cdot k \frac{T_f}{r} \approx 2\pi L \cdot \kappa_e \cdot k T_f \ , \tag{34}$$

where k is Boltzmann's constant, L is the target length, and κ_e is the electron thermal conduction coefficient perpendicular to the axial magnetic field internal to the target:

$$\kappa_e = \frac{n_e k T_f \, \tau_{ei}}{m_e} \cdot \frac{6.18 + 4.66 x_e}{1.93 + 2.31 x_e + 5.35 x_e^2 + x_e^3} \ . \tag{35}$$

Here, n_e is the electron number density, m_e is the electron rest mass, x_e is the electron Hall parameter, defined as $x_e \equiv \omega_{ce} \tau_{ei}$, where ω_{ce} is the electron cyclotron frequency and τ_{ei} is the average

electron-ion collision time. Similarly, for ions, the energy loss rate due to ion thermal conduction is given by:[30]

$$\dot{E}_{tc,i} = 2\pi rL \cdot \kappa_i \cdot k \frac{\partial T_f}{\partial r} \approx 2\pi L \cdot \kappa_i \cdot kT_f \tag{36}$$

with

$$\kappa_i = \frac{n_i k T_f \, \tau_{ii}}{\bar{m}_i} \cdot \frac{2.645 + 2x_i^2}{0.677 + 2.7x_i^2 + x_i^4} \ , \tag{37}$$

where n_i is the ion number density, $\bar{m}_i$ is the average ion mass, x_i is the ion Hall parameter, defined as $x_i \equiv \omega_{ci}\tau_{ii}$, ω_{ci} is the ion cyclotron frequency, and τ_{ii} is the average ion-ion collision time.

The total thermal conduction loss term is then given by:

$$\dot{E}_{tc} = \dot{E}_{tc,e} + \dot{E}_{tc,i} \ . \tag{38}$$

- End losses $\left(\dot{E}_{\text{end}}\right)$: Particles escaping from the ends of the target during compression constitute an additional energy loss term, as well as contributing to the loss of fuel mass. The expression for particle end losses is modeled after reference 30:

$$\dot{E}_{\text{end}} = 2 \cdot \left(\frac{3}{4}\right)^4 \frac{E_f}{V_f} \int_0^{r_f} c_f \cdot 2\pi r \cdot dr = 2 \cdot \left(\frac{3}{4}\right)^4 \frac{E_f}{V_f} c_f \cdot \left(\pi r_f^2\right) , \tag{39}$$

where

$$c_f = \left(\frac{\gamma_f \, p_f}{\rho_f} \right)^{1/2} \tag{40}$$

is the speed of sound in the fuel region and $\gamma_f = 5/3$ is the ratio of specific heats for an ideal gas. For this initial evaluation, it is assumed that particle losses are identical from each end of the target (yielding the factor of 2 in equation (39)) and that the fuel pressure and density are uniform throughout the fuel region. In addition to energy loss, the loss of particles from the ends of the target also creates a mass loss, which is further discussed in section 3.5.

3.4 Net Energy Change and Fuel Temperature

The combined effect $\left(\dot{E}_f\right)$ of the energy gain and loss terms is given by the expression:

$$\dot{E}_f = \dot{E}_{ad} + \dot{E}_{pre} + \dot{E}_{\alpha} - \dot{E}_r - \dot{E}_{tc} - \dot{E}_{end} \ , \tag{41}$$

which is evaluated at each time step to determine the net change in fuel energy. Multiplying $\dot{E}_f$ by the time step Δt yields the net energy change in the fuel for each time step. The cumulative energy in the fuel, E_f, is then calculated, and from that total energy, an average fuel temperature can be determined:

$$T_f = \frac{2E_f}{3k\left(N_{\mathrm{D}} + N_{\mathrm{T}} + N_e\right)}\,, \tag{42}$$

where N_{D}, N_{T}, and N_e are the total number of deuterons, tritons, and electrons in the fuel. The initial numbers and number densities of D and T are determined from the initial user-defined fuel density and volume, which provides the fuel mass, M_f. For this initial model, a 50:50 fuel mixture of D and T is assumed. For this approximation, the number of D and T atoms in the fuel is given by:

$$N_{\mathrm{D}} = N_{\mathrm{T}} = \frac{M_f}{\left(m_{\mathrm{D}} + m_{\mathrm{T}}\right)} \tag{43}$$

where m_{D} and m_{T} are the deuteron and triton masses, respectively. The fuel mass will change as a result of fusion events (fuel burnup), and N_{D} and N_{T} will change in equal proportion as each are consumed in the D-T fusion reactions. The rate of change for N_{D} and N_{T} are governed by fusion reaction rates, discussed below. The number of electrons is assumed to be given by $N_e = N_{\mathrm{D}} + N_{\mathrm{T}}$; as the fuel temperature rises above several electronvolts, the fuel becomes nearly fully ionized and each atom gives up one electron. A more detailed ionization model is being evaluated for inclusion in the model, but for this initial analysis, the approximation of full ionization due either to laser preheating or to adiabatic heating shortly after the start of target compression appears justified based on an initial Saha ionization analysis. The number of each species divided by the fuel volume provides the number density (n_s) for each species, which will change as the fuel volume changes during compression and as D and T ions are consumed by fusion reactions.

3.5 Fusion Reaction Rates

Consistent with the SAMM model, the D-T reaction rate used in the simplified model is:

$$\dot{N}_{\mathrm{D\text{-}T}} = L\int_0^{r_f} n_{\mathrm{D}} n_{\mathrm{T}} \langle \sigma v \rangle_{\mathrm{D\text{-}T}} \cdot 2\pi r \cdot dr\,, \tag{44}$$

where n_{D} and n_{T} are the fuel deuteron and triton number densities, respectively, and σv is the reactivity parameter for D-T reactions. For D-T, the reactivity parameter is calculated as:[30]

$$< \sigma v >_{\mathrm{D\text{-}T}} = C_1 \zeta^{-5/6} \xi^2 \exp\left(-3\zeta^{-1/3}\xi\right)\,, \tag{45}$$

$$\zeta = 1 - \frac{C_2 T_{f,\mathrm{keV}} + C_4 T_{f,\mathrm{keV}}^2 + C_6 T_{f,\mathrm{keV}}^3}{1 + C_3 T_{f,\mathrm{keV}} + C_5 T_{f,\mathrm{keV}}^2 + C_7 T_{f,\mathrm{keV}}^3}\,, \tag{46}$$

and

$$\xi = \frac{c_0}{T_{f,\,\mathrm{keV}}^{1/3}} \ , \tag{47}$$

where $T_{f,\mathrm{kev}}$ is the fuel temperature expressed in units of keV, and C_0–C_7 are fitting parameters used in SAMM and reproduced below for D-T fuel (table 1).

Table 1. Coefficients for reaction rate calculations (adapted from ref. 30).

Coefficient	DT Fuel
C_0	6.6610
$C_1\times10^{22}$	630.5
$C_2\times10^{3}$	15.136
$C_3\times10^{3}$	75.189
$C_4\times10^{3}$	4.6064
$C_5\times10^{3}$	13.500
$C_6\times10^{3}$	–0.10675
$C_7\times10^{3}$	0.01366

For the model presented here, the number density and temperature of the D-T fuel is assumed to be uniform, which simplifies the reaction rate to $\dot{N}_{D\,T\_fus} = n_D n_T \langle \sigma v \rangle_{DT} \pi r_f^2 L$. The rate at which the numbers of D and T ions are reduced due to fusion reactions is then given by:

$$\dot{N}_{\mathrm{D}\_fus} = \dot{N}_{\mathrm{T}\_fus} = -\dot{N}_{\mathrm{D\text{-}T}\_fus} \ . \tag{48}$$

Ignoring for now any secondary reactions, the rate at which deuterons and tritons are lost to D-T fusion reactions is also the rate at which neutrons are produced (one 14.1 MeV neutron per reaction), allowing the neutron number to be tracked for later fluence calculations.

As previously noted, particles will also be lost from the ends of the target during compression and heating, constituting an additional change in ion number and number density within the fuel region. The rate at which particles are lost from each end of the cylindrical fuel region are assumed here to be equal, and given by:[30]

$$\dot{N}_{\mathrm{D}\_\mathrm{ends}} = \dot{N}_{\mathrm{T}\_\mathrm{ends}} = -2 \cdot \left(\frac{3}{4}\right)^4 \int_0^{r_f} n_{\mathrm{D,T}} \cdot c_f \cdot 2\pi r \cdot dr = 2 \cdot \left(\frac{3}{4}\right)^4 \cdot n_{\mathrm{D,T}} \cdot c_f \cdot \left(\pi r_f^2\right) \ , \tag{49}$$

where again the factor of 2 accounts for particle losses from both ends and uniform pressure and density are assumed throughout the fuel region.

The rate at which particles are lost from the fuel region due to fusion reactions and end losses is then given by:

$$\dot{N}_{\mathrm{D}} = \dot{N}_{\mathrm{D\_fus}} + \dot{N}_{\mathrm{D\_ends}}$$

$$\dot{N}_{\mathrm{T}} = \dot{N}_{\mathrm{T\_fus}} + \dot{N}_{\mathrm{T\_ends}} \ . \tag{50}$$

The values of $\dot{N}_{\mathrm{D}}$ and $\dot{N}_{\mathrm{T}}$ are multiplied by the time step Δt and used to update the total ion number remaining at each time step

The fusion power at each time step is then estimated by:[30]

$$P_{\mathrm{D\text{-}T}} = \dot{N}_{\mathrm{D\text{-}T}} \cdot Q_{\mathrm{D\text{-}T}} \ , \tag{51}$$

which in turn is used to estimate the fusion energy released at each time step, $N_{\mathrm{D\text{-}T}} Q_{\mathrm{D\text{-}T}}$. This energy value is then summed over the total simulation time to provide the total energy yield, which is used to provide estimates of engine performance (sec. 2.4).

4. ANALYTIC MODEL: PRELIMINARY RESULTS

The simplified semi-analytic model was used to investigate the effects of various parameters on system performance; e.g., changing the initial target radius, density, and velocity; changing the strengths of the magnetic field gradient and maximum external axial field; and evaluating the impacts of the various heating and cooling terms discussed in section 3.3. The following sections discuss several key results in more detail, with a summary table of key trades and performance impacts provided in appendix B. Given the approximations made in the simplified analytic model, the quantitative values discussed below are likely optimistic. However, the trends appear reasonable and can be used to provide guidance for the more detailed numerical simulations to follow.

4.1 Model Check: Adiabatic Compression

As this is a new concept, there are no readily available codes or experiments against which to compare the analytic model results. A limited evaluation of model accuracy was performed by comparing the maximum predicted fuel temperature due to adiabatic compression against well-known analytic solutions for adiabatic compression heating. This provides some reassurance that key energy terms are being evaluated correctly, but again, an appropriate amount of caution should be used with the quantitative analytic model values presented in this TP.

An exact analytic expression for heating an ideal gas by adiabatic compression alone is given by:[31]

$$T = T_0 \left(\frac{r_0}{r} \right)^{4/3}, \tag{52}$$

where r_0 and r are the initial and compressed fuel radius, T_0 and T are the initial and compressed fuel temperatures, respectively. Three test cases were run to compare the adiabatic compression temperatures predicted by the model against the exact analytic expression. The value of the compression ratio calculated by the model was used along with the initial fuel temperature to determine the final fuel temperature per equation (52). In each case the target outer liner radius was set at 1 cm, liner thickness at 0.16 cm (for an aspect ratio of 6), external vacuum field at 30 T, gradient field at 100 T/m, and initial fuel density at 0.05 kg/m^3. Initial fuel temperature and initial internal magnetic field values were changed to affect the maximum compression ratio. Results of the trials are presented in table 2.

Table 2. Predicted and analytic adiabatic compression fuel temperatures for various initial conditions.

Initial Fuel Temperature (eV)	Initial Internal Magnetic Field (T)	Fuel Compression Ratio (Model)	Temperature (eV) at Compression (Model)	Temperature (eV) at Compression (Eq. (48))	Percent Difference
1	1	34.7	105	112.9	7
1	2	17.2	42.8	44.3	3.4
50	1	33.2	5.02×10^3	5.33×10^3	5.8

In general the semi-analytic model does well at predicting the fuel temperatures due to adiabatic compression. While the remaining terms do not lend themselves as easily to an analytic comparison, the results for the adiabatic heating term provide some confidence in the solutions presented for the semi-analytic model.

4.2 Initial Target Density

Changing the initial target fuel density changes not only the amount of fuel present in the target but also the compression dynamics. Low density targets may not provide sufficiently high reaction rates during compression for significant fusion to occur, limiting the yield. Conversely, high internal pressures generated in higher density targets at lower fuel temperatures may prevent significant compression and fuel heating, again limiting reaction rates and energy yield.

The initial target density was stepwise evaluated from a low of 0.01 kg/m^3 to a high of 0.1 kg/m^3. The initial target injection velocity was 10 km/s, the outer (Be) liner radius was 1 cm with an aspect ratio of 6 (liner thickness of 0.16 cm), and a target length of 5 cm. The initial fuel temperature was set to 1 eV with a maximum preheat temperature of 500 eV (occurring as the target traversed the gradient region). The maximum axial magnetic field produced by the coil was set to 30 T, with an axial gradient of 100 T/m; e.g., rising from 1 to 30 T in approximately 30 cm. The initial internal target axial magnetic field was set to 1 T. The only change in initial conditions for each run was the fuel density, and the impact on performance was primarily measured by the impact on yield, impulse, and I_{sp} for each pulse. The change in I_{sp} with initial target density is plotted in figure 7.

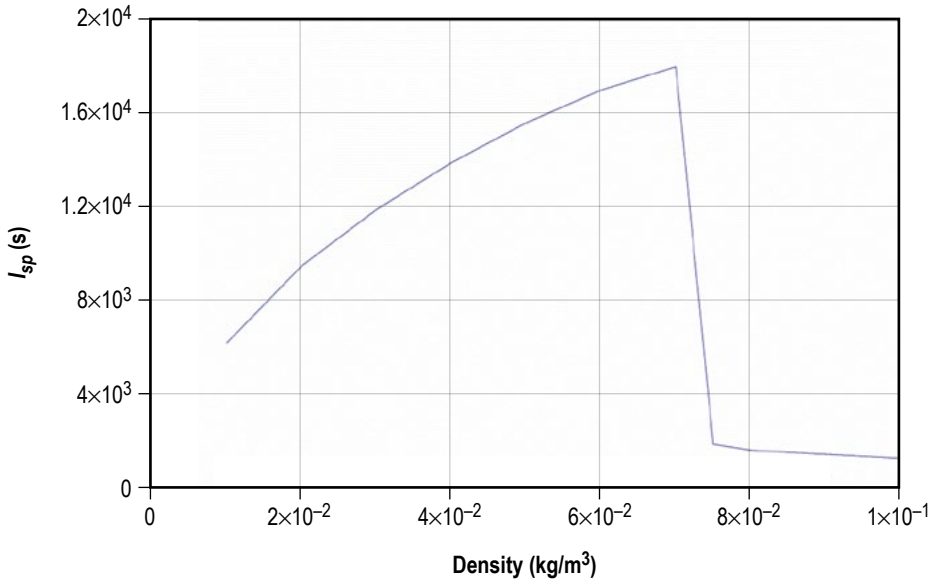

Figure 7. Specific impulse as a function of initial fuel density.

For the same initial conditions, the I_{sp} increases with increasing fuel density up to approximately 0.07 kg/m^3, at which point the I_{sp} rapidly decreases. Reviewing the runs at higher density values, the compressed fuel temperatures were limited to a few keV, too low for any significant fusion events to occur. As such, the target essentially underwent some radial compression but with no significant additional heating as it traversed the coil and exited the system. An initial target fuel density of around 0.07 kg/m^3 (0.07 mg/cc) thus appears close to optimum for the system under evaluation and was used for the subsequent performance trades discussed below.

4.3 Initial Target Radius

Keeping the density constant at 0.07 kg/m^3 and the other values as described above, the external target radius was sequentially changed from 0.75 to 2 cm. The aspect ratio (ratio of external target radius to liner thickness) was kept at $AR = 6$ for each run, corresponding to the minimum AR value for stability quoted in the literature. The impact of changing radius on performance parameters was then evaluated, and the change in I_{sp} as a function of target radius is shown in figure 8.

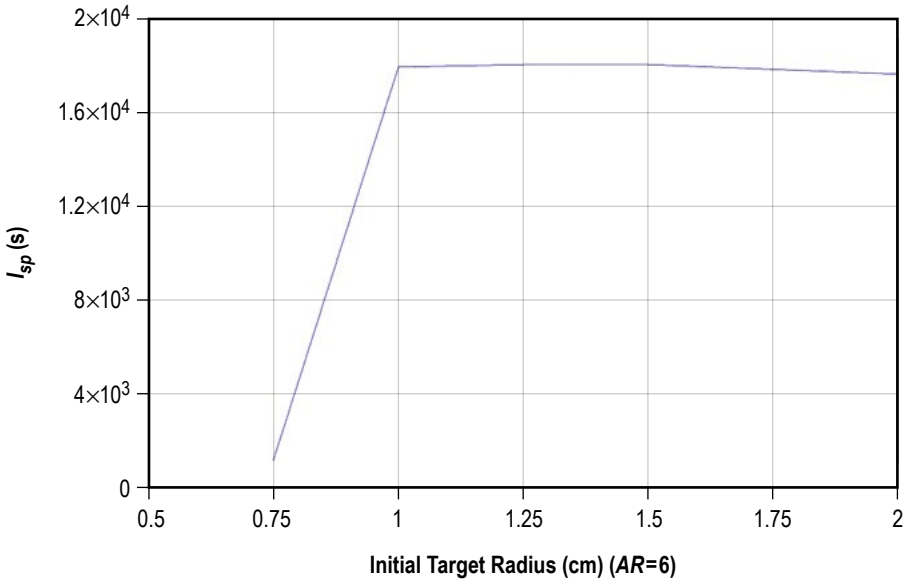

Figure 8. Specific impulse as a function of initial target radius.

As shown in the figure, the I_{sp} rapidly increases over a small change in initial radius, changing from approximately 1,000 s at 0.75 cm to a value approaching 18,000 s at a target radius of 1 cm, after which there is no significant change in performance with increasing target radius. As noted in appendix B, the yield at an initial target radius of 0.75 cm is approximately 4 orders of magnitude lower than the yield for target radii larger than 1 cm. For the assumed parameters, the small radius target was unable to reach the required compression densities and temperatures for significant fusion events to occur.

4.4 Initial Target Velocity

As described in section 1, the rapidly time-changing magnetic field used in standard θ-pinch experiments to induce a target liner current and cause compression (or equivalently to generate a compressive axial magnetic field external to the liner) is replaced in this system with a conductively lined fuel target injected at high velocity along the axis of a superconducting coil. The combination of axial velocity and axial magnetic field gradient provides an effective time-changing magnetic field in the target frame of reference. As discussed in section 2.3, the time it takes the axial magnetic field to diffuse through the conductive liner is longer than the target compression time, and the unbalanced external pressure causes the target to implode. To evaluate the impact of initial target velocity on system performance, the target velocity was evaluated from 2 to 20 km/s, assuming a constant magnetic field gradient of 100 T/m. The initial target density was 0.07 kg/m^3 and the radius was set to 1 cm for each run, with all other values the same as above. The results of changing the initial target velocity on I_{sp} are shown in figure 9.

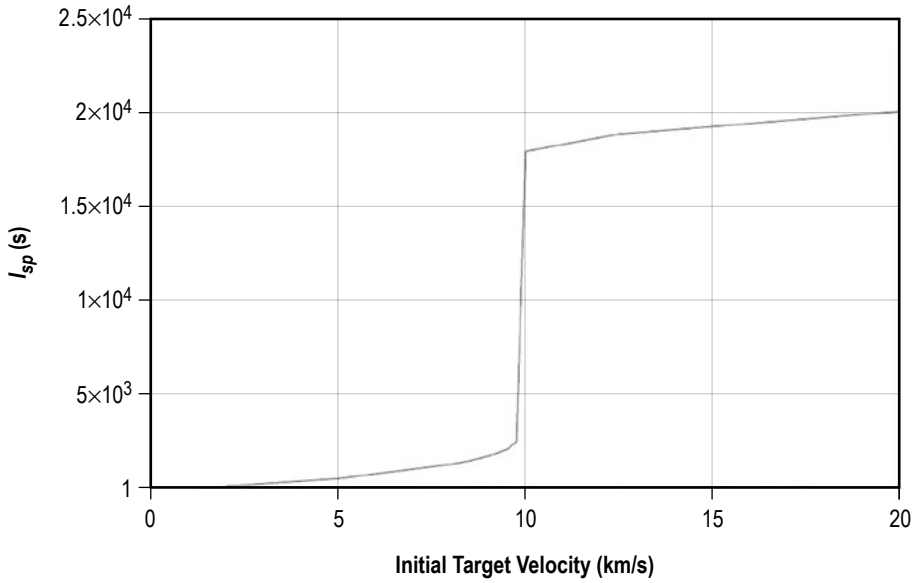

Figure 9. Specific impulse as a function of initial target velocity.

For low target velocities, the I_{sp} remains approximately equal to that of the initially accelerated target, traversing the systems without additional energy gain. However, at approximately 10 km/s, there is significant additional energy gain from fusion events, with the I_{sp} rapidly increasing to approximately 18,000 s, and then slowly increasing at higher initial velocities. At the lower injection velocities, the apparent change in magnetic field does not sufficiently increase rapidly for significant compression to occur. At around 10 km/s, the changing magnetic field in the target frame of reference is sufficient to compress the target and initiate fusion, providing rapid additional energy gain and a correspondingly large increase in I_{sp}. Beyond 10 km/s, there is minimal additional gain, accounting for the slower increase in I_{sp} with increasing initial velocity. To minimize the amount of laser power required to accelerate the target, it appears that providing an initial target velocity of 10 km/s may be sufficient to enable I_{sp} values of interest.

4.5 Target Preheating

Prior studies have shown the benefit of preheating the target fuel prior to compression to reduce the amount of compression required to reach fusion temperatures. To evaluate the effect of initial fuel temperature on performance, it was assumed that once the target reaches its injection velocity, a second high-energy laser pulse would be focused on the aft end of the target to generate a specified amount of heating as the target traversed the gradient field region (sec. 3.3). To evaluate the effect of fuel preheating on performance, the amount of preheating was varied from 50 to 750 eV, assuming a uniform temperature distribution within the fuel region. The initial target density was 0.07 kg/m^3, with an outer radius of 1 cm and initial injection velocity of 10 km/s. The remaining values are the same as above. The impact on I_{sp} by laser preheating of the fuel is shown in figure 10.

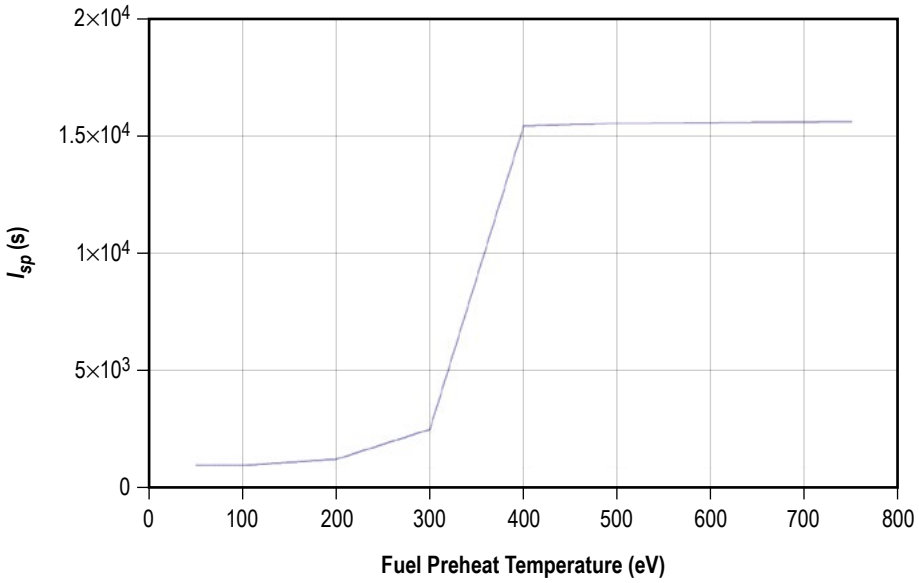

Figure 10. Specific impulse as a function of uniformly preheated fuel temperature.

For initial fuel temperatures below approximately 300 eV, very little additional energy gain is provided by the system. The compression of the target is insufficient to raise the initial temperature high enough for significant amounts of fusion to occur. Between 300 and 400 eV, the I_{sp} rapidly increases as the compressed fuel conditions begin to support gainful fusion. Above roughly 400 eV, there is no significant increase in I_{sp} with increasing initial fuel temperature for otherwise identical targets. Higher initial fuel temperatures would require a commensurate increase in laser heating power, with little additional benefit to system performance. Hence, preheating the target to approximately 400 eV appears sufficient to generate a significant fusion yield on compression.

4.6 External Magnetic Field

The magnetic field produced by the superconducting solenoid coil creates the external axial magnetic field required to maintain inward radial pressure on the target during compression and heating. To evaluate the effect of external magnetic field strength on performance, the value of the maximum axial magnetic field was varied from 5 to 50 T. For these runs, the initial fuel density, radius, and target velocity were 0.07 kg/m^3, 1 cm, and 10 km/s, respectively, with a fuel preheat temperature of 500 eV. A magnetic field gradient of 100 T/m was assumed in all cases. The results of changing the maximum external magnetic field on I_{sp} are plotted in figure 11. Below approximately 30 T, there is little increase in I_{sp} beyond that of the uncompressed target exiting the system. At approximately 30 T, sufficient radial compression is achieved to initiate substantial fusion reactions, resulting in a significant increase in energy yield and corresponding increase in directed exhaust velocity, again assuming a 70% magnetic nozzle conversion efficiency. Increasing the external magnetic field beyond 30 T does not significantly increase the I_{sp} and would require more advanced steady-state superconducting magnets than currently available. While higher external compression fields can be achieved using pulsed coils, the intent of the current study was to assess the viability of a steady-state superconducting magnet to alleviate the mass and complexities associated with high current pulsed power delivery systems. It appears that an axial magnetic field of approximately 30 T, currently at the limit of available superconducting magnet technology,[27] may be sufficient for the concept to work.

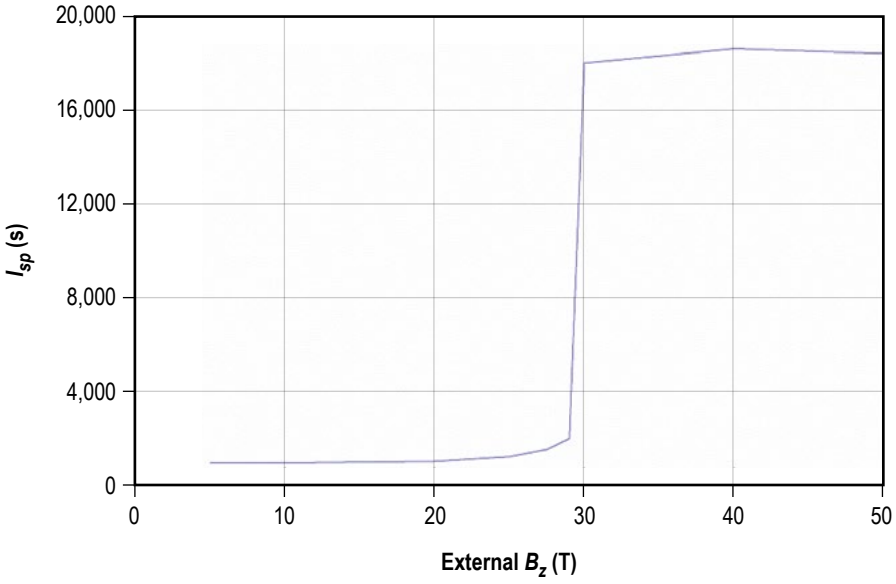

Figure 11. Specific impulse as a function of axial magnetic field external to the target.

4.7 Internal Target Magnetic Field

As noted in the prior discussion of pressure and energy terms (sec. 3), an initial axial magnetic field within the target prior to compression will increase as the square of the compression ratio (eq. (20)), assuming no magnetic field diffusion through the target occurs during the compression time. To evaluate the effect of initial internal magnetic field strengths on system performance, the internal magnetic field was varied from 1 to 5 T. The impact on I_{sp} is plotted in figure 12.

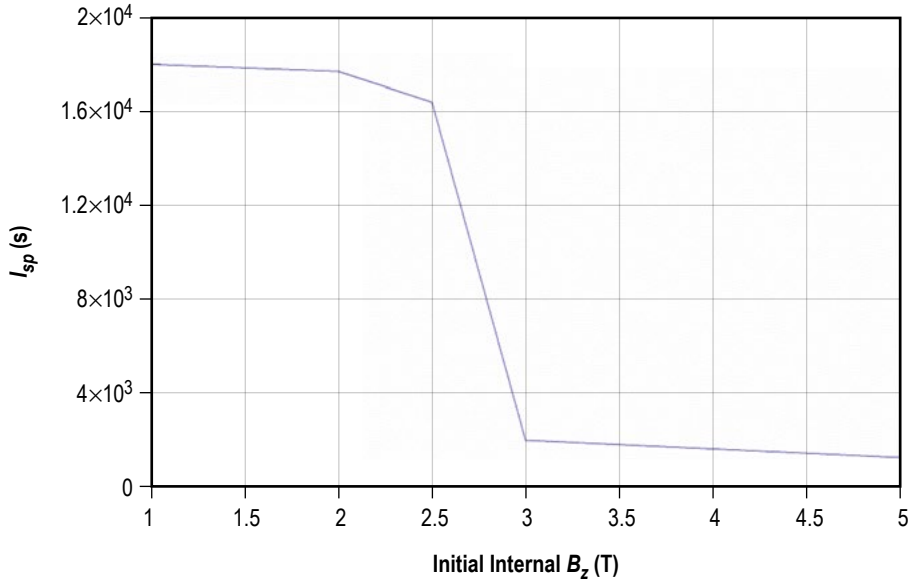

Figure 12. Specific impulse as a function of initial target internal magnetic field.

It is seen that the I_{sp} drops off fairly rapidly for initial internal target magnetic fields above approximately 2.5 T. An inquiry of the code results shows that above this value, and for the target and external magnetic field parameters described above, the maximum radial fuel compression is lower for higher initial target internal magnetic fields. As a specific comparison, the simple analytic model predicts a maximum fuel compression ratio of around 14 with an initial internal field of 2.5 T, while the compression ratio is closer to 6 with an initial internal field of 5 T. The lower amount of compression corresponds to a lower maximum fuel density and temperature, resulting in less fusion reactions, lower yield, and lower I_{sp}. An internal magnetic field of approximately 1 T appears to provide a suitably high field on compression to mitigate radial thermal conduction and provide trapped α particle heating.

4.8 Magnetic Field Gradient

As discussed in section 1, the concept uses a stationary magnetic field and rapidly injected target to generate the compression dynamics of more standard θ-pinch geometries. The axial target velocity and magnetic field gradient combine to mimic a rapidly time-changing magnetic field in the moving target frame of reference, creating the conditions necessary for radial compression. Assuming a 10-km/s initial target velocity, 30-T external axial magnetic field, 1-T initial internal magnetic field, and a 1-cm radius, 0.07-kg/m^3 target preheated to 500 eV (used for consistency during the trade study), the impact of magnetic field gradient on I_{sp} is plotted in figure 13.

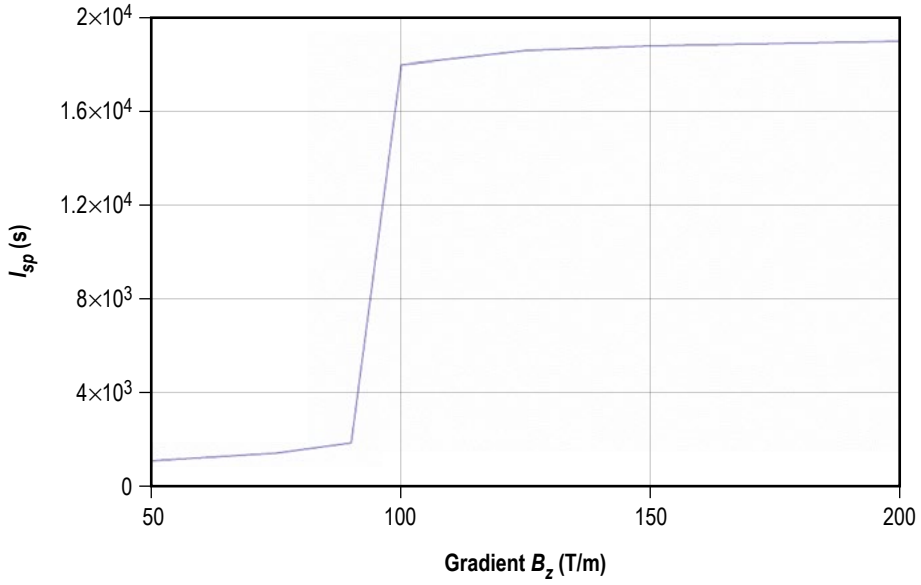

Figure 13. Specific impulse as a function of axial magnetic field gradient.

The axial gradient of the magnetic field provided by the superconducting coil was varied from 50 to 200 T/m, with a sharp increase in I_{sp} observed for a gradient field value of around 100 T/m. At this value, the combination of initial target velocity and magnetic field gradient generated sufficient target compression for fusion reactions to occur, resulting in significant energy gain and a rapid

increase in I_{sp}. Above 100 T/m, the energy produced by the target (assuming the same initial density, radius, etc.) does not significantly increase, but an inquiry of the code results shows the time to reach maximum compression was shorter (e.g., approximately 42 μs at 100 T/m versus 32 μs at 200 T/m). The combination of target velocity and higher field gradient appears equivalent to a higher rate of change of magnetic field in the target frame of reference, resulting in more rapid radial compression.

4.9 Liner Material

Finally, the simplified model was run with three different types of liner material: Al, Be, and Li, to evaluate the effect of liner mass on target compression and corresponding system performance. The runs described in the sections above were performed with a Be liner, which is a good neutron reflector. The literature also reports models and experiments using Li and Al liners, so these were also evaluated in a limited set of runs for comparison with Be. No attempt was made to evaluate the various radiative or reflective properties of each liner; the comparisons were strictly to observe the effects of different liner densities on target compression. The set of generally optimized values found in the preceding sections, summarized here, were used in each liner simulation (table 3).

Table 3. Target and magnetic field values used in liner material evaluation.

Initial Fuel Density	Initial Liner Radius	Aspect Ratio	Injection Velocity	Fuel Preheat Temperature	External B-Field	Initial Internal B-Field	Axial B-Field Gradient
0.07 kg/m^3	1 cm	6	10 km/s	500 eV	30 T	1 T	100 T/m

To evaluate the effect of liner material on system performance, plots were obtained not only for I_{sp} (fig. 14) but also for the yield (fig. 15) and impulse (fig. 16) provided per pulse.

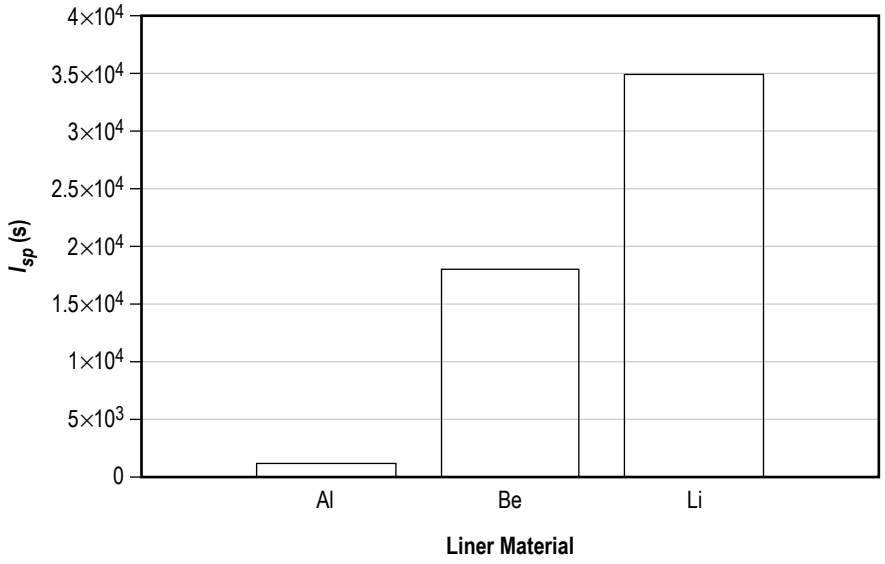

Figure 14. Specific impulse as a function of target liner material.

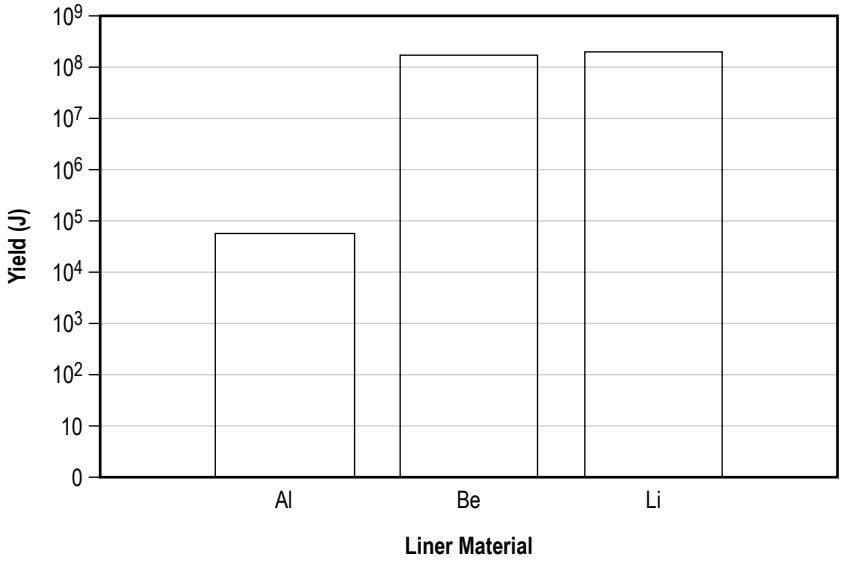

Figure 15. Yield as a function of target liner material.

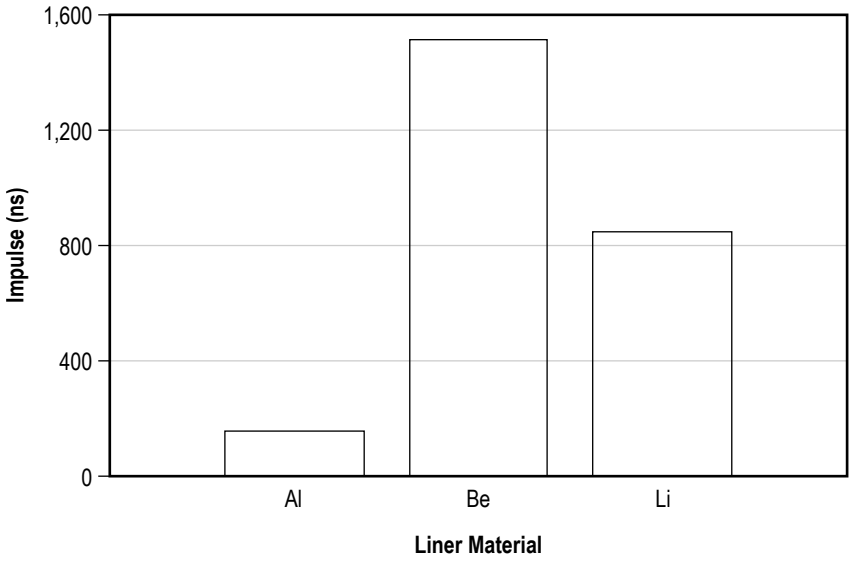

Figure 16. Impulse as a function of target liner material.

Of interest, the Al liner did not achieve a significant energy yield under the assumed target and magnetic field conditions, while both the Be- and Li-lined targets reached similarly high-energy yields (1.7×10^8 J and 1.95×10^8 J, respectively). Because the Al liner did not achieve any appreciable energy gain, the I_{sp} was similar to that of the initially accelerated target traversing the system. In the remaining two cases, the I_{sp} increases as the liner material density decreases; e.g., the Be-lined target delivered approximately 18,000 s, compared to roughly 34,900 s for the Li-lined target. The

target properties outlined above correspond to a Be liner mass of 8.6×10^{-3} kg and Li liner mass of 2.47×10^{-3} kg. The D-T fuel mass in each case is approximately 7.76×10^{-7} kg; hence, the target mass is dominated by the liner mass. Because the liner mass makes up the bulk of the total target mass, higher mass targets will have a lower directed exhaust velocity than lower mass targets for a given yield energy. The impulse delivered for each case shows the Li-lined target has a lower impulse than the Be-lined target (845 N-s versus 1,510 N-s, respectively), which again is primarily due to the lower mass of the Li liner. Per equation (12), the impulse is directly proportional to the exhaust mass and I_{sp}. Substituting the values of mass and I_{sp} for each target into that equation provides the impulse values noted in figure 16. Based on the analytic model predictions, a Li liner provides roughly a factor of 2 increase in I_{sp} but about half the impulse of a Be liner for an otherwise similar D-T target.

4.10 Pulse Considerations

The results presented above were obtained assuming a total run time of 100 μs for each case. However, the target may undergo compression followed by rapid expansion and a subsequent second compression during longer simulation periods, as shown in figure 17. The latter compression cycle in the model results from the target cooling on expansion to the point where external magnetic field pressure on the axially moving target can again cause contraction. This is most likely an artifact of the simplified analytic model. But even were it to physically occur, it would be more desirable to have the initial rapid expansion of the high temperature target (at this point a hot, radiating plasma) occur in the magnetic nozzle to provide directed thrust rather than a rapid expansion within the confined bore of the superconducting coil.

As shown in figure 17, the first compression cycle reaches a minimum radius at a time of approximately 41.5 μs (the time between the target entering the magnetic field gradient and the time for maximum compression to occur). At this point the target begins to expand, and if located in the magnetic nozzle, the radially expanding plasma would be redirected to provide axial thrust. This indicates that the superconducting coil preceding the magnetic nozzle should be relatively short. For an initial target velocity of 10 km/s, the magnet coil will be just over 0.4 m long. While this estimate needs to be verified with more detailed numerical modeling, it does indicate that reasonable superconducting magnet sizes and field strengths may be employed for the concept.

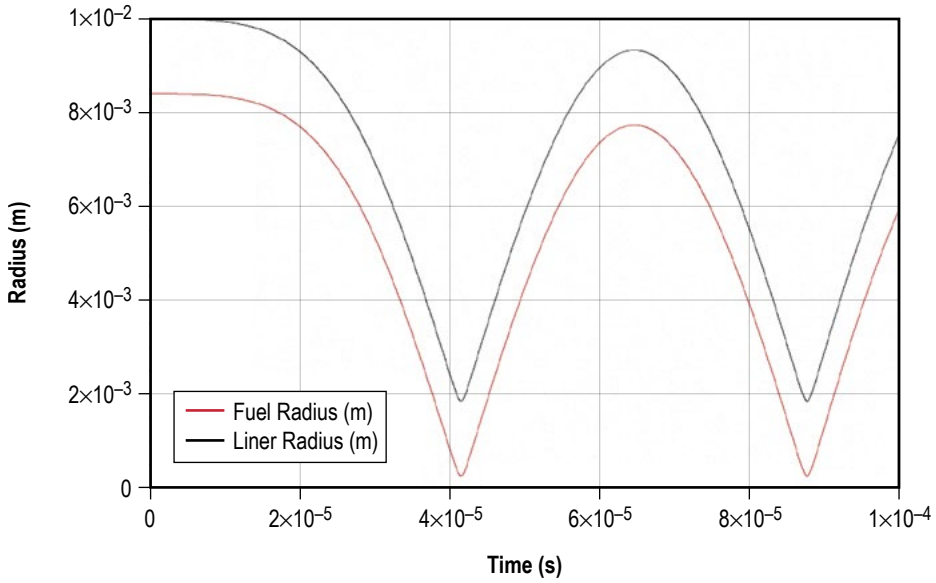

Figure 17. Target radius compression, expansion, and subsequent compression cycle.

Although the initial compression time for the target is on the order of several tens of microseconds, the period over which the target is accelerated to its axial injection velocity can be significantly longer, subject to the engine's pulse repetition frequency. Returning to section 2.2, a rough estimate can be made of the time required to accelerate the target to the desired injection velocity. The ablative acceleration model[25,26] discussed in that section also derives the acceleration time (t) as a fraction of the time required to fully burn through the ablative target material (t_b), which is related to the fraction of remaining target mass (m_f) to initial target mass (m_0):

$$\left(1-\frac{t}{t_b}\right)=\frac{m_f}{m_0}\,. \tag{53}$$

The burn time is given by:

$$t_b=\left(\frac{L_0}{C_c}\right)\left(\frac{n_0}{n_c}\right), \tag{54}$$

where L_0 is the target diameter, C_c is the sound speed of the target material at the critical density n_c, and n_0 is the initial density of the ablated material. The critical sound speed is given by:

$$C_c=\left(\frac{I}{2n_c m_i}\right)^{1/3}, \tag{55}$$

where I is the incident laser intensity (W/m^2), and m_i is the mass of an ablated ion (in this case, Be). From section 2.2, the critical density for a CO_2 laser is $n_c = 2.52 \times 10^{23}$ m^{-3}. The density of Be is 1,850 kg/m^3, and the ion mass is 1.5×10^{-26} kg, for an initial number density of 1.23×10^{29} m^{-3}. Following section 2.2, a laser power of 10 kW provides a laser intensity on a 1-cm radius target of 3.14×10^7 W/m^2. Equation (7) then predicts a velocity of 1.8×10^5 m/s for the ablated Be ions. Substituting this into equation (8) indicates approximately 9% of the Be liner material was ablated to reach the required injection velocity of 10 km/s. Using equation (55), the critical sound speed is equal to 1.1×10^3 m/s, and assuming a 10^{-2}-m radius target, equation (54) then yields a burn time of 8.8 s. From equation (53), the time required to accelerate the target, with $m_f/m_0 = 0.91$, is 0.76 s, substantially longer than the desired 0.1 s acceleration period. This indicates the laser power must be increased to more rapidly accelerate the target. Redoing the above calculations and assuming a laser power of 1 MW results in a laser intensity on target of 3.2×10^9 W/m^2. The corresponding critical sound speed is 7.5×10^3 m/s, and the ablated material velocity is 1.84×10^6 m/s. The ratio of final to initial mass from equation (8) is 0.991, indicating that about 1% of the target mass is ablated to reach the desired 10 km/s injection velocity with the 1 MW laser. Using equation (54), the burn time is approximately 1.3 s, and from equation (53), the acceleration time is predicted to be 1.17×10^{-2} s, or roughly 12 ms. Similar calculations using Li as the ablative material show that a similar amount of ablative mass (~1%) is required to reach an injection velocity of 10 km/s with the 1 MW laser, but over a shorter acceleration period of 3.6 ms. Although very crude estimates, the analysis indicates that a sufficiently high-power laser incident on a Be- or Li-lined target for several milliseconds will rapidly ablate a small fraction of the liner material, providing sufficient axial acceleration of the target into the gradient field on a time scale suitable for multi-Hertz pulsed operation.

4.11 Optimized Case

Based on the trades described above, an initial set of 'optimum' target and magnetic field values were defined to help guide more detailed SPFMaX numerical simulations of the D-T target implosion physics and associated vehicle and mission designs. These values were used in additional runs of the analytic model with an abbreviated simulation time of 45 μs to capture target compression and the subsequent start of target dissociation/expansion. Separate runs were conducted for Li- and Be-lined D-T targets with otherwise identical target and magnetic field values to estimate the potential range of engine performance. Figures 18–24 provide comparisons of several key parameters for the Li- and Be-lined targets.

As shown in figure 18, the external magnetic field applied by the superconducting coil is assumed constant for each case, with an axial gradient of 100 T/m leading to a maximum value of 30 T within the coil. During compression, the initial 1-T axial field within the Li-lined target briefly reaches a maximum compressed value of approximately 730 T, while the internal axial field within the Be-lined target reaches a maximum value of around 1,100 T due to a slightly higher amount of fuel compression, as seen in figure 19.

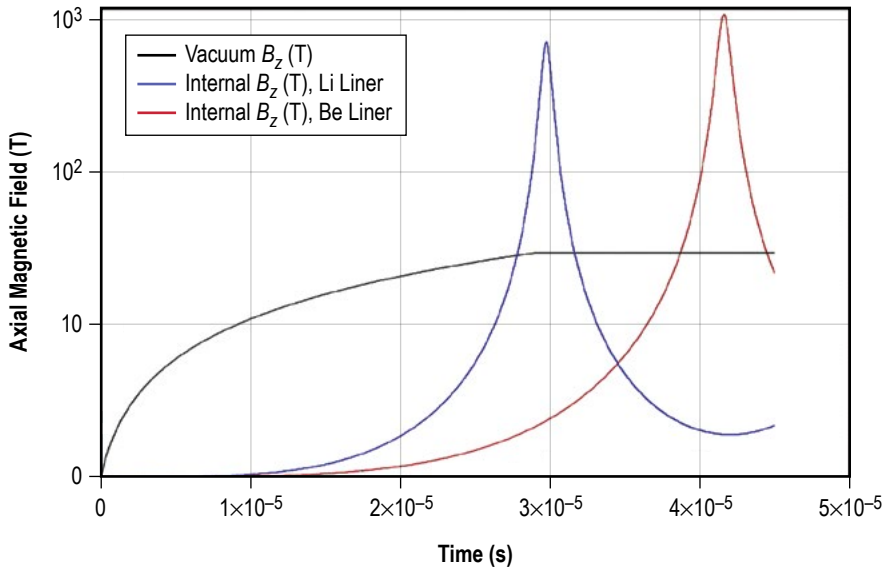

Figure 18. External and internal magnetic field values for Be- and Li-lined targets.

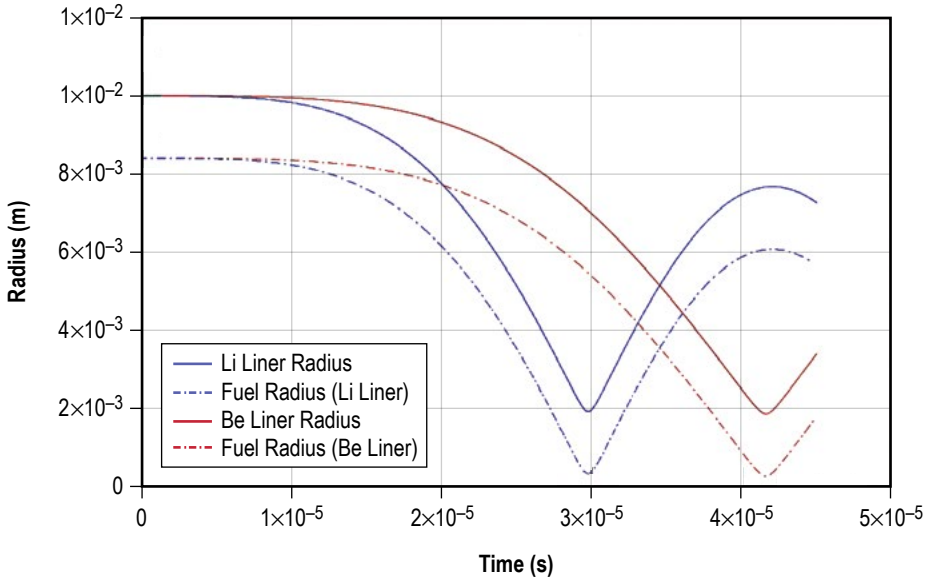

Figure 19. Evolution of liner and fuel radius with time.

Of interest, the Li-lined target reaches maximum compression at an earlier time than the Be-lined target. This is due to a more rapid radial acceleration of the lower mass Li liner for a given compression force compared to the Be-lined target.

Figure 20 displays the evolution of the D-T fuel density during compression. For the Li-lined target, the fuel density increases from the initial 0.07 kg/m^3 to a value of approximately 37 kg/m^3, while for the Be-lined target ,the fuel density increases to a value of 57 kg/m^3 before the target begins to expand. Figure 21 displays the evolution of the D-T ions due to fusion and end losses during compression (sec. 3.5). For a 50:50 mixture of D-T, the evolution of ion number is identical for each species.

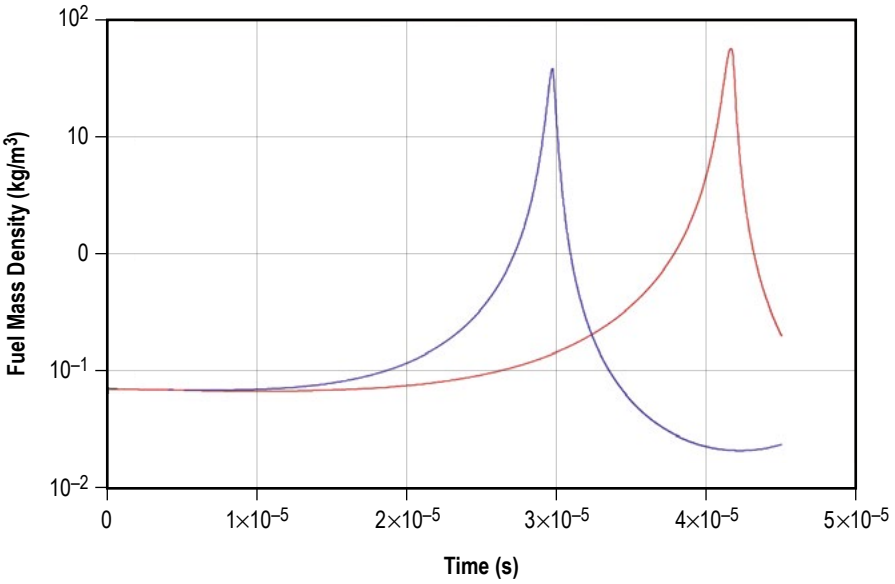

Figure 20. Evolution of D-T fuel mass density with time.

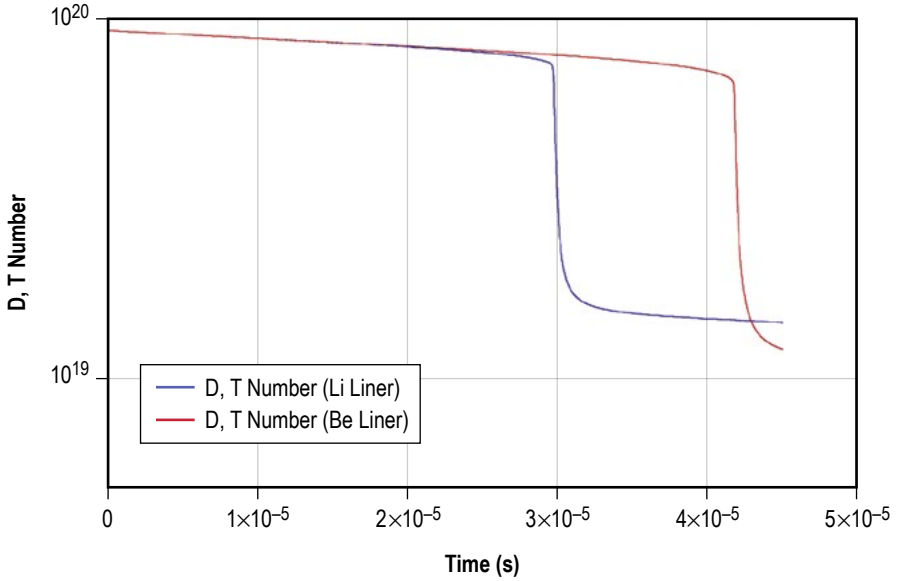

Figure 21. Evolution of number of D-T ions with time.

Figure 22 shows the evolution of the D-T fuel temperature as the target is compressed, with an expanded vertical scale to more clearly show the evolution. In each case there is an initial temperature increase from 1 to 500 eV due to laser preheating, followed by heating due to adiabatic compression and a rapid increase in temperature as fusion begins to occur and the energy of the resulting α particles is trapped within the target and contributes to the rising fuel temperature. As the temperature rapidly increases, the internal fuel pressure eventually exceeds the compressive magnetic field force to cause the target to expand, reducing the internal fuel temperature.

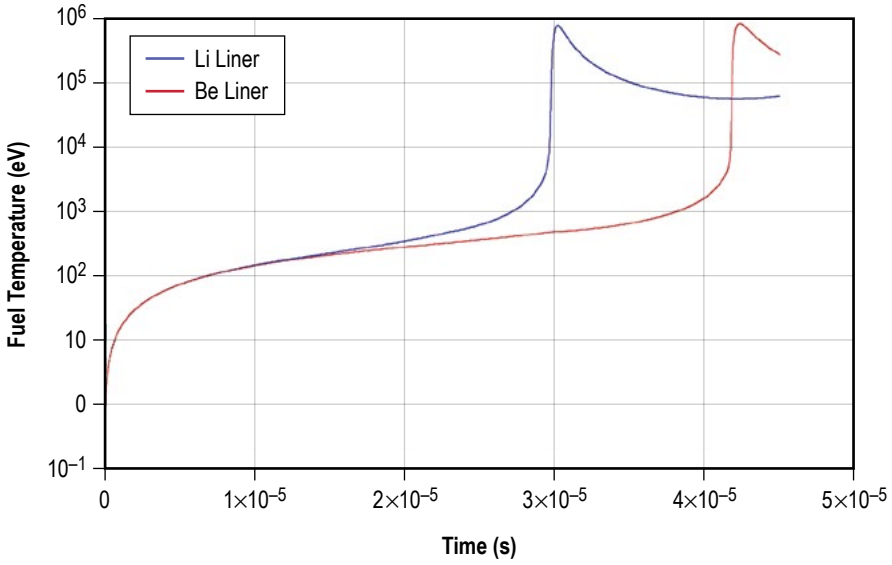

Figure 22. Evolution of D-T fuel temperature with time.

Figure 23 displays the areal density of the fuel during compression and subsequent expansion, where the fuel areal density is equal to the fuel mass density multiplied by the fuel radius (ρR). Upon compression, the Li-lined target reaches a maximum ρR value of 0.12 g/cm^2 (1.2 kg/m^2), while the Be-lined target reaches an areal density of approximately 0.14 g/cm^2 (1.4 kg/m^2). These values (and corresponding fuel temperatures) are comparable to the ρR values for net energy production shown in the Lindl-Widner plot of figure 4.

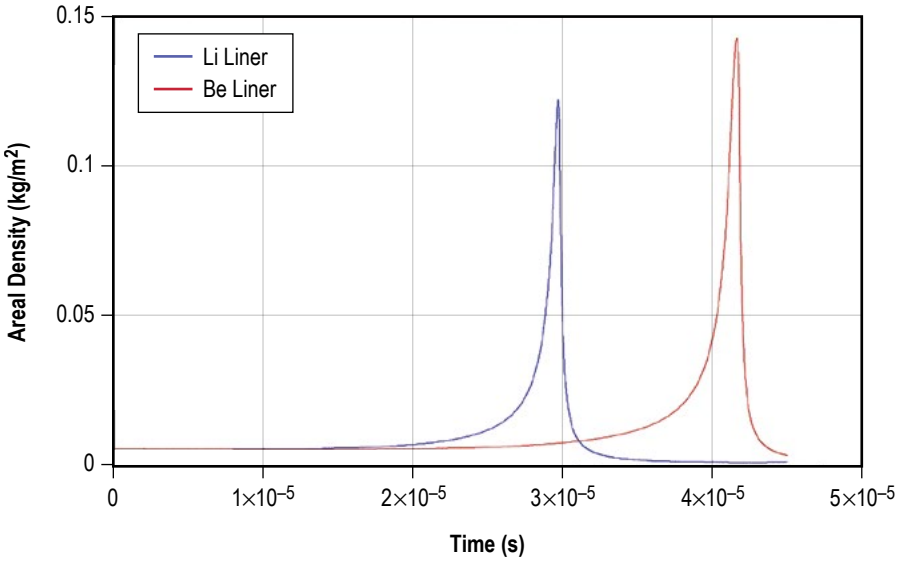

Figure 23. Evolution of fuel areal density (ρR) with time.

Figure 24 displays the cumulative fusion yield produced for each target. Upon ignition, the D-T fuel rapidly generates energy in the form of α particles and neutrons, with a combined energy release of 17.6 MeV (2.8×10^{-12} J) per fusion event.

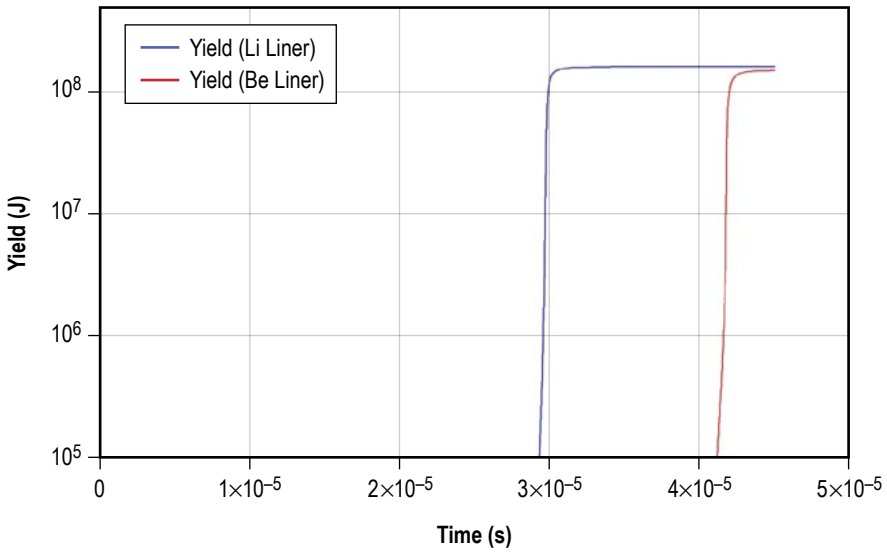

Figure 24. Cumulative target yield as a function of time.

For sufficiently strong internal magnetic fields, the α particle energy (3.5 MeV) is deposited in the fuel and contributes to a rapid increase in the fuel temperature. If not absorbed or reflected by the liner material, the 14.1 MeV neutron may escape the target and impact the surrounding magnet or support structure, depositing energy and causing embrittlement which must be taken into account in vehicle designs. The amount of neutrons produced during fusion and the cumulative amount of neutrons produced in each compression cycle are plotted in figures 25 and 26.

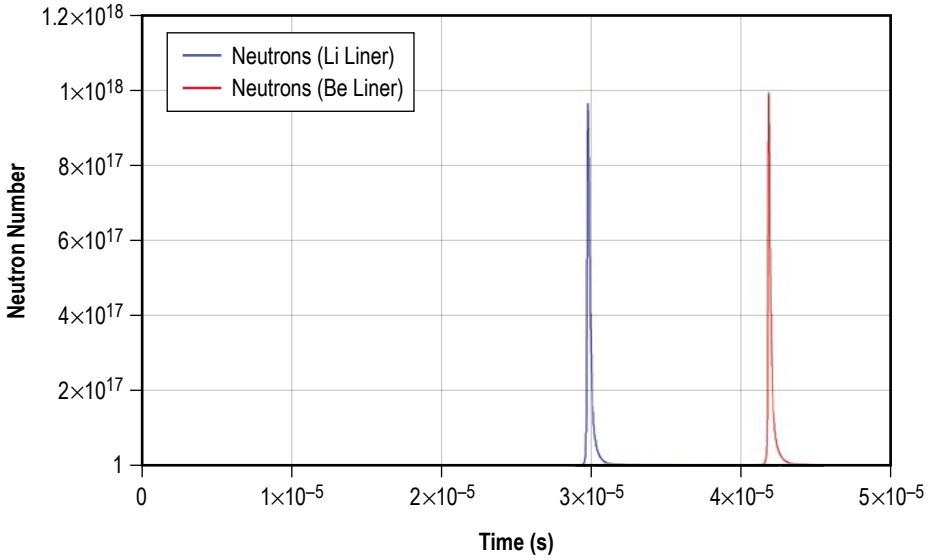

Figure 25. Evolution of neutron production with time.

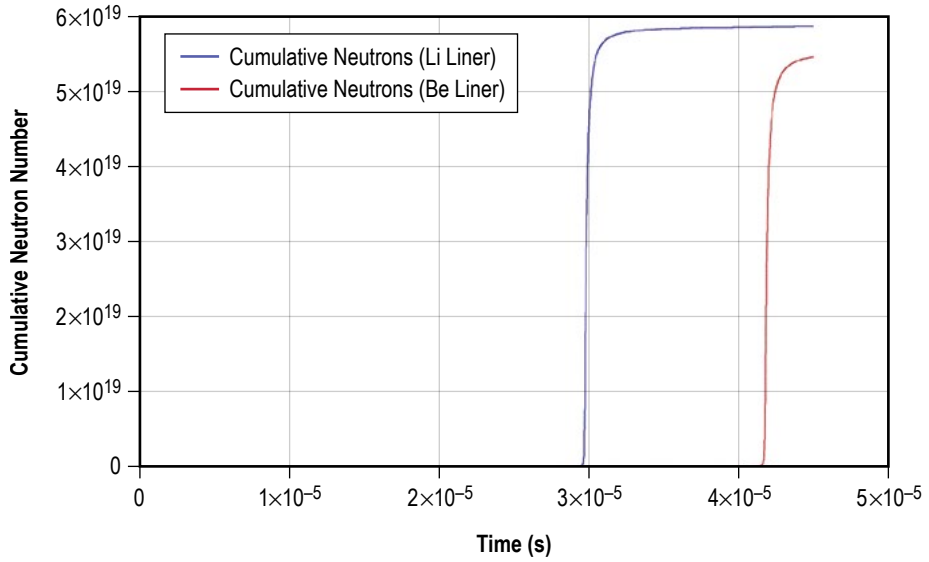

Figure 26. Cumulative neutron production with time.

In each case a copious amount of neutrons are produced, approximately 5.8×10^{19} neutrons in the case of the Li-lined target and 5.4×10^{19} neutrons for the Be-lined target. The energy carried by these neutrons is 1.3×10^{8} and 1.2×10^{8} J, respectively, representing a significant deposition of energy into the surrounding structure during each pulse.

4.12 Summary

The key performance results of this section are summarized in table 4, which displays the optimized target and magnetic field values assumed in these final analytic runs and the corresponding estimates of engine performance. Although the results are undoubtedly optimistic given the simplifying assumptions made in the model, they serve as an initial guide for the more detailed numerical simulations to follow.

Table 4. Engine performance estimates for optimized target and magnetic field values.

Initial Fuel Density	Initial Liner Radius	Aspect Ratio	Injection Velocity	Fuel Preheat Temperature	External B-Field	Initial Internal B-Field	Axial B-Field Gradient
0.07 kg/m^3	1 cm	6	10 km/s	400 eV	30 T	1 T	100 T/m
Specific Impulse (s)		**Impulse (N-s)**		**Yield (J)**		**Gain (100% Efficiency)**	
Li Liner	Be Liner	Li Liner	Be Liner	Li Liner	Be Liner	Li Liner	Be Liner
32,200	17,145	780	1,445	1.65×10^{8}	1.53×10^{8}	982	323

5. SPFMaX THREE-DIMENSIONAL NUMERICAL MODEL

The primary simulation tool being developed under the Phase I NIAC effort is the Smooth Particle Fluid with Maxwell Equation Solver (SPFMaX), a 3D smooth particle hydrodynamic (SPH) numerical method.[32] SPH is similar to other finite difference or finite element approaches to solving mass, momentum, energy, and Maxwell equations in that a set of discrete points are used to calculate the time rate of change of a model's properties in one, two, or three dimensions. The SPH method was chosen in the development of SPFMaX because it conserves mass exactly and does not require a grid to subdivide the domain. This feature makes SPH an attractive method for modeling closed systems with fixed amounts of mass, such as the gradient field pellets. A set of particles defines the shape and properties of the pellet and enables 3D simulations with a laptop in a matter of minutes or a few hours. In spite of the criticisms frequently applied to the SPH method, SPFMaX resolves shocks, heat transfer, viscosity, radiation, etc., and thus far has done so on various test cases to within 10% accuracy for 3D problems. SPFMaX is considered an effective design tool for supporting fusion and other advanced propulsion experiments.

For completeness, the theory behind SPFMaX is included below. At the heart of the code is the kernel approximation, which is common to all SPH methods, where properties are modeled with

$$A_a(r) = \int A(r')W(r-r', h)\, dr' \,, \tag{56}$$

where A is any property (like temperature, pressure, etc.), subscript a means point a, r is the position of point a in space, and W is the interpolating kernel function. In the limit that $h \to 0$, W becomes the direct delta function and the expression becomes exact. Any function can be approximated in this way, and this is the first assumption of SPH. The second is to replace the integral with a summation,

$$A_a = \sum_b A_b V_b W_{ab}(r-r', h) \,, \tag{57}$$

where V_b is the volume of the neighboring particles b. This is called the summation or particle approximation. The kernel function W is usually a Gaussian-like or cubic b-spline function which goes to zero at some κh, where $\kappa = 2$ normally. Gradients can be approximated as:

$$\nabla A_a = \sum_b A_b V_b \nabla W_{ab}(r-r', h) \,. \tag{58}$$

In SPFMaX, the cubic spline function is used because of its simplicity and compact support at a radius of $2h$ away from the test particle. The cubic spline is given by

$$W_{ab} = \begin{cases} \dfrac{1}{4\pi h_{ab^3}}\left[(2-q)^3 - 4(1-q)^3\right], & \text{for } 0 \le q \le 1 \\ \dfrac{1}{4\pi h_{ab^3}}(2-q)^3, & \text{for } 1 \le q \le 2 \\ 0 & \text{for } q > 2 \end{cases} . \tag{59}$$

The key to implementing any SPH method properly is to have an accurate list of neighbors for each particle and a compact support distance h which scales the kernel function and its gradients so the following constraints are satisfied:

$$\sum_b V_b W_{ab} = 1 \tag{60}$$

and

$$\sum_b V_b \nabla W_{ab} = 0 \ , \tag{61}$$

where V is the particle volume, given by

$$V_a = \frac{h_a^3}{\eta^3} \ , \tag{62}$$

and η is a flexible parameter that is fixed at a value of 1.11 in SPFMaX. It scales the ratio of h to the particle's true radius. In practice, it is very difficult to choose a compact support distance for each particle to satisfy the equations above everywhere at every time step.

SPFMaX solves the single fluid equations of motion. Conservation of mass is given by

$$\frac{\partial \rho}{\partial t} + \nabla \cdot (\rho u) = 0 \ , \tag{63}$$

where ρ (kg/m^3) is the mass density, **u** is the velocity vector, and t is time. SPFMaX solves conservation of mass exactly because the continuity equation is not solved. Rather, density is determined by the particle mass divided by the particle volume, where the mass is a constant property of the particles. SPFMaX computes the density from:

$$\rho_a = \frac{m_a}{V_a} \ . \tag{64}$$

The momentum equation for a single fluid is given by

$$\frac{\partial u}{\partial t} = -\frac{1}{\rho}\nabla p + \nabla \cdot \tau + \frac{1}{\rho} j \times B \ , \tag{65}$$

where p is the static pressure and τ is the deviatoric viscous stress tensor. The single temperature energy equation ($T_i = T_e = T$) is given by:

$$\frac{\partial e}{\partial t} = -\frac{p}{\rho}\nabla \cdot u + \frac{\tau}{\rho}\nabla \cdot u - \nabla \cdot (k \nabla T) - 4\sigma T^4 \chi_{\text{Planck}} + \frac{\eta}{\rho} j^2 \ , \tag{66}$$

where k is the thermal conductivity, σ is the Stefan-Boltzmann constant, T is temperature, and χ_{Planck} is the single group Planck emission opacity. Alternatively, if the optical thickness $1/(\rho\chi_{\text{Planck}})$ is of the same order or smaller than the particle scale h, then radiation can be modeled as a diffusion process by adding an additional term to the overall thermal conductivity:

$$k_{\text{total}} = k + k_{\text{Ross}} = k + \frac{4acT_e^3}{3\rho\chi_{\text{Ross}}} \ , \tag{67}$$

where $a = 4\sigma / c$ is the radiation density constant. If the temperature is split between ions and electrons, then the two temperature energy equations are given by:

$$\frac{\partial e_i}{\partial t} = -\frac{p_i}{\rho}\nabla \cdot u + \frac{\tau}{\rho}\nabla \cdot u - \nabla \cdot (k_i \nabla T_i) + Q_{ei} \tag{68}$$

and

$$\frac{\partial e_e}{\partial t} = -\frac{p_e}{\rho}\nabla \cdot u - \nabla \cdot (k_e \nabla T) - 4\sigma T_e^4 \chi_{\text{Planck}} - Q_{ei} + \frac{\eta}{\rho} j^2 \ , \tag{69}$$

where

$$Q_{ei} = \frac{3m_e Z k}{m_i^2} \ \frac{\left(T_e - T_i\right)}{\tau_e} \tag{70}$$

and the electron collision time is:[33]

$$\tau_e = \frac{3}{4\sqrt{2\pi}} \frac{m_i \sqrt{m_e}}{Z\rho} \frac{\left(kT_e\right)^{3/2}}{\lambda} \frac{\left(4\pi\varepsilon_0\right)^2}{q^4} \,. \tag{71}$$

The NIAC-funded gradient field project posed some challenges to the existing gradient field solver, which propagates electric and magnetic fields via the scalar and magnetic vector potentials using second-order time derivatives,

$$\frac{\partial^2 \phi}{\partial t^2} = c^2 \left(\nabla^2 \phi + \frac{\rho_c}{\varepsilon_0} \right) \tag{72}$$

and

$$\frac{\partial^2 \mathbf{A}}{\partial t^2} = c^2 \left(\nabla^2 \mathbf{A} + \mu_0 j \right) , \tag{73}$$

where ϕ is the electric scalar potential, c is the speed of light in a vacuum, ε_0 is the permittivity of free space, **A** is the magnetic vector potential, μ_0 is the permeability of free space, and **j** is the current density vector. The model works well for propagating waves from current and charge density sources, but in steady state, the second-order derivatives have to balance exactly with the source terms, otherwise, the fields can grow rapidly. In steady state, which is a good approximation when the time for an electromagnetic wave to propagate from the source to a point of interest is short with other time scales in the model, the magnetic and vector scalar potentials are:

$$\mathbf{A}(r,t) = \frac{\mu_0}{4\pi} \int_\Omega \frac{\mathbf{j}(r',t')}{|r-r'|} d^3 r' \tag{74}$$

and

$$\phi(r,t) = \frac{\mu_0}{4\pi\varepsilon_0} \int_\Omega \frac{\rho(r',t')}{|r-r'|} d^3 r' \,. \tag{75}$$

The challenge with these equations is that the integrals have to be evaluated over the entire computational domain, so that if each SPH particle had a finite charge or current density, it would be felt by every other particle in the domain, making the method computationally expensive. To overcome this, the source terms are gathered to point sources in a subset of the points to approximate the sources, while avoiding a set of N^2 number of calculations. The electric field is computed from ϕ and **A** with

$$E = -\nabla\phi - \frac{\partial \mathbf{A}}{\partial t} \tag{76}$$

and the magnetic field is calculated with

$$B = \nabla \times \mathbf{A} \,. \tag{77}$$

Evaluating B in this way ensures that $\nabla \cdot \mathrm{B} = 0$ is enforced exactly.

The source terms used to propagate fields are either determined from boundary conditions, such as from an external field coil, or via solution to a system of self-consistent transmission line equations which propagate current and potential changes in the SPH particles. Figure 27 is used to explain how the model works. The green circuit represents an example of an external circuit which drives current, voltage, electric, and magnetic fields inside the computational domain. The computational domain is represented by the red, gray, and black physical SPH particles and the cyan (electric) and yellow (magnetic) field particles, where the electric and magnetic field points are staggered as shown in the figure.

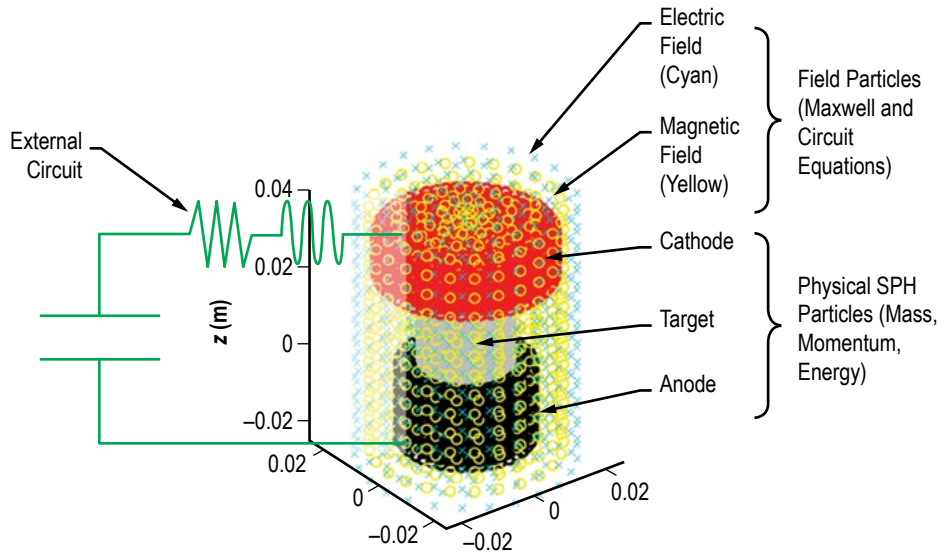

Figure 27. Example of external circuit and connections to anode and cathode of a z-pinch with SPH particles (red, gray, and black) immersed in electric particles (cyan) and magnetic particles (yellow).

For an external circuit, which can be modeled as a series of transmission line sections (including simple RLC circuits, Marx banks, pulse forming networks, and linear transformer drivers), the equations are:

$$\dot{V}_1 = \frac{I_1}{C_1} ,$$

$$\dot{I}_1 = \frac{1}{L_1}\left(V_1 - R_1 I_1 - V_{T,1}\right) ,$$

$$\dot{V}_{T,1} = \frac{I_T}{C_T}\left(\frac{I_1 - I_{T,1}}{\Delta z}\right) ,$$

$$\dot{V}_{T,i} = \frac{I_T}{C_T}\left(\frac{I_{T,i-1} - I_{T,i}}{\Delta z}\right) i = 2 \text{ to } N ,$$

$$\dot{I}_{T,i} = \frac{I_{T,i}}{L_{T,i}}\left(\frac{V_{T,i} - V_{T,i+1}}{\Delta z}\right) - \frac{I_{T,i} R_{T,i}}{L_{T,i}} i = 1 \text{ to } N-1 ,$$

$$\dot{I}_{T,N} = \frac{1}{L_{\text{SPH}}}\left(\phi_{\text{SPH, pos}} - \phi_{\text{SPH, neg}}\right) - \frac{I_{T,N} R_{T,N}}{L_{T,N}} , \tag{78}$$

where the subscript T refers to a transmission line section. Note that the nodes N of the transmission line could be capacitors with their own initial charging voltage or could be bus bars or other passive elements transferring the current and voltage from the capacitor bank to the SPH particles. The last equation, for the time rate of change of current, is directly connected to the SPH particles through the potential difference between the positive and negative SPH particles where the circuit is connected, and the potential is taken to be the mean value for each of the positive and negative electrode leads.

For all SPH particles, the transmission line equations for the physical SPH particles are given as:

$$\left(\frac{\partial \phi}{\partial t}\right)_a = -\left(\frac{I}{C'}\right)_a , \tag{79}$$

where **n** is a unit normal for each face of the particle and C' is the capacitive gradient per particle. The current I in each particle is advanced in the x, y, and z directions with

$$\frac{\partial I_n}{\partial t} = \frac{-\frac{\partial \phi_n}{\partial n} - (v \times B)_n + \frac{\partial R}{\partial n} I_n}{\frac{\partial L_n}{\partial n}}, \; n = x, y, z \; , \tag{80}$$

where

$$R_n = \frac{\rho l}{\mathbf{A}_n} \; . \tag{81}$$

Current density in each particle is given by:

$$\mathbf{j}_n = \frac{I_n}{\mathbf{A}_n} \tag{82}$$

and charge density by:

$$\frac{\partial \rho}{\partial t} = \frac{1}{\text{vol}} I \cdot n \, , \tag{83}$$

where the I_n term is the net current into the particle. In order to connect the external circuit to the SPH particles, the current from the external circuit is added to the positive and negative SPH particles where the circuit is connected. This will add potential to those boundary particles at a rate of I/C. Also, these boundary particles are set with a total current rise rate equal to $\dot{I}_{T,N}$ from the external circuit transmission line equations above.

5.1 SPFMaX Preliminary Results

A preliminary model has been developed for target injection into a converging/diverging magnetic field coil. Figure 28 displays the notional converging/diverging nozzle geometry, showing (a) the coil windings and (b) the magnetic streamlines.

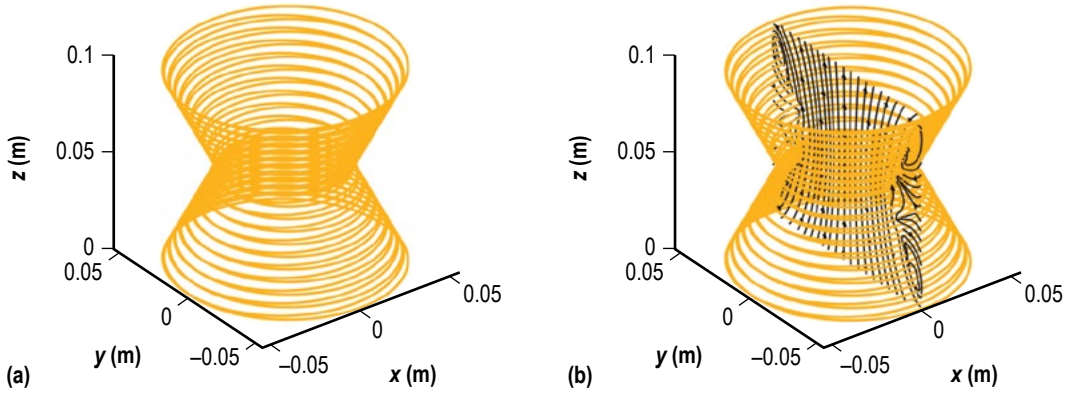

Figure 28. Magnetic field coil: (a) With converging/diverging windings and (b) with magnetic field streamlines.

A simulated fuel target was launched at 2 km/s into the entrance of the coil, with the sequential evolution of target density displayed in figure 29. Although not shown in the figure, an azimuthal current was induced on the surface of the pellet caused by the gradient field, further validating the physics of the gradient field imploding liner concept. Plans to further verify the magnetic flux compression algorithms using a known test case are discussed in section 5.2.

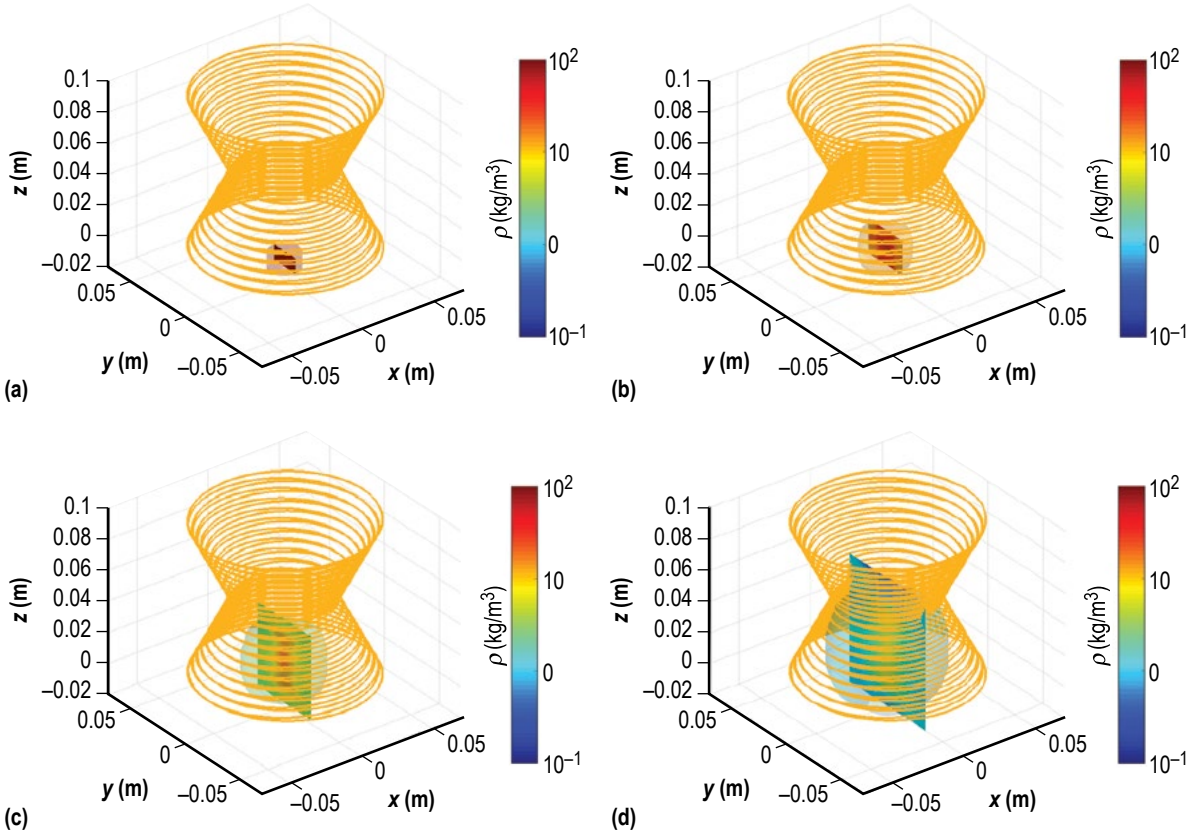

Figure 29. Sequence of target propagation through the entrance of a magnetic field coil: (a) 0 ns, (b) 500 ns, (c) 1,000 ns, and (d) 1,500 ns.

Figure 30 shows a plot of the 3D target entering the mouth of the coil. It is difficult to see against the other details in the plot, but the current is induced on the surface of the pellet as a result of the $v_z \partial B_z / \partial z$ term. Qualitatively, this provides independent validation of the concept, but additional verification remains to be performed using the test case described below.

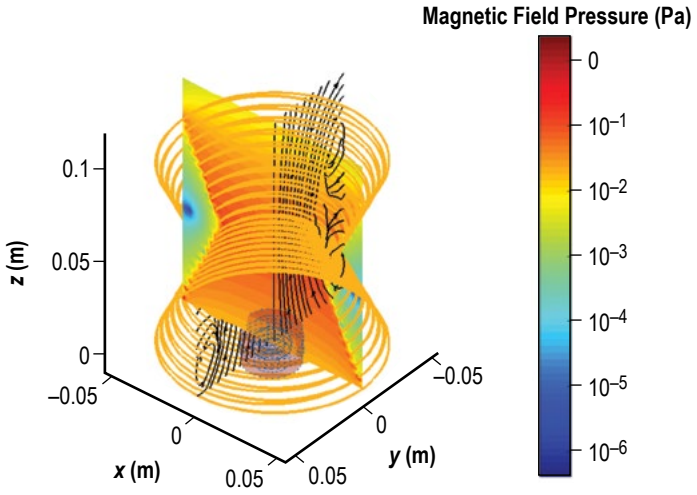

Figure 30. Preliminary simulation of the gradient field propulsion system.

5.2 Verification Test Case Plan

Among the more relevant subjects in which the physics overlap with the gradient field fusion concept is magnetic flux compression. Typically, magnetic flux compression generators are devices that convert part of the energy contained in high explosives into electromagnetic energy (fig. 31). These have application where weight and volume are limited. In general, explosives are used to compress an initial magnetic flux by driving a conductive surface that contains the flux. These conductors work on the magnetic field by moving against them, resulting in an increase in the electromagnetic energy. This energy comes from the explosives and is transmitted to the conductors.

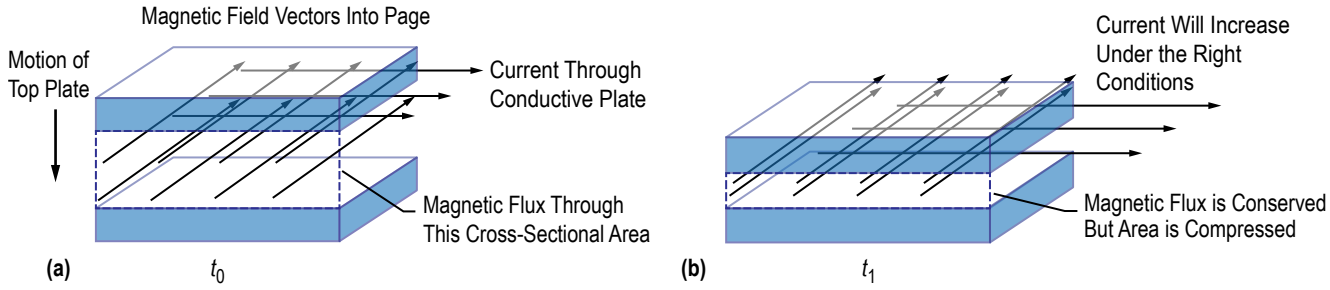

Figure 31. Flux compression generator illustration: (a) A conductive plate with a seed current and seed field traps flux between itself and a bottom conductive plate. Explosives or other force push the plate down with a negative vertical velocity and (b) the top plate and compressed area between the plates. The flux is conserved, and the current rises under conditions discussed in the text.

The modeling of such devices is documented in Fowler and Altgilbers.[34] Conservation of flux gives

$$\phi = B_0 \lambda x_0 = \phi(x) = B \lambda x \,, \tag{84}$$

where λ is the plate width and x_0 is the initial plate spacing. The magnetic pressure is

$$P_M = \frac{B^2}{2\mu_0} \,. \tag{85}$$

The initial magnetic energy is obtained by multiplying this by the volume:

$$E_0 = \frac{B_0^2}{2\mu_0} \lambda \omega x_0 \,, \tag{86}$$

where ω is the plate depth into the page. As the conducting plate moves downward, the energy is

$$E(x) = \frac{B^2}{2\mu_0} \lambda \omega x \,. \tag{87}$$

Using the expression for the magnetic flux,

$$E(x) = \frac{\left(B_0 x_0 / x\right)^2}{2\mu_0} \lambda \omega x = \frac{\left(B_0\right)^2}{2\mu_0} \lambda \omega x_0 \frac{x_0}{x} = E_0 \frac{x_0}{x} \,. \tag{88}$$

It is desirable to relate the magnetic field to the current. For the plate geometry, this is

$$B = \mu_0 \frac{1}{\omega} \,. \tag{89}$$

The generator inductance is then

$$L(x) = \mu_0 \lambda \frac{x}{\omega} \,. \tag{90}$$

Thus, the flux becomes

$$\phi = L_0 I_0 \,. \tag{91}$$

As the conductor moves, the flux is

$$\phi(x) = L(x) I \,. \tag{92}$$

The energy is

$$E_0 = \frac{1}{2} L_0 I_0^2 \ . \tag{93}$$

As the conductor moves, the energy varies as

$$E(x) = \frac{1}{2} L(x) I^2 = E_0 \frac{L_0}{L(x)} \ . \tag{94}$$

More generally, for perfectly conducting systems, one can write

$$\frac{d\phi}{dt} = \frac{BA}{dt} = \frac{d(LI)}{dt} = 0 \ . \tag{95}$$

This is also a statement that the voltage around the circuit is zero; expanding, gives

$$I \frac{dL}{dt} + L \frac{dI}{dt} = B\lambda v + L \frac{dI}{dt} = 0 \ . \tag{96}$$

The circuit in a flux compression generator (FCG) hooked to an external load (denoted by L_1) can be illustrated in figure 32, where the FCG is represented as the time-dependent inductance.

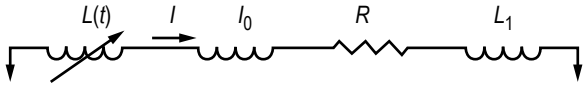

Figure 32. Circuit in an FCG.

The equation governing the performance of this circuit is

$$\frac{d}{dt}\left[\left(L + L_p + L_1\right) I\right] + IR = 0 \ , \tag{97}$$

where the parasitic transmission line inductance is L_p. The equation expands as

$$\left[\frac{dL}{dt} + R\right] I + \left(L + L_1 + L_p\right) \frac{dI}{dt} = 0 \ . \tag{98}$$

Using this model to guide a future verification run in SPFMaX, a MATLAB-based graphical user interface (GUI) was developed to expedite the parametric analysis of a case in which current is amplified in a parameter space comparable to the gradient field fusion concept. Figure 33 displays results for a compressive plate velocity of 12 km/s, resulting in an initial seed current of 1 MA, rising up to 16 MA in 20 μs.

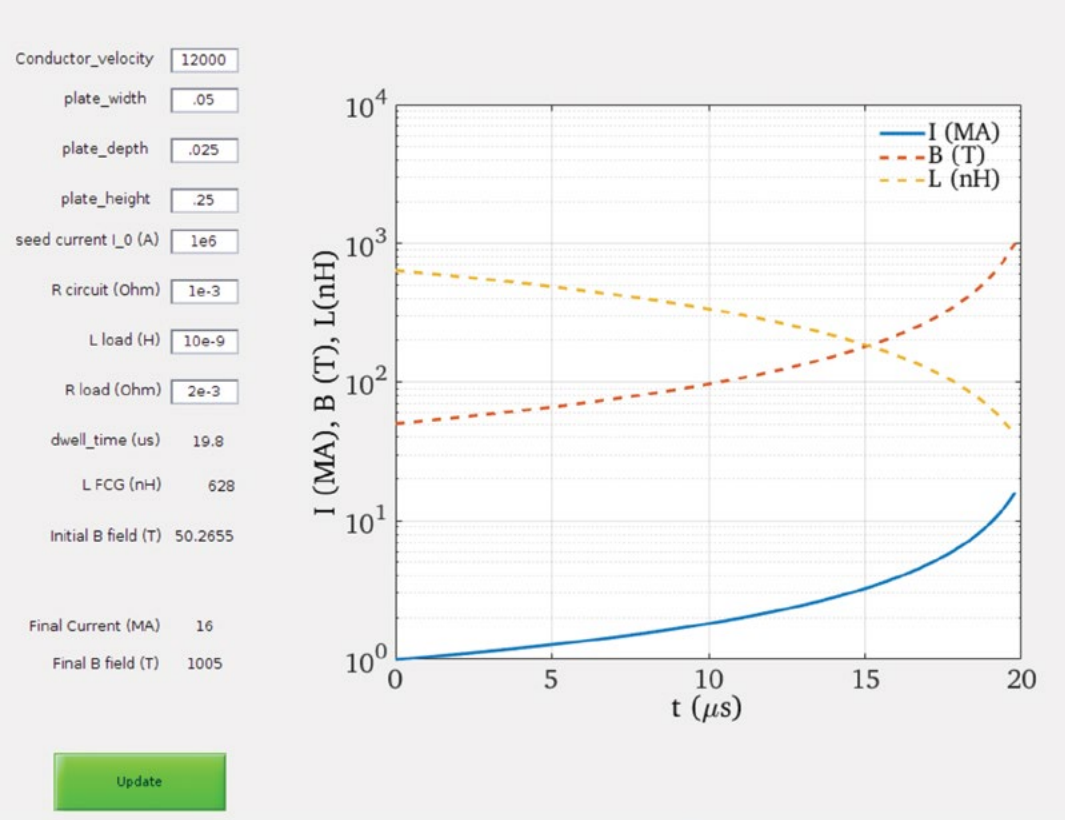

Figure 33. Screen capture of the MATLAB-based GUI flux compression generator model developed for this project.

While additional modifications to the SPFMaX code remain to be incorporated, significant progress has been made toward modeling rapid magnetic flux compression and simulating the induced currents generated by a high velocity target traversing a magnetic field gradient, lending a degree of confidence in the proposed concept and the underlying simulations. Future work will incorporate these advancements into a simulation of the gradient field imploding liner geometry to evaluate the accuracy of the analytic results presented earlier and to provide a deeper understanding of the physics underlying the concept.

6. MISSION ANALYSIS

In order to identify operating regimes with the greatest impact on space exploration missions, a parametric assessment of mission outcomes has been performed. To span both near- and far-term mission goals, one-way missions to Mars and Saturn have been examined. In order to capture a range of applications from piloted to cargo, the missions spanned trip times from 20 days to 1 year, and with payloads from 20 mt (representing a crew vehicle for a fast transport) to 200 mt (representing a cargo mission in support of extended presence at the destination). While fusion offers the potential for much higher power and thrust levels than conventional electric propulsion, it is not quite in the range where simple impulsive ΔVs might be assumed. For demanding, fast planetary missions, the system must still thrust over a significant portion of the trajectory, which then introduces gravity and steering losses that must be accounted for based on system performance. In order to capture a possible range of operating scenarios, from nearly impulsive burns to extended operation similar to that of an electric propulsion vehicle, an analytic approximation method was used that captures this full range of operation.

The mission analysis is based on the equivalent length method developed by Zola,[35] in which an equivalent length, derived from detailed trajectories over a range of acceleration levels, was found to be essentially invariant to the magnitude of the vehicle acceleration. Using this length, together with an assumption of travel in field free space, allows simplified rectilinear analysis of missions. This approach provides for rapid estimation of mission performance over a wide range of propulsion systems and mission times and has been used previously to examine nuclear electric propulsion performance for Mars missions.[36] Equivalent length values for one-way rendezvous missions to Mars and Saturn were used to scope vehicle performance for the current concept.

The overall propulsion performance of the system can be defined parametrically in terms of the specific power of the propulsion system, α (kW/kg), the jet power, $P_{\text{jet}} = F^2/2\dot{m}$, and specific impulse, $I_{\text{sp}} = F/\dot{m}g_0$, where F is the thrust, $\dot{m}$ is the propellant mass flow rate, and g_0 is the acceleration of gravity at sea level.

Because calculations of the actual performance were concurrently being developed during the Phase I activity, the system was initially modeled parametrically with values based on the PUFF fusion system,[37] specifically using $P_{\text{jet}} = 1$ GW, $\alpha = 16$ kW/kg, and varying I_{sp} from 10,000 to 50,000 s. Using the equivalent length method described above, a calculation of initial mass and trip time could be performed for varying payloads, initial masses, and I_{sp}. In this way, the regimes in which the engine has the greatest impact can be identified and used to focus design efforts.

The results of these estimates are shown in figure 34 (Mars) and figure 35 (Saturn). Three-dimensional contours of delivered payload mass are shown for 20, 50, 100, 150, and 200 mt of payload, as functions of I_{sp}, initial mass (M_0), and trip time. The overall capability and limits of the system for both missions is evident from the limits of the contours. For Mars, the initial mass is fairly insensitive to trip time of I_{sp} for trip times longer than 100 days, and approximately linear with payload mass. For shorter trip times, a minimum trip time of 40 days is possible for rapidly increasing propellant mass. Fast trips can be accomplished for initial masses of 200–500 mt, and at values of I_{sp} below 20,000 s.

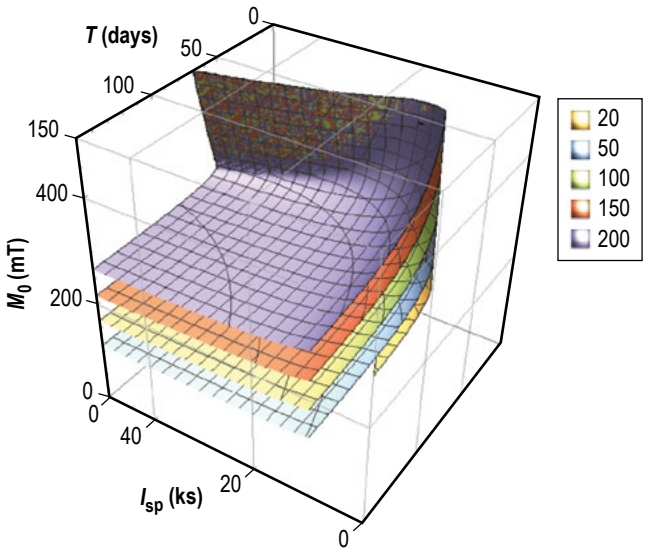

Figure 34. Mission performance contours for one-way trip to Mars.

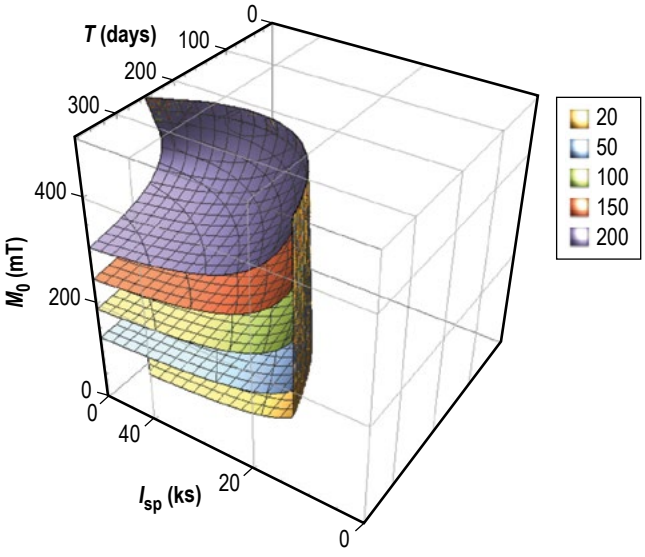

Figure 35. Mission performance contours for one-way trip to Saturn.

The Saturn mission is more constrained, as would be expected for the greater distance. The minimum trip time is on the order of 200 days one way—a relatively short time compared to current propulsion options, but still representing significant exposure to space. A minimum I_{sp} of 20,000 s is required to reach Saturn; at the lower payload mases, there is a lower sensitivity to higher I_{sp}, as seen in the Mars case.

Summarizing the general benefits of the system, the preceding mission analysis indicates that the projected system performance can achieve impressively short trip times for both Mars and Saturn:

- Mars: 100–150 mt payload from low Earth orbit (LEO) using two Space Launch System (SLS) block 2 launches (260 mt),[38] <60–90 days one-way-trip time.

- Saturn: 50–100 mt payload from LEO using two SLS block 2 launches, 200 days one-way-trip time.

6.1 Detailed Mission Examples

To provide more detailed performance estimates, the 'optimized' performance values developed with the simplified semi-analytic model (secs. 3 and 4) were used. As noted in table 5, these correspond to the two thrust and I_{sp} levels for the Be and Li liners but assumes comparable power levels. It is also assumed that the engine operates at a 10-Hz repetition rate, consistent with the assumptions in section 4, to provide the average thrust values used in the table. These options were examined parametrically for a Mars outbound case over a range of trip times to give an estimate of their capability both for fast delivery for crewed missions and for high payload delivery. A crewed mission is assigned to primarily carry crew as the payload, with an estimated payload mass of 50 mt. The high payload mission assumes significant infrastructure will be delivered to the Martian surface.

Table 5. Calculated performance space for gradient field fusion system.

	Li Liner	Be Liner
Specific impulse (s)	32,200	17,145
Impulse (N-s)	780	1,445
Thrust (N)	7,800	14,450
Yield (J)	1.65×10^8	1.53×10^8
Gain (100% efficiency)	982	323

To address this range of missions, payloads of 50, 100, and 200 mt to Mars were considered, and propellant mass and total initial mass were calculated for the mission. These results are shown in figures 36 and 37. The fastest trip times are constrained by the all-propulsive limit, in which the vehicle is constantly accelerating for the entire trip. Note that the overall propellant mass rapidly diminishes with trip time, to the point that vehicle mass becomes essentially linear with payload mass as the propellant mass asymptotically decreases to values less than either the payload or propulsion system. The Be liner case, with lower I_{sp}, is capable of somewhat shorter trip times, although not dramatically shorter, at the cost of essentially twice the propellant mass.

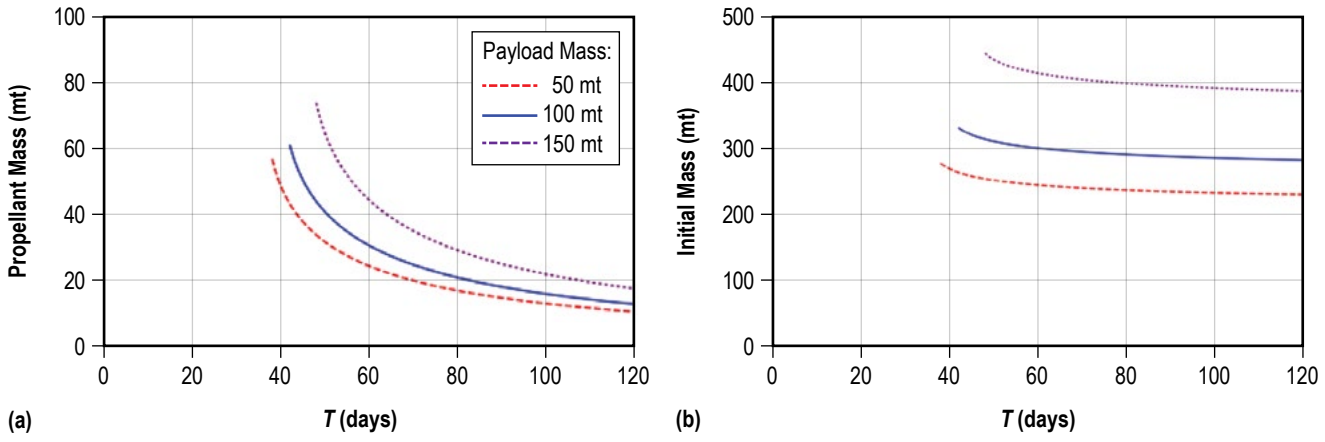

Figure 36. Mars (a) propellant mass and (b) total initial mass scaling for the Li liner gradient field fusion case.

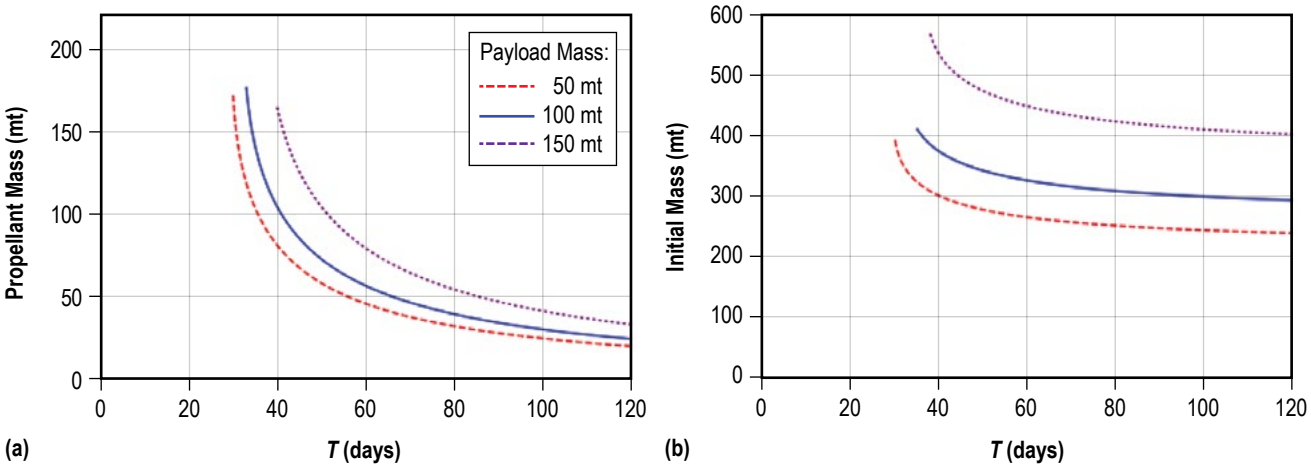

Figure 37. Mars (a) propellant mass and (b) total initial mass scaling for the Be liner gradient field fusion case.

Because of the high performance of the Gradient Fusion system and its relative insensitivity to Mars mission times, a Saturn mission was also considered for the same system design parameters, as shown in figures 38 and 39. For one-way-trip times under a year, there is a greater sensitivity of propellant mass due to the higher energy requirements. There is also a significant benefit in using the Li liner system with its higher I_{sp}. Propellant masses are substantially reduced, while accessible trip times are essentially the same. For a long-term exploration program of the solar system, the Li liner system appears to offer the widest benefits, due to the high I_{sp} and high power density of the fusion system.

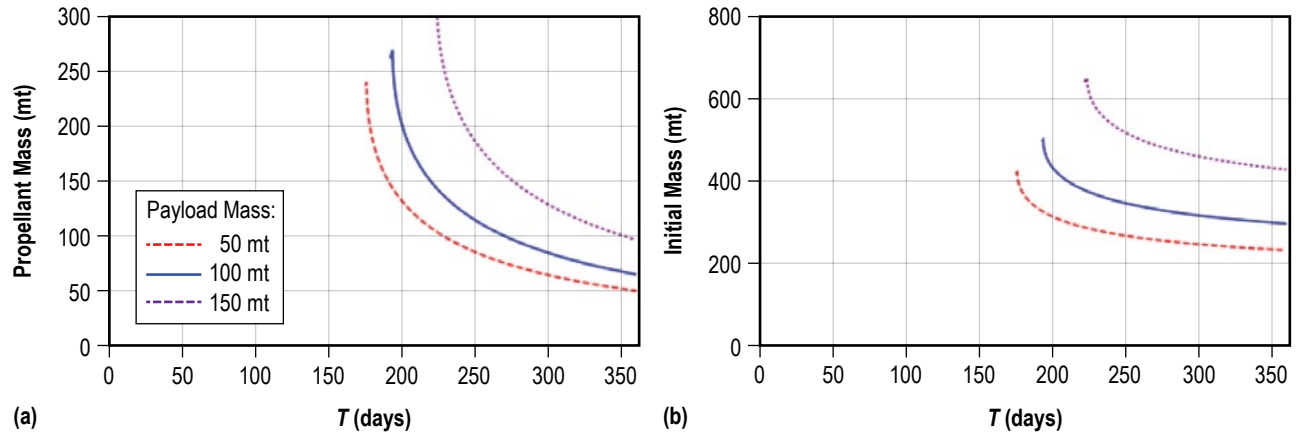

Figure 38. Saturn (a) propellant mass and (b) total initial mass scaling for the Li liner gradient field fusion case.

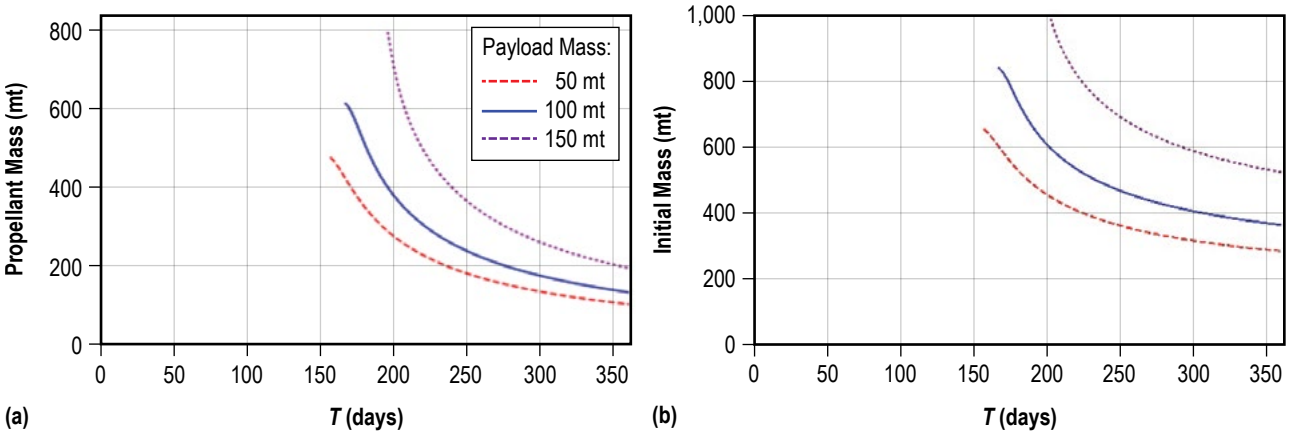

Figure 39. Saturn (a) propellant mass and (b) total initial mass scaling for the Be liner gradient field fusion case.

The calculations to date have been for one-way trips; however, especially in the case of the Mars mission, propellant mass plays a relatively small role in the overall system mass over a range of trip times, from 20 mt (Li liner) to 50 mt (Be liner). A symmetric Mars round trip for a 50-mt crew mission payload could be considered as an outbound payload of 100 mt, with 50 mt used for the return trip. For an assumed vehicle mass of 320 mt, a 100 mt payload using 50 mt of propellant would require 45 days with the Li-lined target system, and on the order of 75 days with the Be-lined target system. For a lower vehicle mass of 270 mt, a 50 mt payload can be delivered in 40 days (one way) with 50 mt of propellant. Additional analysis with more detailed trajectory codes can be used to more accurately calculate potential round-trip times, but assuming the validity of the semi-analytic model performance predictions, the engine appears capable of providing rapid transit for both crew and cargo to solar system destinations of current interest for human exploration.

7. VEHICLE DESIGN

A preliminary vehicle design was evaluated as part of the Phase I activity. As with most nuclear systems, the vehicle design is dominated by the need to radiate waste heat, here mainly impinging on the struts and supports of the magnetic nozzle and main vehicle supports. Figure 40 provides an overview of the initial vehicle concept. The numbers shown in the figure reflect a fast trip to Mars carrying an Orion module and deep space habitat. The vehicle design leverages the prior analytical work found in references 39 and 40. Based on the mission analysis provided in section 6, the vehicle assumes a payload mass of 50 mt and a (one-way) propellant mass of 50 mt. Table 6 in the following section provides the mass breakdown by subsystem, sized using the performance values from the previously mentioned references. Future work will include more detailed analysis of each individual subsystem.

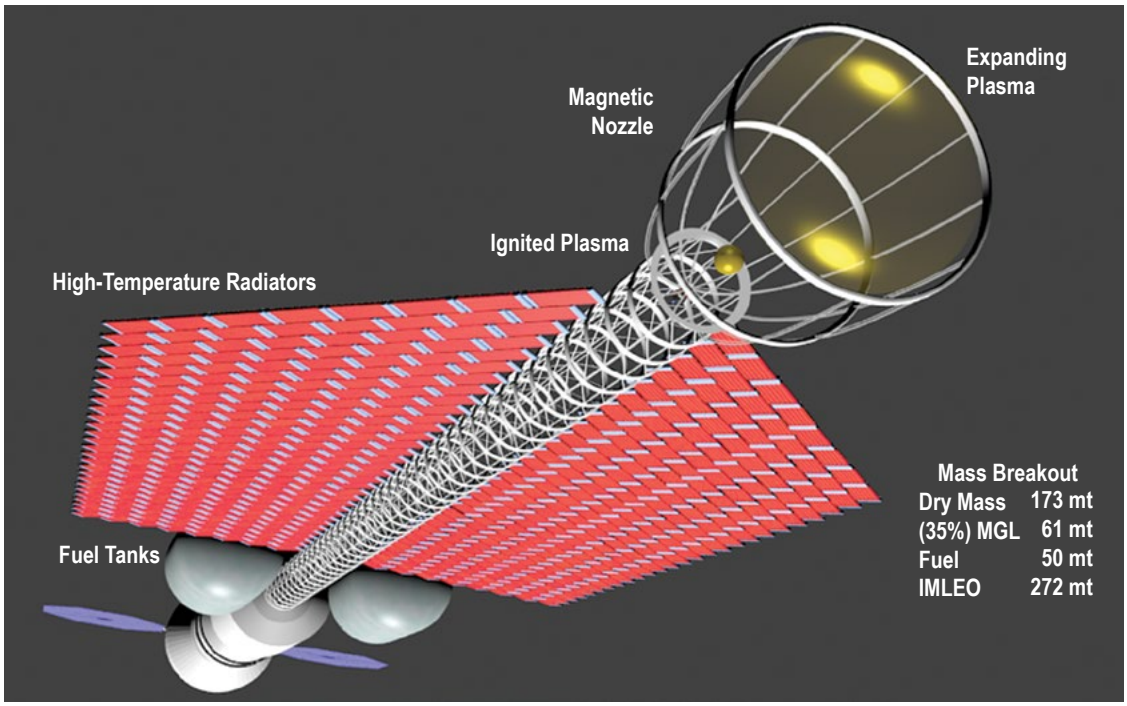

Figure 40. Illustrative vehicle concept.

Table 6. Preliminary vehicle design parameters.

System	Mass (mt)
Prop tanks	5
Thermal	13.6
Propulsion	75.4
Structural	17.3
Avionics	3.5
Mass growth allowance	58.4
Inert mass	173.2
Payload	50
Dry mass	223.2
Ullage	1.5
Inert mass	224.7
Propellant	48.5
IMLEO	271.6

7.1 Vehicle Assumptions

The propellant tanks are sized assuming a 10% mass relative to the amount of propellant stored. This is a fair approximation given the size of the tanks and the bulkiness of hydrogen. A reference point is the Shuttle external tanks, where the dry mass of the tanks is 7% of the fully-loaded mass.

Thermal subsystems can be complex to design because the size of the radiators are a strong function of the system efficiency. A rejection temperature of 1,250 K is assumed in this analysis. The following steps are used to estimate the thermal load to be rejected. The jet power may be calculated as:

$$P_{\text{jet}} = \frac{1}{2}\dot{m}v_e^2 \ , \tag{99}$$

where $\dot{m}$ is the mass flow rate of propellant and v_e is the exhaust velocity. The thrust, F, is given by:

$$F = \dot{m}v_e + A_e\left(p_e - p_a\right) , \tag{100}$$

where the second term is the exit area times the difference in exit pressure and atmospheric pressure. This term approaches zero for a well-designed nozzle. Substituting equation (100) into equation (99), and noting that the I_{sp} may be written as $I_{\text{sp}} = F/\dot{m}g_0$, yields the following expression for jet power:

$$P_{\text{jet}} = \frac{1}{2}Fg_0 I_{\text{sp}} \ . \tag{101}$$

For the parameters identified in section 6 (assuming 100% efficiency), the jet power is calculated to be approximately 1.2 GW. Thermal loads are primarily due to radiative heating of the superconducting magnet coils during target compression and fusion initiation, and radiation from the hot expanding plasma impinging on the struts that comprise the magnetic nozzle. The thermal load

on the coils is expected to be relatively low, due to the short timeframe of the pulsed fusion event, the rapid movement of the target through the coils into the nozzle, and the initial neutron reflector/moderator properties of the target liner. The plasma expanding into the magnetic nozzle region has a longer duration in which to impart thermal loads to the struts, hence the nozzle must be designed with as much open surface area as possible to allow the majority of photons and neutrons to escape, while still directing the charged plasma particles for thrust.

To calculate the thermal load, it is assumed that some fraction (φ_{therm}) of the generated fusion power (P_{gen}) goes immediately into thermal losses to the coils and structure. Of the remaining power, some fraction (φ_{loss}) is assumed to escape to space. The total power left in the directed plasma jet is then:

$$P_{\text{jet}} = P_{\text{gen}} - P_{\text{gen}}\varphi_{\text{therm}} - P_{\text{gen}}\left(1-\varphi_{\text{therm}}\right)\varphi_{\text{loss}} \ . \tag{102}$$

For the initial calculations, a 10% thermal loss is assumed ($\varphi_{\text{therm}} = 0.1$), with an additional 10% of the remaining energy lost to space ($\varphi_{\text{loss}} = 0.1$). Equation (102) then predicts $P_{\text{jet}} = 0.81 \cdot P_{\text{gen}}$, or a loss of approximately 19%. Assuming an initial power generation of 1.2 GW, the power loss is approximately 0.2 GW. These estimates are not unreasonable, given the open structure of the magnetic nozzle which provides a significant viewing area to the expanding plasma.

Using the standard equation for radiative heat transfer:

$$q = \varepsilon\sigma A T^4 , \tag{103}$$

where ε is the infrared emissivity (optimistically set to unity), σ is the Stefan-Boltzman constant, and T is the rejection temperature (1,250 K) yields a required viewing area, A, of approximately 1,360 m^2. The radiator mass can then be estimated assuming a double-sided radiator with an areal density of 5 kg/m^2, as designed in reference 39, and a ratio of radiator mass to pump/cryo mass of unity, also from reference 39, to provide an estimated thermal mass of around 13.6 mt.

The propulsion system is sized using an alpha of 17.6 kW/kg, which is the specific power used in the magnetized target fusion (MTF) concept in reference 38. This value is somewhat pessimistic, as the current system will be significantly less complex and presumably less massive than the referenced MTF system.

The structural mass fraction is assumed to be 10%, calculated as a fraction of the total inert mass, which is a commonly used standard for in-space, medium thrust vehicles. Similarly, the avionics mass is assumed to be 2%.

Mass growth allowance is strongly debated in any new concept. Here, a mass growth allowance of 50% is assumed as an initial value, given the early stage of the propulsion and vehicle concept.

8. OPTIONS FOR A GROUND-BASED, PROOF-OF-CONCEPT DEMONSTRATION

Toward the end of the Phase I activity, consideration was given toward a future ground-based experimental program to anchor the analytic and computational models for magnetic flux and target compression. Although the specific accelerator and superconducting magnet systems outlined in this Phase I TP are likely beyond the scope of NIAC funding, suitable low-cost hardware can be used to perform proof-of-concept tests to demonstrate the dynamics of radial compression arising from high-velocity target injection into a suitably strong magnetic field. In place of the repetitively pulsed high-power laser proposed for target ablation and acceleration, a ground-based light gas gun (LGG) can be used to generate high initial axial target velocities. Pulsed or steady state water-cooled coils can be used to generate a range of axial magnetic field strengths and gradients. Replacing the Li- or Be-lined D-T fusion target with more mundane but readily manufactured hollow or filled spheres and cylinders can provide data for comparison with target compression simulations. Bringing these available systems together into a ground-based test facility for parametric testing and model validation would fall within the scope and budgetary resources of a future NIAC Phase II project, and if successful, could lead to a more detailed experimental program. The following sections provide initial thoughts on a potential approach toward a ground-based, proof-of-concept demonstration.

8.1 Two-Stage Light Gas Gun

A two-stage LGG is a method of compressing and heating a working fluid (He or hydrogen gas) to very high temperatures and pressures for the purpose of accelerating a projectile to very high velocities, greater than 7 km/s. The general concept is to replace the combustible byproducts of a single-stage propellant gun with a lower molecular weight gas, such as He or hydrogen, resulting in a higher sound speed and ultimately higher velocity potential than the heavier gases from traditional systems. This is achieved by separating the gun system in to two major components, the pump tube section and the launch tube, where in effect, the pump tube assembly is replacing a traditional propellant chamber (fig. 41). Because an energy source is still required to function as a gun system, the first step is to burn a propellant in a pressure chamber (fig. 42, step 1). The products from this combustion drive a heavy piston down a pump tube to compress the driver gas to high pressures and temperatures. A high-pressure section transitions the pump tube to the launch tube, and in this section, a projectile is located and separated initially from the driver gas using a burst diaphragm (fig. 42, step 2). Once a sufficiently high pressure is reached, the diaphragm ruptures and the compressed and heated driver gas accelerates the projectile down the launch tube. The piston comes to a stop in a tapered transition section (fig. 42, step 3).

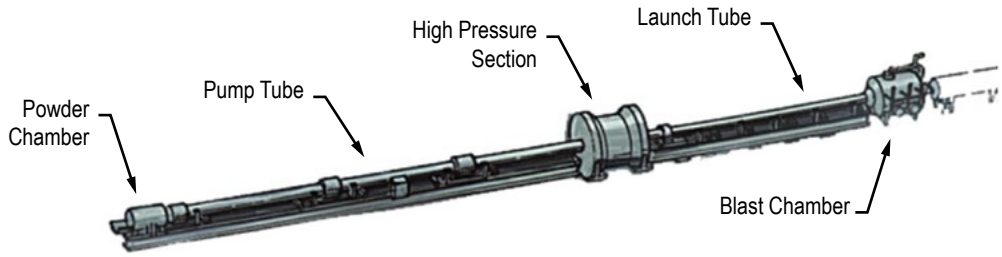

Figure 41. Major components of a two-stage LGG.

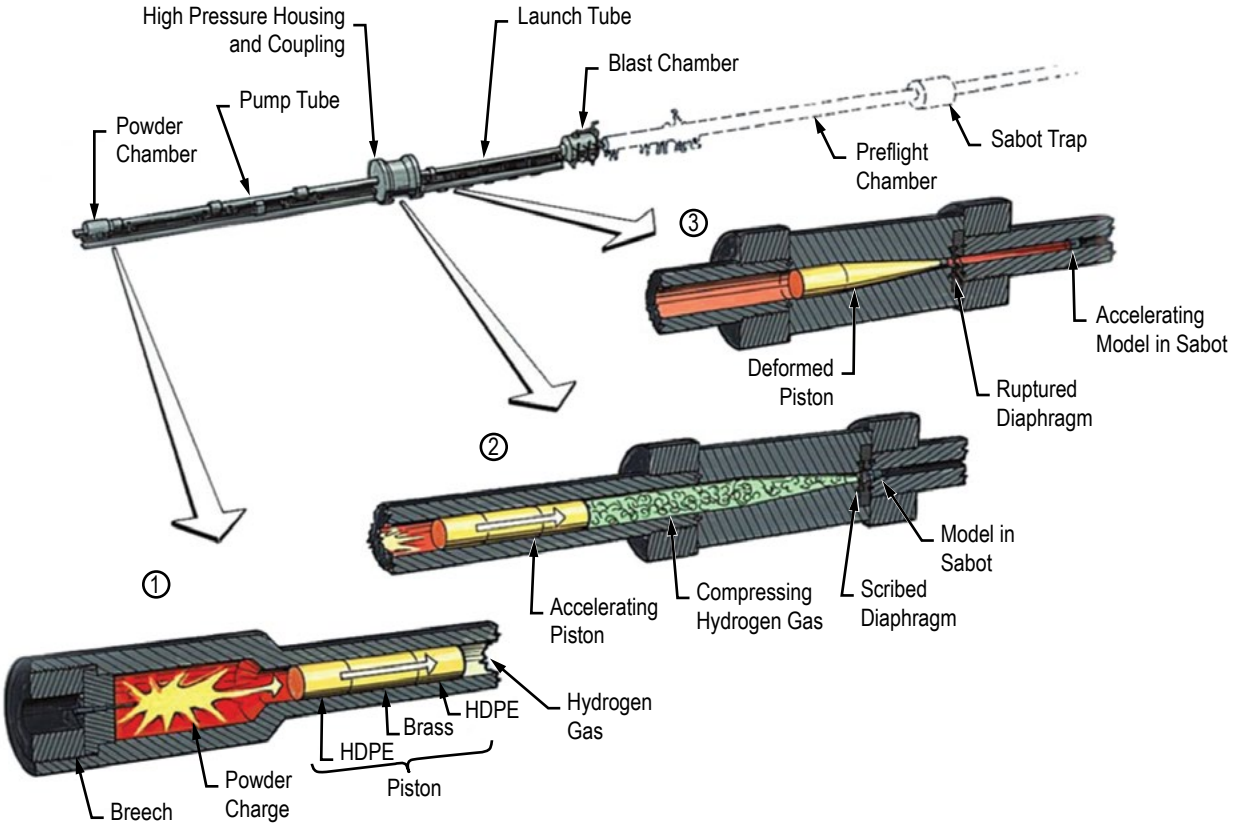

Figure 42. Steps in LGG firing sequence.

8.2 Test Facility Description

UAH operates the Aerophysics Research Center (ARC) located on the Redstone Arsenal in Huntsville, AL. The ARC houses three separate two-stage LGG systems with associated test chambers and instrumentation that are used to conduct experiments in the sub, super, and hypersonic velocity regimes both for high-speed flight and impact testing. The ARC also maintains several custom single-stage launcher systems that can be utilized or modified to meet specific user requirements.

Key parameters of the two-stage LGGs available for this research are defined in table 7. A parametric map of projectile velocity versus projectile mass is shown in figure 43.

Table 7. UAH ARC two-stage LGG parameters with single-stage example.

UAH ARC Launcher Systems	Pump Tube Length (m)	Pump Tube Inside Diameter (mm)	Launch Tube Length (m)	Available Launch Tube Inside Diameters (mm)	Primary Impact Chamber Diameter x Length (m)	Projectile Launch Mass Range (gm)	Projectile Velocity Range (km/s)
Large	38.13	254	22.88	56, 57, 68, 70, 75, 78, 86, 100, 152	3×12.5	150 to 12,000	1 to 7.5
Intermediate	18.3	133	15.25	18, 29, 35	2.4×6.7	40 to 250	1 to 7.5
Small	13.42	108	7.47	19, 29	1.8×4.3	10 to 130	1 to 7.5
Single Stage	NA	NA	9.9	32	2.4×6.7	5 to 100	0.1 to 1.1

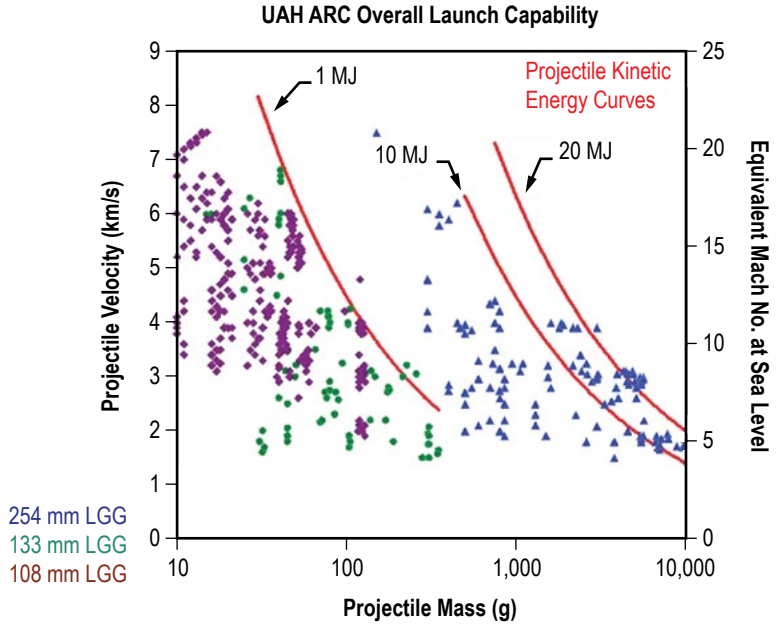

Figure 43. General facility launch mass/velocity capability.

The intermediate two-stage LGG with approximately 30 m (100 ft) of flight range chambers and optional camera/data ports appears suitable for a ground-based, proof-of-concept demonstration. Additional photographs of the intermediate LGG facility are provided in figures 44 and 45.

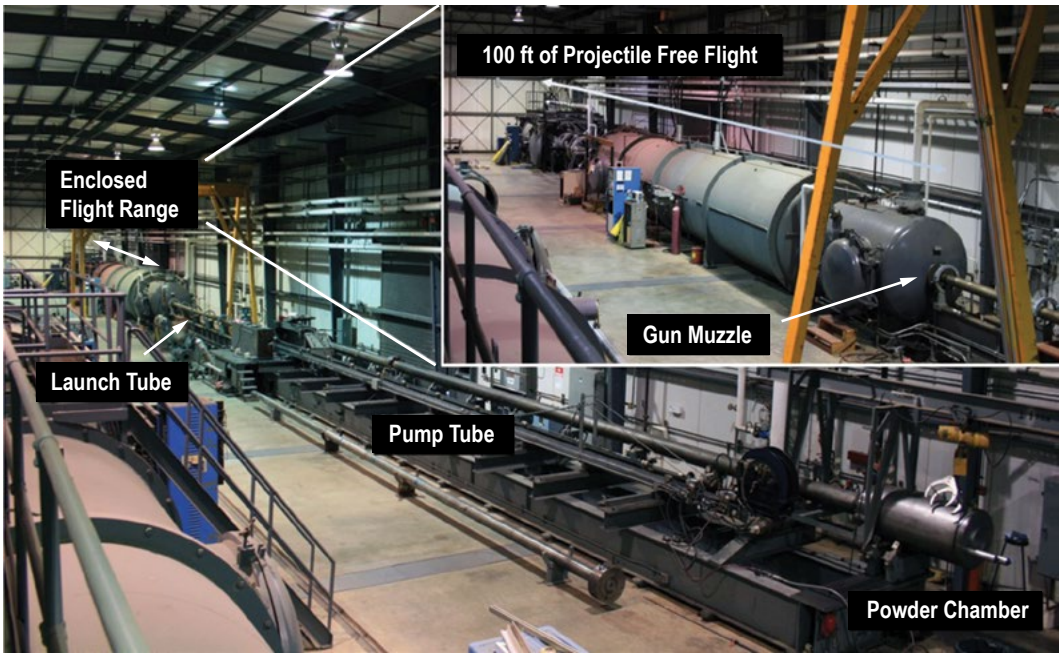

Figure 44. Intermediate-sized, two-stage LGG range.

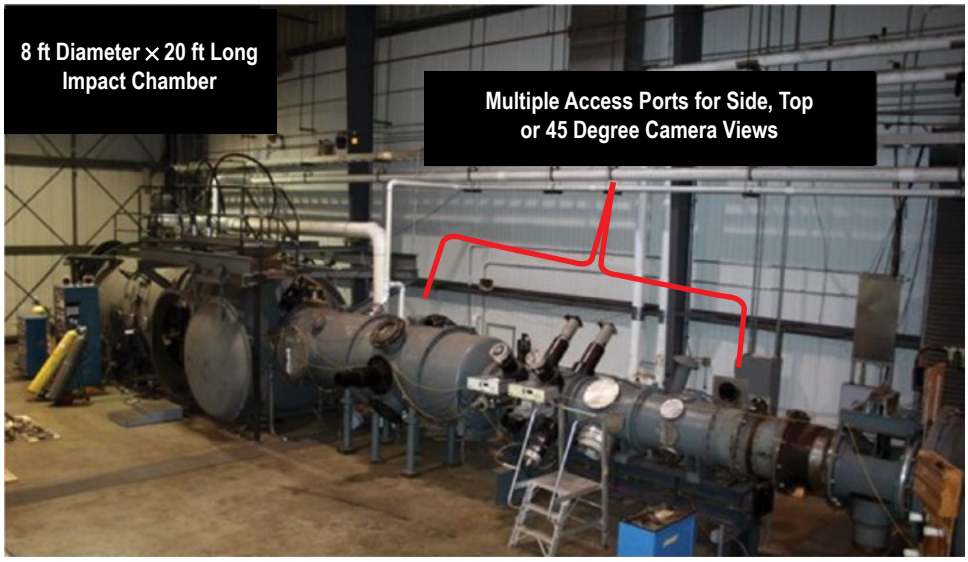

Figure 45. Multiple data acquisition and image access ports for flexible test setup.

8.3 Target Projectiles

Figures 46 and 47 illustrate previously tested projectiles on the intermediate LGG with flight velocities on the order of 5 km/s. For the purposes of studying flux compression, the projectiles could be spherical, cylindrical, or conical, and either solid, filled, or hollow in construction. Various liner materials and shell thicknesses can be used to provide a parametric comparison against numerical simulation compression results. Note that all figures are open source.

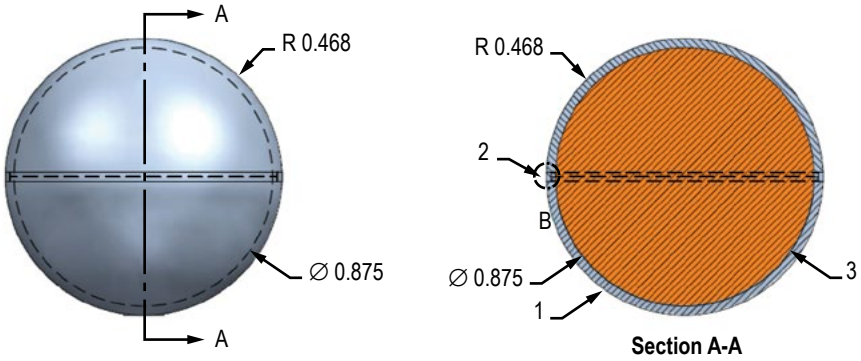

Figure 46. Hollow steel sphere with filler material.

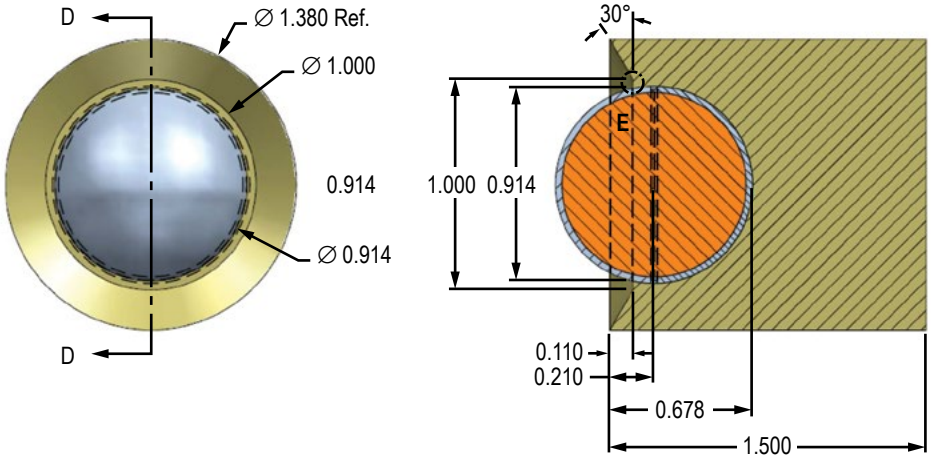

Figure 47. Hollow steel sphere and sabot used for support during launch.

8.4 Potential Test Setup

An illustration of a potential test setup for measuring magnetic flux compression of a hypervelocity projectile is shown in figure 48. In this example, a 2-ft- (0.6-m-) diameter test chamber is fitted with single or multiple water-cooled hollow copper coils to generate a static magnetic field using a high DC source; alternatively, a pulsed current coil with a capacitive power bank could be used and timed to provide a maximum quasi-steady (millisecond time scale) magnetic field just prior to and during the rapid traverse of the injected target. An instrument feedthrough is provided for the installation of *B*-dot probes to measure the dynamic change in the magnetic flux from the projectile. Additional instrumentation could include high-speed cameras suitable for time-of-flight tracking and centerline radial compression videography, wireless pressure sensors to provide compression measurements within the target, external measurement options such as flash x-ray imaging during compression, and multiple data acquisition and control systems that can be readily modified for use. Although just a cursory look at instrumentation options was performed toward the close of the Phase I activity, it appears that several readily available sensors are available and could be included as part of a future experimental proof-of-concept effort.

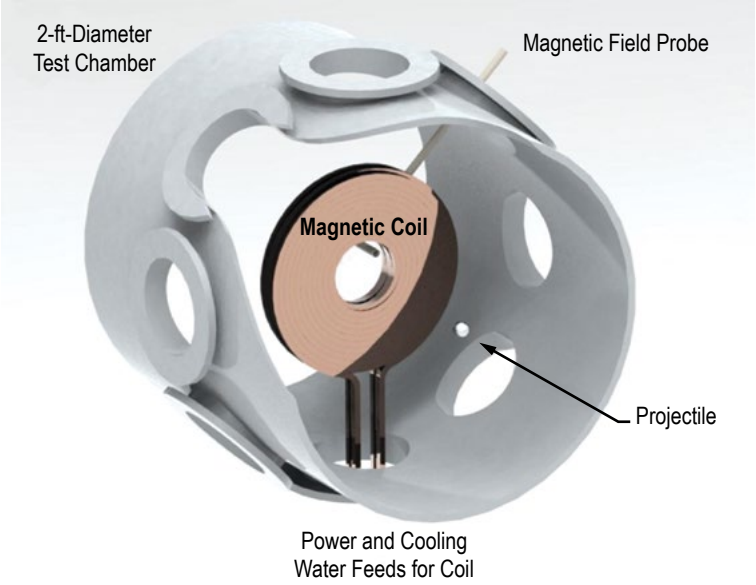

Figure 48. Magnetic flux and target compression test setup.

The ability to perform target compression tests with available ground facilities and equipment provides a relatively low-cost approach for proof-of-concept testing of the target field interaction, underpinning the proposed concept. Using an LGG to inject a high-speed target into a strong magnetic field produced by water-cooled coils can economically map multiple parametric conditions against which the numerical models can be validated, with the results extrapolated to more accurately model this promising in-space propulsion system. Although not as well developed, a simultaneous program to evaluate pulsed material ablation from a target surface could also be carried out with commercially available kilowatt-class lasers and available highly accurate impulse thrust

stands to evaluate the momentum imparted to a known target mass as a function of laser intensity and ablative material. The combination of ablative acceleration experiments and target compression experiments, performed in available facilities with available or commercial off-the-shelf-purchased equipment, would demonstrate the initial feasibility of the concept. As the terrestrial fusion community continues the development of MIF targets and the compression conditions required for gainful energy production, their results can be readily incorporated into the proposed system to refine target designs, magnetic field strengths and geometries, and acceleration requirements for a realistic, fusion-based propulsion system.

9. CONCLUDING REMARKS

Human exploration of the solar system beyond our immediate neighborhood requires significantly faster transit times than offered by current or near-term, in-space propulsion systems. Crewed missions to Mars, Saturn, or other deep space destinations must balance the benefits of exploration against concerns for crew health and survivability. At present, there are no implementable countermeasures against the high-energy radiation associated with solar flares and cosmic radiation, or the deleterious effects of long-duration weightlessness on the human body. Reducing astronaut trip times will help mitigate these survivability issues, while simultaneously reducing crew logistics mass and overall mission cost. Deep space robotic missions such as the notional Thousand Astronomical Unit mission will also benefit from more rapid trip times by delivering instruments and providing data within the career lifetimes of the scientists at home.

This Phase I project has evaluated the dynamics associated with a novel magnetized target fusion system proposed for rapid solar system exploration. Replacing the standard θ-pinch geometry of a static target within a rapidly rising axial magnetic field to generate radial compressive forces, the concept under investigation injects a target at high axial velocity into a static axial magnetic field, creating similar radial compression forces in a geometry more suitable for in-space propulsion. During the Phase I effort, a semi-analytic model was developed to simulate the key physics of target injection, radial liner compression, and conditions for gainful fusion energy release. A number of simulations were performed to define optimum target and field conditions, which were used to inform mission analysis and vehicle design studies. Concurrently, substantial progress was made in the development of a significantly more accurate 3D physics-based simulation, which will be used to further refine the target and field conditions required for sensible fusion gain. Preliminary results of the advanced simulation have demonstrated that liner currents are indeed induced due to rapid target injection into a strong magnetic field, underpinning the fundamental physics of the concept. Using the results of the analytic model, mission analysis has been performed for both Mars and Saturn missions, showing significantly reduced trip times for crewed missions and the capability for substantial cargo delivery supporting sustained exploration. Preliminary vehicle designs have been developed based on estimated parameters for the proposed system, forming a baseline against which more detailed designs will be developed as the modeling results are further refined.

The rapid human exploration of destinations within our solar system requires significantly more energetic propulsion systems than current chemical engines or nuclear thermal propulsion can provide. The pulsed fusion propulsion system described in this Phase I TP may offer a practical, viable method to achieve the accelerations required for fast interplanetary transits. If successful, the concept will enable a new class of crewed exploration missions less constrained by the frailties of the human physique, opening the solar system to our ever-expanding need for human exploration.

APPENDIX A—ANALYTIC MODEL BLOCK DIAGRAM

Shown is the block diagram of the semi-analytic model used in the Phase I activity. The equations corresponding to the major blocks are discussed in detail in section 3.

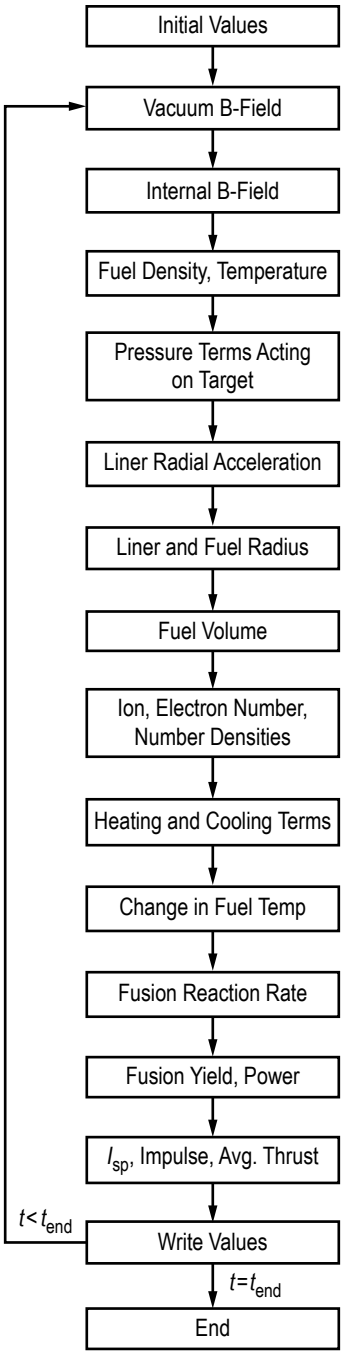

APPENDIX B—ANALYTIC MODEL DATA VALUES

Assumptions: All energy gain and loss terms included
Initial fuel temp before preheat: 1-eV
Inner coil radius: 2.5-cm
Total run time: 100 microseconds

Change Density		Density (kg/m^3)	Isp (s)	Ibit (N-s)	Yield (J)	P_preheat (W)	Preheat time (s)	P_accel (W)	Gain
Density	*change*	0.01	6.19E+03	5.21E+02	1.58E+07	2.10E+08	3.01E-05	1.25E+04	3.62E+01
Injection VZ0	10-km/s	0.02	9.49E+03	8.00E+02	4.25E+07	4.20E+08	2.95E-05	1.25E+04	9.59E+01
R_liner	1-cm	0.03	1.19E+04	1.00E+03	7.03E+07	6.30E+08	2.92E-05	1.25E+04	1.56E+02
Aspect Ratio	6	0.04	1.39E+04	1.17E+03	9.80E+07	8.41E+08	2.92E-05	1.25E+04	2.15E+02
Liner material	Be	0.05	1.56E+04	1.31E+03	1.25E+08	1.05E+09	2.93E-05	1.25E+04	2.71E+02
Initial fuel temp	1-eV	0.06	1.70E+04	1.44E+03	1.52E+08	1.26E+09	2.95E-05	1.25E+04	3.24E+02
Fuel preheat	500-eV	0.07	1.80E+04	1.51E+03	1.70E+08	1.47E+09	2.97E-05	1.25E+04	3.57E+02
BZ_max	30-T	0.075	1.89E+03	1.59E+02	4.54E+05	1.58E+09	2.97E-05	1.25E+04	9.50E-01
BZ_int	1-T	0.08	1.63E+03	1.37E+02	2.24E+05	1.68E+09	2.98E-05	1.25E+04	4.66E-01
Grad BZ	100-T/m	0.10	1.27E+03	1.07E+02	4.04E+04	2.10E+09	3.02E-05	3.03E-05	8.17E-02
Final Vz (m/s)	9.90E+03								

Change VZ0		VBZ0 (km/s)	Isp (s)	Ibit (N-s)	Yield (J)	P_preheat (W)	Preheat time (s)	P_accel (W)	Gain
Density	0.07-kg/m^3	2.00	1.97E+02	1.66E+01	7.21E-01	2.86E+08	1.00E-04	5.02E+02	1.17E-05
Injection VZ0	*change*	5.00	5.91E+02	4.98E+01	4.98E+03	7.27E+08	6.13E-05	3.14E+03	3.27E-02
R_liner	1-cm	8.00	1.34E+03	1.13E+02	1.67E+05	1.17E+09	3.49E-05	8.03E+03	5.21E-01
Aspect Ratio	6	8.50	1.53E+03	1.29E+02	2.65E+05	1.25E+09	3.34E-05	9.07E+03	7.45E-01
Liner material	Be	9.00	1.77E+03	1.49E+02	4.35E+05	1.32E+09	3.21E-05	1.02E+04	1.11E+00
Initial fuel temp	1-eV	9.50	2.14E+03	1.81E+02	8.25E+05	1.40E+09	3.08E-05	1.13E+04	1.91E+00
Fuel preheat	500-eV	9.75	2.54E+03	2.14E+02	1.43E+06	1.43E+09	3.02E-05	1.19E+04	3.15E+00
BZ_max	30-T	10.00	1.80E+04	1.51E+03	1.70E+08	1.47E+09	2.97E-05	1.25E+04	3.57E+02
BZ_int	1-T	12.50	1.89E+04	1.59E+03	1.83E+08	1.84E+09	2.42E-05	1.96E+04	2.56E+02
Grad BZ	100-T/m	15.00	1.93E+04	1.63E+03	1.87E+08	2.22E+09	2.01E-05	2.82E+04	1.85E+02
		17.50	1.97E+04	1.66E+03	1.90E+08	2.59E+09	1.72E-05	3.84E+04	1.39E+02
		20.00	2.01E+04	1.69E+03	1.92E+08	2.96E+09	1.50E-05	5.02E+04	1.09E+02

Change Radius		R_liner (cm)	Isp (s)	Ibit (N-s)	Yield (J)	P_preheat (W)	Preheat time (s)	P_accel (W)	Gain
Density	0.07-kg/m^3	0.75	1.25E+03	5.91E+01	1.84E+04	8.29E+08	2.89E-05	7.06E+03	6.90E-02
Injection VZ0	10-km/s	1.00	1.80E+04	1.51E+03	1.70E+08	1.47E+09	2.97E-05	1.25E+04	3.57E+02
R_liner	*change*	1.25	1.81E+04	2.39E+03	2.71E+08	2.30E+09	2.97E-05	1.96E+04	3.65E+02
Aspect Ratio	6	1.50	1.81E+04	3.44E+03	3.89E+08	3.31E+09	2.94E-05	2.82E+04	3.64E+02
Liner material	Be	2.00	1.77E+04	6.15E+03	6.79E+08	5.81E+09	2.84E-05	5.02E+04	3.49E+02
Initial fuel temp	1-eV								
Fuel preheat	500-eV								
BZ_max	30-T								
BZ_int	1-T								
Grad BZ	100-T/m								
Final Vz (m/s)	9.90E+03								

Change Max Preheat Temp		Tpre_fuel (eV)	Isp (s)	Ibit (N-s)	Yield (J)	P_preheat (W)	Preheat time (s)	P_accel (W)	Gain
Density	0.07-kg/m^3	50	1.01E+03	8.51E+01	6.69E-12	1.05E+08	3.03E-05	1.25E+04	1.54E-17
Injection VZ0	10-km/s	100	1.01E+03	8.55E+01	9.33E+00	2.10E+08	2.81E-05	1.25E+04	2.14E-05
R_liner	1.0-cm	200	1.26E+03	1.06E+02	3.70E+04	4.20E+08	2.73E-05	1.25E+04	8.35E-02
Aspect Ratio	6	300	2.54E+03	2.14E+02	1.39E+06	6.30E+08	2.77E-05	1.25E+04	3.09E+00
Liner material	Be	400	1.55E+04	1.30E+03	1.23E+08	8.41E+08	2.85E-05	1.25E+04	2.71E+02
Initial fuel temp	1-eV	500	1.56E+04	1.31E+03	1.25E+08	1.05E+09	2.93E-05	1.25E+04	2.71E+02
Fuel preheat	*change*	750	1.57E+04	1.32E+03	1.27E+08	1.58E+09	3.03E-05	1.25E+04	2.66E+02
BZ_max	30-T								
BZ_int	1-T								
Grad BZ	100-T/m								
Final Vz (m/s)	9.90E+03								

Change BZ_max		BZ_max (T)	Isp (s)	Ibit (N-s)	Yield (J)	P_preheat (W)	Preheat time (s)	P_accel (W)	Gain
Density	0.07-kg/m^3	5.0	1.02E+03	8.60E+01	3.62E-02	8.92E+09	5.00E-06	1.25E+04	7.63E-08
Injection VZ0	10-km/s	10.0	1.02E+03	8.60E+01	3.26E-02	4.46E+09	1.00E-05	1.25E+04	6.87E-08
R_liner	1.0-cm	20.0	1.08E+03	9.07E+01	2.10E+03	2.22E+09	2.01E-05	1.25E+04	4.43E-03
Aspect Ratio	6	25.0	1.29E+03	1.09E+02	4.59E+04	1.77E+09	2.52E-05	1.25E+04	9.67E-02
Liner material	Be	27.5	1.59E+03	1.34E+02	1.97E+05	1.61E+09	2.77E-05	1.25E+04	4.16E-01
Initial fuel temp	1-eV	29.0	2.06E+03	1.74E+02	6.49E+05	1.52E+09	2.93E-05	1.25E+04	1.37E+00
Fuel preheat	500-eV	30.0	1.80E+04	1.51E+03	1.70E+08	1.47E+09	2.97E-05	1.25E+04	3.57E+02
BZ_max	*change*	40.0	1.86E+04	1.57E+03	1.83E+08	1.10E+09	3.24E-05	1.25E+04	3.85E+02
BZ_int	1-T	50.0	1.84E+04	1.55E+03	1.80E+08	8.74E+08	3.40E-05	1.25E+04	3.78E+02
Grad BZ	100-T/m								
Final Vz (m/s)	9.90E+03								

Change BZ_int		BZ_int (T)	Isp (s)	Ibit (N-s)	Yield (J)	P_preheat (W)	Preheat time (s)	P_accel (W)	Gain
Density	0.07-kg/m^3	1.0	1.80E+04	1.51E+03	1.70E+08	1.47E+09	2.97E-05	1.25E+04	3.57E+02
Injection VZ0	10-km/s	2.0	1.77E+04	1.49E+03	1.64E+08	1.47E+09	2.68E-05	1.25E+04	3.45E+02
R_liner	1.0-cm	2.5	1.64E+04	1.38E+03	1.40E+08	1.47E+09	2.62E-05	1.25E+04	2.95E+02
Aspect Ratio	6	3.0	2.01E+03	1.70E+02	5.95E+05	1.47E+09	2.57E-05	1.25E+04	1.25E+00
Liner material	Be	5.0	1.26E+03	1.06E+02	3.72E+04	1.47E+09	2.44E-05	1.25E+04	7.85E-02
Initial fuel temp	1-eV								
Fuel preheat	500-eV								
BZ_max	30-T								
BZ_int	*change*								
Grad BZ	100-T/m								
Final Vz (m/s)	9.90E+03								

Change Grad Bz	(BZ_max=30-T)	Grad BZ (T/m)	Isp (s)	Ibit (N-s)	Yield (J)	P_preheat (W)	Preheat time (s)	P_accel (W)	Gain
Density	0.07-kg/m^3	50	1.10E+03	9.29E+01	5.04E+03	7.35E+08	6.07E-05	1.25E+04	1.06E-02
Injection VZ0	10-km/s	75	1.43E+03	1.21E+02	1.05E+05	1.10E+09	3.65E-05	1.25E+04	2.21E-01
R_liner	1.0-cm	90	1.87E+03	1.57E+02	4.35E+05	1.32E+09	3.21E-05	1.25E+04	9.17E-01
Aspect Ratio	6	100	1.80E+04	1.51E+03	1.70E+08	1.47E+09	2.97E-05	1.25E+04	3.57E+02
Liner material	Be	125	1.86E+04	1.57E+03	1.83E+08	1.84E+09	2.42E-05	1.25E+04	3.86E+02
Initial fuel temp	1-eV	150	1.88E+04	1.59E+03	1.87E+08	2.21E+09	2.02E-05	1.25E+04	3.95E+02
Fuel preheat	500-eV	200	1.90E+04	1.60E+03	1.92E+08	2.95E+09	1.51E-05	1.25E+04	4.04E+02
BZ_max	30-T								
BZ_int	1-T								
Grad BZ	*change*								
Final Vz (m/s)	9.90E+03								

Change Liner Material		Liner Material	Isp (s)	Ibit (N-s)	Yield (J)	P_preheat (W)	Preheat time (s)	P_accel (W)	Gain
Density	0.07-kg/m^3	AL	1.27E+03	1.56E+02	5.79E+04	1.48E+09	3.02E-05	3.76E+04	8.66E-02
Injection VZ0	10-km/s	Be	1.80E+04	1.51E+03	1.70E+08	1.47E+09	2.97E-05	1.25E+04	3.57E+02
R_liner	1.0-cm	Li	3.49E+04	8.45E+02	1.95E+08	1.46E+09	2.29E-05	9.66E+03	1.16E+03
Aspect Ratio	6								
Liner material	*change*								
Initial fuel temp	1-eV								
Fuel preheat	500-eV								
BZ_max	30-T								
BZ_int	1-T								
Grad BZ	*change*								
Final Vz (m/s)	9.90E+03								

REFERENCES

1. Murray, K.A.: "The Gevaltig: An Inertial Fusion Powered Manned Spacecraft Design for Outer Solar System Missions," NASA-CR-185163, NASA Lewis Research Center, Cleveland, OH, October 1989.

2. Orth, C.D.: "VISTA—A Vehicle for Interplanetary Space Transport Application Powered by Inertial Confinement Fusion," Final Systems Report, UCRL-TR-110500, Lawrence Livermore National Laboratory, Livermore, CA, May 16, 2003.

3. Bond, A.; and Martin, A.R.: "Project Daedalus," *Journal of the British Interplanetary Society* (*Supplement*)," Vol. 31, pp. 55–57, 1978.

4. Project Icarus, Starship Congress 2017 Program, http://icarusinterstellar.org/, July 31, 2017.

5. Williams, C.H.; Dudzinski, L.A.; Borowski, S.K.;, and Juhasz, A.J.: "Realizing "2001: A Space Odyssey": Piloted Spherical Torus Nuclear Fusion Propulsion," NASA/TM—2005–213559, NASA Glenn Research Center, Cleveland, OH, 52 pp., March 2005.

6. Slough, J.A.: "Propagating Magnetic Wave Plasma Accelerator (PMWAC) for Deep Space Exploration," Phase I Final Report, NASA Institute for Advanced Concepts, 1999.

7. Slough, J.; Pancotti, A.; Kirtley, D.; et al.: "Nuclear Propulsion through Direct Conversion of Fusion Energy: The Fusion Driven Rocket," NASA Innovative and Advanced Concepts, Phase I Final Report, NASA, Washington, DC, <https://ntrs.nasa.gov/search.jsp?R=20160010608 2018-05-14T16:36:59+00:00Z>, 32 pp., September 30, 2012.

8. Adams, R.B.; Cassibry, J.; Bradley, D.E.; et al.: "Pulsed Fission-Fusion (PuFF) – Phase I Report," NASA Innovative and Advanced Concepts, Final Report, 52 pp., 2013.

9. Gibbs, W.W.: "The Fusion Underground," *Scientific American*, Vol. 315, pp. 38–45, doi:10.1038/scientificamerican1116-38, November 2016.

10. Waldrop, M.M.: "Plasma Physics: The Fusion Upstarts," *Nature*, Vol. 511, Issue 7510, pp. 398–400, July 24, 2014.

11. Slutz, S.A.; Stygar, W.A.; Comez, M.R.; et al.: "Scaling Magnetized Liner Inertial Fusion on Z and Future Pulsed-Power Accelerators," *Physics of Plasmas*, Vol. 23, Issue 2, Article No. 022702, https://doi.org/10.1063/1.4941100, February 2016.

12. National Research Council, Committee on the Prospects for Inertial Confinement Fusion Energy, "An Assessment of the Prospects for Inertial Fusion Energy," National Academies Press, 237 pp., 2013.

13. Liberman, M.A.; De Groot, J.S.; Toor, A.; and Spielman, R.B.: *Physics of High-Density Z-Pinch Plasmas*, Springer, 276 pp., 1999.

14. Sefkow, A.B.; Slutz, S.A.; Koning, J.M.; et al.: "Design of magnetized liner inertial fusion experiments using the Z facility," *Physics of Plasmas*, Vol. 21, 072711, https://doi.org/10.1063/1.4890298, 2014.

15. Miyamoto, K.: *Plasma Physics for Nuclear Fusion*, MIT Press, Cambridge, MA, 1987.

16. Cassibry, J.; Cortez, R.; Stanic, M; et al., "Case and Development Path for Fusion Propulsion," *J. Spacecraft and Rockets*, Vol. 52, Issue 2, pp. 595–612, https://doi.org/10.2514/1.A32782, March–April 2015.

17. Wurden, G.A.; Hsu, S.C.; Intrator, T.P.; et al., "Magneto-Inertial Fusion," *J. Fusion Energy*, Vol. 35, Issue 1, pp. 69–77, 2016.

18. Gomez, M.R.; Slutz, S.A.; Sefkow, A.B.; et al. (and refs. therein), "Experimental Demonstration of Fusion-Relevant Conditions in Magnetized Liner Inertial Fusion," *Phys. Rev. Lett.*, Vol. 113, Issue 15, pp. 155003-1–15503-4, October 16, 2014.

19. Awe, T.J.; et al.: "Experimental Demonstration of the Stabilizing Effect of Dielectric Coatings on Magnetically Accelerated Imploding Metallic Liners," *Phys. Rev. Lett.*, Vol. 116, Issue 6, p. 065001, February 2016.

20. Basko, M.M.; Kempb, A.J.; and Meyer-ter-Vehn, J.: "Ignition conditions for magnetized target fusion in cylindrical geometry," *Nuclear Fusion*, Vol. 40, Issue 1, pp. 59–63, 2000.

21. Freeland, R.M.: "Project Icarus: Fission-Fusion Hybrid Fuel for Interstellar Propulsion," J. British Interplanetary Society, Vol. 66, pp. 290–296, 2013.

22. Kirtley, D.; Slough, J.; Schonig, J.; and Ketsdever, A.: "Pulsed Inductive Macron Propulsion," Joint Army-Navy-NASA-Air Force (JANNAF) Space Propulsion Systems Conference, Colorado Springs, CO, May 3–7, 2010.

23. Esmond, M.J.: Mostaghim, S.S.; Gebhart, T.E.; and Winfrey, A.L.: "Investigation of Electrothermal Plasma Pellet Launcher Optimization for Fusion Fueling," 2014 IEEE 41st International Conference on Plasma Sciences (ICOPS)/2014 IEEE International Conference on High-Power Particle Beams (BEAMS), DOI: 10.1109/PLASMA.2014.7012717, May 25–29, 2014.

24. Felber, F.S.: "Model of Ablative Acceleration at Moderate Laser Intensities," *Phys. Fluids*, Vol. 23, Issue 7, pp. 1380–1382, July 1980.

25. Jarboe, T.R.: "Confinement and Acceleration of Pellet Material by One-Sided Laser Irradiation," *Phys. Fluids B*, Vol. 5, Issue 4, pp. 1332–1335, April 1993.

26. Jarboe, T.R.; Kunkel, W.B.; and Lietzke, A.F.: "Study of Plasma Density Distribution Produced by Irradiating a 50-μ Deuterium Pellet on One Side With a Ruby Laser," *Phys. Fluids*, Vol. 19, Issue 10, pp. 1501–1506, October 1976.

27. National High Magnetic Field Laboratory, <futurism.com/superconducting-magnet-smashes-world-record/> The world-record holding superconducting magnet has a cold bore size of 3.4- cm, weighs approximately 2.3 tons, and has an axial magnetic field strength of 32 T, accessed March 10, 2018.

28. Cassibry, J.T.; and Wu, S.T.: "Sub-Alfvenic Inlet Boundary Conditions for Axisymmetric MHD Nozzles," 37th AIAA Plasmadynamics and Lasers Conference, San Francisco, CA, https://doi.org/10.2514/6.2006-3561, 2006.

29. Williams, C.H.: "Application of Recommended Design Practices for Conceptual Nuclear Fusion Space Propulsion Systems," AIAA Paper 2004-3534, 10th Joint Propulsion Conference and Exhibit, Fort Lauderdale, FL, July 11–14, 2004.

30. McBride, R.D.; and Slutz, S.A.: "A Semi-Analytic Model of Magnetized Liner Inertial Fusion," Phys. Plasmas, Vol. 22, p. 052708, https://doi.org/10.1063/1.4918953, 2015.

31. Slutz, S.A.; Hermann, M.C.; Vesey, R.A.; et al.: "Pulsed Power-Driven Cylindrical Liner Implosions of Laser Preheated Fuel Magentized with an Axial Field," *Phys. Plasmas*, Vol. 17, p. 056303, https://doi.org/10.1063/1.3333505, 2010.

32. Monaghan, J.J.: "Smoothed Particle Hydrodynamics," *Rep. Prog. Phys*., Vol. 68, Number 8, p. 57, July 5, 2005.

33. Huba, J.D.: "NRL: Plasma Formulary," Naval Research Laboratory, Washington, DC, NRL/PU/6790-04-477, 72 pp., December 2004.

34. Fowler, C.M.; and Altgilbers, L.L.: "Magnetic Flux Compression Generators: a Tutorial and Survey," *Electromagnetic Phenomena*, Vol. 3, No. 3(11), pp. 305–357, 2003.

35. Zola, C.L.: "A Method of Approximating Propellant Requirements of Low-Thrust Trajectories," NASA TN D-3400, NASA Lewis Research Center, Cleveland, OH, 54 pp., April 1966.

36. Gilland, J.H.: "Mission and System Optimization of Nuclear Electric Propulsion Vehicles for Lunar and Mars Missions," NASA Contractor Report 189058, NASA Lewis Research Center, Cleveland, OH, 16 pp., December 1991.

37. Adams, R.B.; Cassibry, J.T.; and Schillo, K.: "Developing the Pulsed Fission-Fusion (PuFF) Engine," 50th AIAA/ASME/SAE/ASEE Joint Propulsion Conference, AIAA Propulsion and Energy Forum, AIAA 2014-3520, Cleveland, OH, July 28–30, 2014.

38. Jackman, A.: Space Launch System, A New Capability for Space Exploration, https://sites.nationalacademies.org/cs/groups/ssbsite/documents/webpage/ssb_171779.pdf, March 29, 2016.

39. Adams, R.B.; Alexander, R.A.; Chapman, J.M.; et al.: "Conceptual Design of In-Space Vehicles for Human Exploration of the Outer Planets," NASA/TP—2004–213089, NASA Marshall Space Flight Center, Huntsville, AL, 141 pp., 2004.

40. Miernik, J.; Statham, G.; Fabisinski, L.; et al.: "Z-Pinch Fusion-based Nuclear Propulsion," *Acta Astronautica*, Vol. 82, Issue 2, pp. 173–182, February 2013.

REPORT DOCUMENTATION PAGE

Form Approved
OMB No. 0704-0188

1. REPORT DATE *(DD-MM-YYYY)*	2. REPORT TYPE	3. DATES COVERED *(From - To)*
01–09–2018	Technical Publication	May 2017–February 2018

4. TITLE AND SUBTITLE

Gradient Field Imploding Liner Fusion Propulsion System
NASA Innovative Advanced Concepts Phase I Final Report

5a. CONTRACT NUMBER

5b. GRANT NUMBER

5c. PROGRAM ELEMENT NUMBER

6. AUTHOR(S)

M.R. Lapointe, R.B. Adams, J. Cassibry,*
M. Zweiner,* and J.H. Gilland**

5d. PROJECT NUMBER

5e. TASK NUMBER

5f. WORK UNIT NUMBER

7. PERFORMING ORGANIZATION NAME(S) AND ADDRESS(ES)

George C. Marshall Space Flight Center
Huntsville, AL 35812

8. PERFORMING ORGANIZATION REPORT NUMBER

M–1471

9. SPONSORING/MONITORING AGENCY NAME(S) AND ADDRESS(ES)

National Aeronautics and Space Administration
Washington, DC 20546–0001

10. SPONSORING/MONITOR'S ACRONYM(S)

NASA

11. SPONSORING/MONITORING REPORT NUMBER

NASA/TP—2018–219996

12. DISTRIBUTION/AVAILABILITY STATEMENT

Unclassified-Unlimited
Subject Category 99
Availability: NASA STI Information Desk (757–864–9658)

13. SUPPLEMENTARY NOTES

Prepared by the Exploration Systems and Systems Development Division, Science and Technology Office Directorate
*The University of Alabama—Huntsville, Huntsville, AL **Ohio Aerospace Institute, Cleveland, OH

14. ABSTRACT

The advancement of human deep space exploration requires the continued development of energetic in-space propulsion systems, advancing from current chemical engines to nuclear thermal rockets to future high energy concepts such as nuclear fusion. This Technical Publication (TP) presents the initial results of a NASA Innovative Advanced Concepts Phase I study funded to investigate the feasibility of a new pulsed fusion propulsion concept based on the rapid implosion of a fuel target injected at high velocity into a strong stationary magnetic field. The proposed concept takes advantage of the significant advances in terrestrial magneto-inertial fusion designs while attempting to mitigate the most common engineering impediments to in-space propulsion applications. A semi-analytic numerical model developed to optimize fusion target energy release and engine performance is described, along with initial steps toward a 3D smooth particle hydrodynamic code to more accurately model the target implosion physics. A preliminary vehicle design concept is presented, and representative trajectory analyses for rapid Mars and Saturn missions are provided. This TP concludes with an overview of proposed next steps for theoretical and experimental validation of the concept.

15. SUBJECT TERMS

spacecraft, propulsion, power

16. SECURITY CLASSIFICATION OF:			17. LIMITATION OF ABSTRACT	18. NUMBER OF PAGES	19a. NAME OF RESPONSIBLE PERSON
a. REPORT	b. ABSTRACT	c. THIS PAGE			STI Help Desk at email: help@sti.nasa.gov
U	U	U	UU	102	19b. TELEPHONE NUMBER *(Include area code)* STI Help Desk at: 757–864–9658

National Aeronautics and
Space Administration
IS02
George C. Marshall Space Flight Center
Huntsville, Alabama 35812